The Astrophysical Journal, 821:116 (29pp), 2016 April 20 doi:10.3847/0004-637X/821/2/116

CLASH: JOINT ANALYSIS OF STRONG-LENSING, WEAK-LENSING SHEAR, AND MAGNIFICATION DATA FOR 20 GALAXY CLUSTERS*

Keiichi Umetsu[1], Adi Zitrin[2,10], Daniel Gruen[3,4,5,6,11], Julian Merten[7], Megan Donahue[8], and Marc Postman[9]
[1] Institute of Astronomy and Astrophysics, Academia Sinica, P. O. Box 23-141, Taipei 10617, Taiwan; keiichi@asiaa.sinica.edu.tw
[2] Cahill Center for Astronomy and Astrophysics, California Institute of Technology, MS 249-17, Pasadena, CA 91125, USA
[3] Universitäts-Sternwarte, München, Scheinerstrasse 1, D-81679 München, Germany
[4] Max-Planck-Institut für extraterrestrische Physik, Giessenbachstrasse 1, D-85748, Garching, Germany
[5] SLAC National Accelerator Laboratory, Menlo Park, CA 94025, USA
[6] Kavli Institute for Particle Astrophysics and Cosmology, Stanford University, Palo Alto, CA 94305, USA
[7] Department of Physics, University of Oxford, Keble Road, Oxford OX1 3RH, UK
[8] Department of Physics and Astronomy, Michigan State University, East Lansing, MI 48824, USA
[9] Space Telescope Science Institute, 3700 San Martin Drive, Baltimore, MD 21208, USA
Received 2015 July 19; accepted 2016 March 2; published 2016 April 20

ABSTRACT

We present a comprehensive analysis of strong-lensing, weak-lensing shear and magnification data for a sample of 16 X-ray-regular and 4 high-magnification galaxy clusters at $0.19 \lesssim z \lesssim 0.69$ selected from Cluster Lensing And Supernova survey with Hubble (CLASH). Our analysis combines constraints from 16-band *Hubble Space Telescope* observations and wide-field multi-color imaging taken primarily with Suprime-Cam on the Subaru Telescope, spanning a wide range of cluster radii (10″–16′). We reconstruct surface mass density profiles of individual clusters from a joint analysis of the full lensing constraints, and determine masses and concentrations for all of the clusters. We find the internal consistency of the ensemble mass calibration to be $\leqslant 5\% \pm 6\%$ in the one-halo regime (200–2000 kpc h^{-1}) compared to the CLASH weak-lensing-only measurements of Umetsu et al. For the X-ray-selected subsample of 16 clusters, we examine the concentration–mass (c–M) relation and its intrinsic scatter using a Bayesian regression approach. Our model yields a mean concentration of $c|_{z=0.34} = 3.95 \pm 0.35$ at $M_{200c} \simeq 14 \times 10^{14}\, M_\odot$ and an intrinsic scatter of $\sigma(\ln c_{200c}) = 0.13 \pm 0.06$, which is in excellent agreement with Λ cold dark matter predictions when the CLASH selection function based on X-ray morphological regularity and the projection effects are taken into account. We also derive an ensemble-averaged surface mass density profile for the X-ray-selected subsample by stacking their individual profiles. The stacked lensing signal is detected at 33σ significance over the entire radial range $\leqslant 4000$ kpc h^{-1}, accounting for the effects of intrinsic profile variations and uncorrelated large-scale structure along the line of sight. The stacked mass profile is well described by a family of density profiles predicted for cuspy dark-matter-dominated halos in gravitational equilibrium, namely, the Navarro–Frenk–White (NFW), Einasto, and DARKexp models, whereas the single power-law, cored isothermal and Burkert density profiles are disfavored by the data. We show that cuspy halo models that include the large-scale two-halo term provide improved agreement with the data. For the NFW halo model, we measure a mean concentration of $c_{200c} = 3.79^{+0.30}_{-0.28}$ at $M_{200c} = 14.1^{+1.0}_{-1.0} \times 10^{14}\, M_\odot$, demonstrating consistency between the complementary analysis methods.

Key words: cosmology: observations – dark matter – galaxies: clusters: general – gravitational lensing: strong – gravitational lensing: weak

1. INTRODUCTION

Clusters of galaxies represent the largest and rarest class of self-gravitating systems formed in the universe. In the context of hierarchical models of structure formation, the evolution of the cluster abundance with cosmic time is a sensitive probe of the amplitude and growth rate of the primordial fluctuation spectrum because cluster-sized systems populate the exponential tail of the cosmic mass function of dark-matter (DM, hereafter) halos (Haiman et al. 2001). Therefore, large cluster samples with well-defined selection functions can, in principle, provide an independent test of any viable cosmological model, including the current concordance Λ cold dark matter (ΛCDM) model defined in the framework of general relativity, complementing cosmic microwave background (CMB) anisotropy, large-scale galaxy clustering, supernova, CMB lensing, and cosmic shear experiments. Currently, cluster samples are often defined by optical, X-ray, or Sunyaev–Zel'dovich effect (SZE) observables (e.g., Vikhlinin et al. 2009; Planck Collaboration et al. 2014), so that the masses are indirectly inferred from scaling relations. In the last few years, a systematic effort has been conducted to enable a self-consistent calibration of mass–observable relations using robust cluster lensing measurements (Ford et al. 2014; Gruen et al. 2014; Umetsu et al. 2014; von der Linden et al. 2014b; Hoekstra et al. 2015; Jimeno et al. 2015; Melchior et al. 2015; Merten et al. 2015) and well-defined selection functions (Benitez et al. 2014; Miyazaki et al. 2015).

Considerable progress has been made in understanding the formation and evolution of DM halos in an expanding universe, governed by nonlinear gravitational growth of cosmic density perturbations. N-body simulations of collisionless CDM established a nearly self-similar form for the spherically averaged density profile $\rho_h(r)$ of DM halos (Navarro et al. 1997, hereafter Navarro–Frenk–White, NFW) over a wide range of halo masses and radii, with some intrinsic variance associated with the mass accretion histories of

* Based in part on data collected at the Subaru Telescope, which is operated by the National Astronomical Society of Japan.
[10] Hubble Fellow.
[11] Einstein Fellow.

individual halos (Jing & Suto 2000; Tasitsiomi et al. 2004; Graham et al. 2006; Navarro et al. 2010; Ludlow et al. 2013; Adhikari et al. 2014; Diemer & Kravtsov 2014). The degree of mass concentration, $c_{200c} = r_{200c}/r_{-2}$,[12] is predicted to correlate with halo mass because the scale radius r_{-2} stays approximately constant when the halo leaves the fast accretion regime, whereas r_{200c} does still grow, thus increasing concentration. Cluster-sized halos are thus predicted to be less concentrated than less massive halos and to have typical concentrations of $c_{200c} = 3$–4 (Bhattacharya et al. 2013; Dutton & Macciò 2014; Meneghetti et al. 2014).

Galaxy clusters act as powerful gravitational lenses (e.g., Kneib & Natarajan 2011), offering a direct probe for testing these well defined predictions of DM halo structure. The critical advantage of cluster gravitational lensing is its ability to map the mass distribution of individual systems independent of assumptions about their physical and dynamical state. Clusters produce a variety of detectable lensing effects, including deflection, shearing, and magnifying of the images of background sources (Bartelmann & Schneider 2001). In the weak regime where the lensing signal is approximately linearly related to the potential, lensing can be used to probe the mass distribution of clusters in a model-independent manner (e.g., Kaiser & Squires 1993; Fahlman et al. 1994; Kaiser 1995; Umetsu et al. 1999; Clowe et al. 2000). In the strong regime, several sets of multiple images with known redshifts allow us to tightly constrain the central mass distribution (e.g., Zitrin et al. 2012b; Jauzac et al. 2014). For a massive cluster, the two complementary regimes contribute similar logarithmic radial coverage (Umetsu et al. 2011b, see their Figure 6). Hence, combining strong and weak lensing can significantly improve constraints on the cluster mass distribution for full radial coverage (Bradač et al. 2006; Limousin et al. 2007; Merten et al. 2009; Diego et al. 2015).

The Cluster Lensing And Supernova survey with Hubble (CLASH, Postman et al. 2012)[13] is a 524-orbit Multi-Cycle Treasury program that has been designed to probe the mass distribution of 25 galaxy clusters using their gravitational lensing properties, providing a sizable sample of mass calibrators for accurate cluster cosmology. All CLASH clusters were observed in 16 filters with the *Hubble Space Telescope* (*HST*). This 16-band *HST* photometry has enabled us to uncover many sets of multiple images (Zitrin et al. 2012b, 2015), whose spectroscopic redshifts have been determined from a dedicated spectroscopic survey conducted with the VIMOS spectrograph on the Very Large Telescope (VLT; Balestra et al. 2013; Biviano et al. 2013; Rosati et al. 2014; Girardi et al. 2015). CLASH has produced combined strong- and weak-lensing analyses of *HST* and Subaru Telescope observations, allowing for detailed mapping of the cluster mass distributions (Coe et al. 2012; Umetsu et al. 2012; Medezinski et al. 2013; Merten et al. 2015; Zitrin et al. 2015). Donahue et al. (2014) derived radial profiles of temperature, gas mass, and hydrostatic mass for the full CLASH sample using *XMM-Newton* and *Chandra* observations.

A major goal of the CLASH survey is to test models of structure formation by using the halo concentration–mass (c–M) relation determined from cluster gravitational lensing. For this aim, twenty CLASH clusters were selected to have X-ray temperatures greater than 5 keV and to show a smooth X-ray morphology, with no lensing information used a priori (Postman et al. 2012). A further sample of five clusters were selected by their high lens magnification properties to study magnified high-redshift galaxies behind the clusters (Zheng et al. 2012; Coe et al. 2013; Monna et al. 2014).

Recently, we have carried out a systematic study of the CLASH sample to obtain measurements of mass and concentration from cluster lensing (Meneghetti et al. 2014; Umetsu et al. 2014; Merten et al. 2015). Meneghetti et al. (2014) presented a detailed characterization of the CLASH X-ray-selected clusters with numerical simulations to make predictions about their intrinsic and observational properties. Umetsu et al. (2014) conducted a joint shear-and-magnification weak-lensing analysis of a subsample of the CLASH clusters, using wide-field multi-color imaging taken primarily with Subaru/Suprime-Cam. Merten et al. (2015) presented a two-dimensional strong- and weak-lensing (hereafter SaWLens) analysis of 19 CLASH X-ray-selected clusters, by combining strong and weak-shear lensing data from 16-band *HST* imaging with wide-field weak-shear data analyzed by Umetsu et al. (2014). In both analyses, we find excellent agreement between the data and ΛCDM predictions when the projection effects and the selection function based on X-ray morphology are taken into account. More recently, Xu et al. (2015) carried out an observational and theoretical study of the abundance of gravitationally lensed arcs in the CLASH survey, finding full agreement between the observations and simulations using an automated, objective arcfinding algorithm.

In this paper we present a comprehensive joint analysis of strong-lensing, weak-lensing shear and magnification data for a sample of 16 X-ray-regular and 4 high-magnification clusters selected from the CLASH survey. Our extended analysis combines the constraints from the CLASH Subaru and *HST* lensing data sets of Umetsu et al. (2014) and Zitrin et al. (2015). We aim to combine these complementary lensing constraints to construct individual cluster surface mass density profiles, from which we will determine the c–M relation. This improved mass-profile data set also allows us to obtain an ensemble calibration of cluster masses and to probe the ensemble-averaged cluster mass distribution.

The paper is organized as follows. In Section 2 we briefly describe the basic theory of cluster gravitational lensing. After summarizing the properties of the CLASH sample, we outline in Section 3 the formalism and procedure for constructing surface mass density profiles from a joint analysis of strong-lensing, weak-lensing shear and magnification constraints. In Section 4 we revisit the mass profile analysis of individual CLASH clusters by combining *HST* and ground-based lensing measurements. In Section 5, we conduct stacked lensing analysis of the X-ray-selected subsample to study their ensemble-averaged mass distribution. In Section 6 we examine the concentration–mass relation for the X-ray-selected subsample using Bayesian regression methods. Section 7 is devoted to the discussion of the results. Finally, a summary is given in Section 8.

Throughout this paper, we adopt a concordance ΛCDM cosmology with $\Omega_m = 0.27$, $\Omega_\Lambda = 0.73$, and $h = 0.7h_{70} = 0.7$ (Komatsu et al. 2011), where $H_0 = h \times 100\ \mathrm{km\,s^{-1}\,Mpc^{-1}} = h_{70} \times 70\ \mathrm{km\,s^{-1}\,Mpc^{-1}}$. We use the standard notation $M_{\Delta c}$ ($M_{\Delta m}$) to denote the mass enclosed within a sphere of radius $r_{\Delta c}$ ($r_{\Delta m}$), within which the mean overdensity is Δ_c (Δ_m) times the critical density $\rho_c(z)$ (mean background density $\overline{\rho}_m(z)$) at

[12] The quantity r_{200c} is defined as the radius within which the mean interior density is 200 times the critical density $\rho_c(z)$ of the universe at the cluster redshift z, and r_{-2} is a scale radius at which $d \ln \rho_h / d\ln r = -2$.

[13] http://www.stsci.edu/~postman/CLASH/

the cluster redshift z. All quoted errors are 68.3% (1σ) confidence limits (CL) unless otherwise stated.

2. CLUSTER LENSING BASICS

In the cluster lensing regime (Umetsu 2010), the convergence $\kappa = \Sigma/\Sigma_c$ is the projected surface mass density $\Sigma(\theta)$ in units of the critical surface mass density for lensing, $\Sigma_c = (c^2 D_s)/(4\pi G D_l D_{ls}) \equiv c^2/(4\pi G D_l \beta)$, where D_l, D_s, and D_{ls} are the lens, source, and lens-source proper angular diameter distances, respectively, and $\beta(z, z_l) = D_{ls}/D_s$ is the geometric lensing strength as a function of source redshift z and lens redshift z_l.

The gravitational shear γ can be directly observed from ellipticities of background galaxies in the regime where $\kappa \ll 1$. The tangential shear component γ_+ averaged around a circle of radius θ satisfies the following *identity* (Kaiser 1995):

$$\gamma_+(\theta) = \kappa(<\theta) - \kappa(\theta) \equiv \Delta\Sigma(\theta)/\Sigma_c, \quad (1)$$

with $\kappa(\theta) = \Sigma(\theta)/\Sigma_c$ the azimuthally averaged convergence at radius θ, $\kappa(<\theta) = \Sigma(<\theta)/\Sigma_c$ the average convergence interior to θ, and $\Delta\Sigma(\theta) = \Sigma(<\theta) - \Sigma(\theta)$ the differential surface mass density.

The observable quantity for quadrupole weak lensing in general is not the shear but the *reduced* gravitational shear,

$$g(\boldsymbol{\theta}) = \frac{\gamma(\boldsymbol{\theta})}{1 - \kappa(\boldsymbol{\theta})}, \quad (2)$$

which is invariant under $\kappa(\boldsymbol{\theta}) \to \lambda\kappa(\boldsymbol{\theta}) + 1 - \lambda$ and $\gamma(\boldsymbol{\theta}) \to \lambda\gamma(\boldsymbol{\theta})$ with an arbitrary constant $\lambda \neq 0$, known as the mass-sheet degeneracy (Falco et al. 1985; Gorenstein et al. 1988; Schneider & Seitz 1995).This degeneracy can be broken, for example,[14] by measuring the magnification factor,

$$\mu(\boldsymbol{\theta}) = \frac{1}{[1 - \kappa(\boldsymbol{\theta})]^2 - |\gamma(\boldsymbol{\theta})|^2}, \quad (3)$$

which transforms as $\mu(\boldsymbol{\theta}) \to \lambda^2\mu(\boldsymbol{\theta})$.

We consider a population of source galaxies described by their redshift distribution function, $\overline{N}(z)$, for statistical weak-lensing measurements. The mean lensing depth for a given population ($X = g, \mu$) is given by

$$\langle\beta\rangle_X = \left[\int_0^\infty dz\, \overline{N}_X(z)\beta(z)\right]\left[\int_0^\infty dz\, \overline{N}_X(z)\right]^{-1}. \quad (4)$$

In general, we apply different size, magnitude, and color cuts in source selection for measuring the shear and magnification effects, leading to different $\overline{N}_X(z)$. In contrast to the former effect, the latter does not require source galaxies to be spatially resolved, but it does require a stringent flux limit against incompleteness effects.

We introduce the relative lensing depth of a source population with respect to a fiducial source in the far background as $\langle W\rangle_X = \langle\beta\rangle_X/\beta_\infty$ with $\beta_\infty \equiv \beta(z \to \infty, z_l)$ (Bartelmann & Schneider 2001). The associated critical surface mass density is $\Sigma_{c,\infty} = c^2/(4\pi G D_l \beta_\infty)$. The source-averaged convergence and shear fields are then expressed as $\langle\kappa\rangle_X = \langle W\rangle_X \kappa_\infty$ and $\langle\gamma\rangle_X = \langle W\rangle_X \gamma_\infty$, using those in the far-background limit. Hereafter, we use the far-background lensing fields, $\kappa_\infty(\boldsymbol{\theta})$ and $\gamma_\infty(\boldsymbol{\theta})$, to describe the projected mass distribution of clusters.

[14] Alternatively, one may constrain the constant λ such that the enclosed mass within a certain aperture is consistent with mass estimates from independent observations (e.g., Umetsu & Futamase 2000). See also Section 4.1.

3. CLUSTER SAMPLE, DATA, AND METHODOLOGY

In this section, we outline the analysis procedure used to combine strong-lensing, weak-lensing shear and magnification data for direct reconstruction of cluster surface mass density profiles. In Section 3.1, we present a summary of the properties of our cluster sample. In Section 3.2, we describe the background galaxy selection for the weak-lensing shear and magnification analysis. In Sections 3.3, 3.4, and 3.5, we describe our methods for measuring cluster lensing profiles as a function of clustercentric radius. In Section 3.6, we outline the joint likelihood approach of Umetsu (2013) to perform a mass profile reconstruction from multi-probe lensing data.

3.1. Cluster Sample

Our cluster sample stems from the CLASH shear-and-magnification weak-lensing analysis of Umetsu et al. (2014) based primarily on Subaru multi-color imaging. This sample comprises two subsamples, one with 16 X-ray regular clusters and another with four high-magnification clusters, both taken from the CLASH sample of Postman et al. (2012).

Table 1 gives a summary of the properties of 20 clusters in our sample. Following Umetsu et al. (2014), we adopt the brightest cluster galaxy (BCG) position as the cluster center for our mass profile analysis. As discussed by Umetsu et al. (2014), our sample exhibits, on average, a small positional offset between the BCG and X-ray peak, characterized by an rms offset of $\sigma_{\rm off} \simeq 30\,{\rm kpc}\,h^{-1}$. For the X-ray-selected subsample, $\sigma_{\rm off} \simeq 11\,{\rm kpc}\,h^{-1}$. This level of offset is negligible compared to the range of overdensity radii of interest for mass measurements ($\Delta_c \lesssim 2500$). Hence, smoothing from the miscentering effects will not significantly affect our cluster mass profile measurements (Johnston et al. 2007; Umetsu et al. 2011a).

3.2. Background Galaxy Selection for Weak Lensing

A careful selection of background galaxies is critical for a cluster weak-lensing analysis, so that unlensed cluster members and foreground galaxies do not dilute the background lensing signal. Umetsu et al. (2014) used the color–color (CC) selection method of Medezinski et al. (2010), typically using the Subaru/Suprim-Cam $B_J R_C z'$ photometry where available (Umetsu et al. 2014, Tables 1 and 2), which spans the full optical wavelength range. The photometric zero points were precisely calibrated to an accuracy of ~0.01 mag, using the *HST* photometry of cluster elliptical galaxies and with the help of galaxies with measured spectroscopic redshifts.

For shape measurements, Umetsu et al. (2014) combined two distinct populations that encompass the red and blue branches of background galaxies in CC-magnitude space, having typical redshift distributions peaked around $z \sim 1$ and ~2, respectively (see Figures 1, 5, and 6 of Medezinski et al. 2011). For validation purposes, we have compared our blue+red background samples with spectroscopic samples obtained from the CLASH-VLT large spectroscopic program with VIMOS (Rosati et al. 2014) providing thousands of spectroscopic redshifts for cluster members and intervening galaxies along the line of sight, including lensed background galaxies (e.g., Balestra et al. 2013; Biviano et al. 2013). Combining CLASH-VLT spectroscopic redshifts with the Subaru multi-band photometry available for 10

Table 1
Properties of the Cluster Sample

Cluster	z_l	R.A.[a] (J2000.0)	decl.[a] (J2000.0)	$k_B T_X$[b] (keV)	θ_{Ein}[c] ($''$)	M_{2D} ($10^{13}\,M_\odot h_{70}^{-1}$)[d] $\theta = 10''$	$\theta = 20''$	$\theta = 30''$	$\theta = 40''$
X-ray Selected:									
Abell 383	0.187	02:48:03.40	−03:31:44.9	6.5 ± 0.24	15.1	1.15 ± 0.17	3.04 ± 0.51	4.98 ± 0.96	6.77 ± 1.35
Abell 209	0.206	01:31:52.54	−13:36:40.4	7.3 ± 0.54	8.9	0.93 ± 0.14	2.36 ± 0.45	3.96 ± 0.89	5.60 ± 1.40
Abell 2261	0.224	17:22:27.18	+32:07:57.3	7.6 ± 0.30	23.1	1.91 ± 0.31	4.79 ± 0.69	7.67 ± 1.26	10.42 ± 1.84
RX J2129.7+0005	0.234	21:29:39.96	+00:05:21.2	5.8 ± 0.40	12.9	1.13 ± 0.18	3.36 ± 0.44	5.95 ± 0.74	8.67 ± 1.10
Abell 611	0.288	08:00:56.82	+36:03:23.6	7.9 ± 0.35	18.1	1.84 ± 0.25	5.25 ± 0.83	9.37 ± 1.82	14.26 ± 3.06
MS2137-2353	0.313	21:40:15.17	−23:39:40.2	5.9 ± 0.30	17.1	2.25 ± 0.33	5.23 ± 0.81	7.99 ± 1.38	10.76 ± 2.00
RX J2248.7-4431	0.348	22:48:43.96	−44:31:51.3	12.4 ± 0.60	31.1	2.47 ± 0.45	7.36 ± 1.02	13.14 ± 1.96	19.41 ± 3.07
MACS J1115.9+0129	0.352	11:15:51.90	+01:29:55.1	8.0 ± 0.40	18.1	1.85 ± 0.37	5.79 ± 0.84	11.09 ± 1.50	16.98 ± 2.37
MACS J1931.8-2635	0.352	19:31:49.62	−26:34:32.9	6.7 ± 0.40	22.2	2.91 ± 0.60	7.37 ± 1.12	12.15 ± 1.86	17.21 ± 2.90
RX J1532.9+3021	0.363	15:32:53.78	+30:20:59.4	5.5 ± 0.40	…	…	…	…	…
MACS J1720.3+3536	0.391	17:20:16.78	+35:36:26.5	6.6 ± 0.40	20.1	2.65 ± 0.35	7.20 ± 1.08	12.39 ± 2.17	17.97 ± 3.36
MACS J0429.6-0253	0.399	04:29:36.05	−02:53:06.1	6.0 ± 0.44	15.7	2.22 ± 0.39	6.80 ± 0.96	12.55 ± 1.86	18.87 ± 3.02
MACS J1206.2-0847	0.440	12:06:12.15	−08:48:03.4	10.8 ± 0.60	26.8	3.37 ± 0.50	9.51 ± 1.39	16.37 ± 2.50	23.18 ± 3.88
MACS J0329.7-0211	0.450	03:29:41.56	−02:11:46.1	8.0 ± 0.50	24.1	3.40 ± 0.62	8.66 ± 1.26	14.36 ± 2.16	21.12 ± 3.17
RX J1347.5-1145	0.451	13:47:31.05	−11:45:12.6	15.5 ± 0.60	33.0	3.56 ± 0.76	11.55 ± 2.14	20.40 ± 3.18	29.25 ± 4.12
MACS J0744.9+3927	0.686	07:44:52.82	+39:27:26.9	8.9 ± 0.80	24.3	4.70 ± 0.92	13.55 ± 2.13	23.64 ± 3.35	34.79 ± 4.57
High Magnification:									
MACS J0416.1-2403	0.396	04:16:08.38	−24:04:20.8	7.5 ± 0.80	25.9	1.33 ± 0.18	5.35 ± 0.79	11.32 ± 1.68	17.43 ± 2.51
MACS J1149.5+2223	0.544	11:49:35.69	+22:23:54.6	8.7 ± 0.90	20.4	2.88 ± 0.51	9.29 ± 1.39	17.80 ± 2.87	28.09 ± 5.07
MACS J0717.5+3745	0.548	07:17:32.63	+37:44:59.7	12.5 ± 0.70	55.0	2.01 ± 0.19	8.04 ± 0.74	18.79 ± 2.01	35.80 ± 5.83
MACS J0647.7+7015	0.584	06:47:50.27	+70:14:55.0	13.3 ± 1.80	26.4	3.62 ± 0.77	11.75 ± 1.84	21.59 ± 3.32	31.95 ± 5.45

Notes.
[a] The cluster center is taken to be the location of the BCG when a single dominant central galaxy is found. Otherwise, in the case of MACS J0717.5+3745 and MACS J0416.1−2403, it is defined as the center of the brightest red-sequence-selected cluster galaxies (Umetsu et al. 2014).
[b] X-ray temperature from Postman et al. (2012).
[c] Effective Einstein radius for a fiducial source at $z_s = 2$ determined from the *HST* strong and weak-shear lensing analysis by Zitrin et al. (2015). The reported values are the average of two different models (where available) of Zitrin et al. (2015). The typical model uncertainty in θ_{Ein} is 10%.
[d] Lensing estimates of the projected cluster mass $M_{2D}(<\theta)$ enclosed within a cylinder of radius θ. The data here are constructed for each cluster by combining two different lens models (where available) of Zitrin et al. (2015). For details, see Section 3.5.

southern CLASH clusters, we find a mean contamination fraction of $(2.4 \pm 0.7)\%$ in our blue+red background regions in CC-magnitude space, where the error accounts for Poisson statistics.

Our magnification-bias measurements are based on flux-limited samples of red background galaxies ($R_C - z' \gtrsim 0.5$, Medezinski et al. 2011). Apparent faint magnitude cuts (m_{lim}) were applied for each cluster in the reddest CC-selection band (typically the Subaru z' band) to avoid incompleteness near the detection limit. The threshold m_{lim} was chosen at the magnitude where the source number counts turn over, and it corresponds on average to the 6σ limiting magnitude within $2''$ diameter aperture. Our CC selection does not cause incompleteness at the faint end in the bluer filters (for a general discussion, see Hildebrandt 2015) because we have deeper photometry in the bluer bands (this is by design, so as to detect the red galaxies; see Broadhurst 1995) and our "CC-red" galaxies are relatively blue in $B_J - R_C$ (Figure 1 of Medezinski et al. 2011).

The mean depths $\langle\beta\rangle$ and $\langle\beta^2\rangle$ of the background samples were estimated using photometric redshifts of individual galaxies determined with the BPZ code (Benítez 2000; Benítez et al. 2004) from our point-spread function (PSF) corrected multi-band photometry (typically with 5 Subaru filters; Table 1 of Umetsu et al. 2014). An excellent statistical agreement was found between the depth estimates $\langle\beta\rangle$ from our BPZ measurements in the cluster fields and those from the COSMOS photometric-redshift catalog (Ilbert et al. 2009), with a median relative offset of 0.27% and an rms field-to-field scatter of 5.0% (Umetsu et al. 2014).

3.3. Reduced Tangential Shear

We use the azimuthally averaged radial profile of the reduced tangential shear $g_+ = \gamma_+/(1-\kappa)$ as the primary constraint from wide-field weak-lensing observations. We adopt the following approximation for the nonlinear corrections to the source-averaged reduced tangential shear $\langle g_+\rangle = \left[\int_0^\infty dz\, \overline{N}_g(z) g_+(z)\right]\left[\int_0^\infty dz\, \overline{N}_g(z)\right]^{-1}$ (Seitz & Schneider 1997):

$$\langle g_+\rangle \approx \frac{\langle W\rangle_g\,[\kappa_\infty(<\theta) - \kappa_\infty(\theta)]}{1 - \kappa_\infty(\theta)\langle W^2\rangle_g/\langle W\rangle_g} = \frac{\langle\gamma_+\rangle}{1 - f_{W,g}\,\langle\kappa\rangle}, \quad (5)$$

where $\langle W\rangle_g$ is the relative lensing strength (Section 2) averaged over the population $N_g(z)$ of source galaxies, $f_{W,g} \equiv \langle W^2\rangle_g/\langle W\rangle_g^2$ is a dimensionless quantity of the order unity, $\langle\kappa\rangle = \langle W\rangle_g\,\kappa_\infty$, and $\langle\gamma_+\rangle = \langle W\rangle_g\,\gamma_{+,\infty}$.

In the present study, we use the weak lensing shear data obtained by Umetsu et al. (2014). The shear analysis pipeline of Umetsu et al. (2014) was implemented based on the procedures described in Umetsu et al. (2010) and on verification tests with mock ground-based observations (Massey et al. 2007; Oguri et al. 2012). The key feature of the shear calibration method of Umetsu et al. (2010) is that we use galaxies detected with very high significance, $\nu > 30$, to model the PSF isotropic correction as function of object size and magnitude. Here ν is the peak significance given by the IMCAT peak-finding algorithm *hfindpeaks*. Recently, a very

similar procedure was used by the Local Cluster Substructure Survey (LoCuSS) collaboration in their Subaru weak-lensing study of 50 clusters (Okabe & Smith 2015). Another important feature is that we select isolated galaxies for the shape measurement to minimize the impact of crowding and blending (Umetsu et al. 2014). To do this, we first identify objects having any detectable neighbor within $3r_g$, with r_g the Gaussian scale length given by *hfindpeaks*. All such close pairs of objects are rejected. After this close-pair rejection, objects with low detection significance $\nu < 10$ are excluded from our analysis. All galaxies with usable shape measurements are then matched with sources in our CC-magnitude-selected background galaxy samples (Section 3.2), ensuring that each galaxy is detected in both the reddest CC-selection band and the shape-measurement band.

Using simulated Subaru/Suprime-Cam images (Massey et al. 2007; Oguri et al. 2012), Umetsu et al. (2010) find that the lensing signal can be recovered with $|m| \sim 0.05$ of the multiplicative shear calibration bias and $c \sim 10^{-3}$ of the residual shear offset (as defined by Heymans et al. 2006; Massey et al. 2007). Accordingly, Umetsu et al. (2014) included for each galaxy a shear calibration factor of $1/(1+m)$ ($g \rightarrow g/0.95$) to account for residual calibration. As noted by (Umetsu et al. 2012), the degree of multiplicative bias m depends modestly on the seeing conditions and the PSF quality (Oguri et al. 2012, see Section 3.2 for their image simulations using Gaussian and Moffat PSF profiles with 0.″5–1.″1 FWHM). This variation with the PSF properties limits the shear calibration accuracy to $\delta m \sim 0.05$ (Umetsu et al. 2012, Section 3.3).

From shape measurements of background galaxies, the averaged reduced tangential shear was measured in a set of concentric annuli ($i = 1, 2, \ldots, N_{\rm WL}$) centered on each cluster as

$$\langle g_{+,i}\rangle = \left[\sum_{k\in i} w_{(k)}\, g_{+(k)}\right]\left[\sum_{k\in i} w_{(k)}\right]^{-1}, \quad (6)$$

where the index k runs over all objects located within the ith annulus, $g_{+(k)}$ is an estimate of g_+ for the kth object, and w_k is its statistical weight given by $w_{(k)} = 1/(\sigma^2_{g(k)} + \alpha_g^2)$, with $\sigma_{g(k)}$ the uncertainty in the estimate of reduced shear g_k and α_g the softening constant taken to be $\alpha_g = 0.4$ (Umetsu et al. 2014), a typical value of the mean dispersion $(\overline{\sigma_g^2})^{1/2}$ in Subaru observations (e.g., Oguri et al. 2009; Umetsu et al. 2009; Okabe et al. 2010). Here α includes both intrinsic shape and measurement noise contributions. The statistical uncertainty $\sigma_{+,i}$ in $\langle g_{+,i}\rangle$ was estimated from bootstrap resampling of the background source catalog for each cluster.

The reduced tangential shear profiles analyzed in this study are presented in Figure 2 of Umetsu et al. (2014). For all clusters in our sample, the estimated values for $\langle\beta\rangle_g$, and $f_{W,g}$ are summarized in Table 3 of Umetsu et al. (2014). We marginalize over the calibration uncertainty of $\langle\beta\rangle_g$ in our joint likelihood analysis of multiple lensing probes (Section 3.6.2).

3.4. Magnification Bias

A fundamental limitation of measuring shear only is the mass-sheet degeneracy (Section 2; see also Section 4.2). We can break this degeneracy by using the complementary combination of shear and magnification (Schneider et al. 2000; Umetsu & Broadhurst 2008; Rozo & Schmidt 2010; Umetsu 2013).

Deep multi-color photometry enables us to explore the faint end of the luminosity function of red quiescent galaxies at $z \sim 1$ (Ilbert et al. 2010). For such a population, the effect of magnification bias is dominated by the geometric area distortion because few fainter galaxies can be magnified up into the flux-limited sample; this results in a net depletion of source counts (Taylor et al. 1998; Broadhurst et al. 2005; Umetsu & Broadhurst 2008; Umetsu et al. 2010, 2011b, 2012, 2014, 2015; Coe et al. 2012; Ford et al. 2012; Medezinski et al. 2013; Radovich et al. 2015). In the regime of negative magnification bias, a practical advantage is that the effect is not sensitive to the exact form of the source luminosity function (Umetsu et al. 2014).

If the magnitude shift $\delta m = 2.5\log_{10}\mu$ of an object due to magnification is small compared to that on which the logarithmic slope of the luminosity function varies, the number counts can be locally approximated by a power law at the limiting magnitude $m_{\rm lim}$. The magnification bias at redshift z is then given by (Broadhurst et al. 1995)

$$N_\mu(\boldsymbol{\theta}, z; <m_{\rm lim}) = \overline{N}_\mu(z)\,\mu^{2.5\,s-1}(\boldsymbol{\theta}, z) \equiv \overline{N}_\mu(z) b_\mu(\boldsymbol{\theta}, z), \quad (7)$$

where $\overline{N}_\mu(z) = \overline{N}_\mu(z; <m_{\rm lim})$ is the unlensed mean source counts and s is the logarithmic count slope evaluated at $m_{\rm lim}$, $s = [d\log_{10}\overline{N}_\mu(z; <m)/dm]_{m=m_{\rm lim}}$. In the regime where $2.5\,s \ll 1$, a net count depletion results. Accounting for the spread of $\overline{N}_\mu(z)$, we express the population-averaged magnification bias as $\langle b_\mu\rangle = \left[\int_0^\infty dz\,\overline{N}_\mu(z) b_\mu(z)\right]\left[\int_0^\infty dz\,\overline{N}_\mu(z)\right]^{-1}$. Following Umetsu et al. (2014), we interpret the observed number counts on a grid of equal-area cells ($n = 1, 2, \ldots$) as (see Appendix A.2 of Umetsu 2013)

$$\langle b_\mu(\boldsymbol{\theta}_n)\rangle = N_\mu(\boldsymbol{\theta}_n; <m_{\rm lim})/\overline{N}_\mu(<m_{\rm lim}) \approx \langle\mu^{-1}(\boldsymbol{\theta}_n)\rangle^{1-2.5 s_{\rm eff}} \quad (8)$$

with $s_{\rm eff} = [d\log_{10}\overline{N}_\mu(<m)/dm]_{m=m_{\rm lim}}$ the effective count slope defined in analogy to Equation (7). Equation (8) is exact for $s_{\rm eff} = 0$ and gives a good approximation for depleted populations with $s_{\rm eff} \ll 0.4$.

The covariance matrix $\mathrm{Cov}[N(\boldsymbol{\theta}_m), N(\boldsymbol{\theta}_n)] \equiv (C_N)_{mn}$ of the source counts includes the clustering and Poisson contributions (Hu & Kravtsov 2003) as $(C_N)_{mn} = (\overline{N}_\mu)^2\omega_{mn} + \delta_{mn}N_\mu(\boldsymbol{\theta}_m)$, with ω_{mn} the cell-averaged angular correlation function of source galaxies (see Equation (14) of Umetsu et al. 2015). The angular correlation length of background galaxies can be small (Connolly et al. 1998; van Waerbeke 2000) compared to the typical resolution $\sim 1'$ of cluster weak lensing, so that the correlation between different cells can be generally ignored, whereas the unresolved and nonvanishing correlation on small angular scales accounts for increase of the variance of counts. We thus approximate C_N by (Umetsu et al. 2015)

$$(C_N)_{mn} \approx [\langle\delta N_\mu^2(\boldsymbol{\theta}_m)\rangle + N_\mu(\boldsymbol{\theta}_m)]\,\delta_{mn}, \quad (9)$$

with $\langle\delta N_\mu^2(\boldsymbol{\theta}_m)\rangle$ being the total variance of the mth counts. To enhance the signal-to-noise ratio (S/N), we calculate the surface number density $n_\mu(\theta) = dN_\mu(\theta)/d\Omega$ of source galaxies as a function of clustercentric radius, by averaging the counts in

concentric annuli centered on the cluster. The source-averaged magnification bias is then expressed as $\langle n_\mu(\theta)\rangle = \bar{n}_\mu \langle \mu^{-1}(\theta)\rangle^{1-2.5s_{\rm eff}}$ with $\bar{n}_\mu$ the unlensed mean surface number density.

We measure the magnification bias signal in each annulus ($i = 1, 2, \ldots, N_{\rm WL}$) as (Umetsu et al. 2015)

$$\langle n_{\mu,i}\rangle = \frac{1}{(1-f_{{\rm mask},i})\Omega_{\rm cell}} \sum_m \mathcal{P}_{im} N_\mu(\boldsymbol{\theta}_m) \tag{10}$$

with $\Omega_{\rm cell}$ being the solid angle of the cell and $\mathcal{P}_{im} = \left(\sum_m A_{mi}\right)^{-1} A_{mi}$ the projection matrix normalized in each annulus as $\sum_m \mathcal{P}_{im} = 1$, here, A_{mi} is the fraction of the area of the mth cell lying within the ith annular bin ($0 \leqslant A_{mi} \leqslant 1$), and $f_{{\rm mask},i}$ is the mask correction factor for the ith annular bin, $(1-f_{{\rm mask},i})^{-1} \equiv \left[\sum_m (1-f_m) A_{mi}\right]^{-1} \sum_m A_{mi}$, with f_m being the fraction of the mask area in the mth cell, due to bad pixels, saturated objects, foreground, and cluster galaxies. The intrinsic clustering plus statistical Poisson contributions to the uncertainty in $\langle n_{\mu,i}\rangle$ are given as

$$(\sigma^{\rm int}_{\mu,i})^2 + (\sigma^{\rm stat}_{\mu,i})^2 = \frac{1}{(1-f_{{\rm mask},i})^2 \Omega^2_{\rm cell}} \sum_m \mathcal{P}^2_{im} (C_N)_{mm}, \tag{11}$$

where $(\sigma^{\rm int}_\mu)^2$ and $(\sigma^{\rm stat}_\mu)^2$ account for the contributions from the first and second terms of Equation (9), respectively.

In the present work, we use magnification measurements from flux-limited samples of red background galaxies obtained by Umetsu et al. (2014). The analysis procedure used in Umetsu et al. (2014) is summarized as follows: The magnification bias analysis was limited to the $24' \times 24'$ region centered on the cluster. The clustering error term $\sigma^{\rm int}_{\mu,i}$ was estimated empirically from the variance in each annulus due to variations of the counts along the azimuthal direction. For the estimation of $\langle n_{\mu,i}\rangle$, a positive tail of $>\nu\sigma$ cells with $\nu = 2.5$ was excluded in each annulus by iterative σ clipping to reduce the bias due to intrinsic angular clustering of source galaxies. The Poisson error term $\sigma^{\rm stat}_{\mu,i}$ was estimated from the clipped mean counts. The systematic change between the mean counts estimated with and without σ clipping was then taken as a systematic error, $\sigma^{\rm sys}_{\mu,i} = |n^{(\nu)}_{\mu,i} - n^{(\infty)}_{\mu,i}|/\nu$, where $n^{(\nu)}_{\nu,i}$ and $n^{(\infty)}_{\mu,i}$ represent the clipped and unclipped mean counts in the ith annulus, respectively. As noted by Umetsu et al. (2014), the $\sigma^{\rm sys}_\mu$ term is sensitive to large-scale variations of source counts and can in principle account for projection effects from background clusters along the line of sight and spurious excess counts due perhaps to spatial variation of the photometric zero point and/or to residual flat-field errors. These errors were combined in quadrature as

$$\sigma^2_{\mu,i} = (\sigma^{\rm int}_{\mu,i})^2 + (\sigma^{\rm stat}_{\mu,i})^2 + (\sigma^{\rm sys}_{\mu,i})^2. \tag{12}$$

Since we include the $\sigma^{\rm sys}_\mu$ term in the error analysis, our magnification bias measurements are stable and insensitive to the particular choice of ν. The smaller the ν value, the larger the resulting total errors as dominated by the Poisson and systematic terms.

The count normalization and slope parameters ($\bar{n}_\mu$, $s_{\rm eff}$) were estimated from the source counts in the outskirts at $10' \leqslant \theta \leqslant \theta_{\rm max}$, with $\theta_{\rm max} = 16'$ except $\theta_{\rm max} = 14'$ for RX J2248.7−4431 observed with ESO/WFI (Umetsu et al. 2014). The mask-corrected magnification bias profile $\langle n_{\mu,i}\rangle/\bar{n}_\mu$ is thus proportional to $(1-f_{\rm mask,back})/(1-f_{{\rm mask},i}) \equiv 1 + \Delta f_{{\rm mask},i}$ with $f_{\rm mask,back} = f_{\rm mask}\,(10' \leqslant \theta \leqslant \theta_{\rm max})$ the masked area fraction in the reference background region. Masking of observed sky was accounted for using the method outlined in Umetsu et al. (2011b, Method B of Appendix A). This method can be fully automated to achieve similar performance to conservative approaches (e.g., Method A of Umetsu et al. 2011b) in terms of the masked area fraction once the configuration parameters of SExtractor (Bertin & Arnouts 1996) are optimally tuned. We tuned the SExtractor configuration parameters by setting `DETECT_THRESH = 5` and `DETECT_MINAREA = 300` as found by Umetsu et al. (2011b) to detect foreground objects, cluster galaxies, and defects (e.g., saturated stars and stellar trails) in the coadded images ($0\farcs2$ pixel^{-1} sampling). We marked the pixels that belong to these objects in the `CHECKIMAGE_TYPE = OBJECT` mode. Recently, Chiu et al. (2015) adopted this method to calculate the masked area fraction for their magnification bias measurements, finding that the SExtractor configuration of Umetsu et al. (2011b) is optimal for their observations with Megacam on the *Magellan* Clay telescope.

We find that the unmasked area fraction $1 - f_{\rm mask}$ is on average 93% of the sky at $\theta \geqslant 10'$, decreasing toward the cluster center down to 88% at $1' \lesssim \theta \lesssim 2'$ ($210\,{\rm kpc}\,h^{-1} \lesssim R \lesssim 420\,{\rm kpc}\,h^{-1}$ at $z = 0.35$). The typical variation of the mask correction factor across the radial range is thus $\approx \max(f_{\rm mask}) - f_{\rm mask,back} \sim 5\%$, which is much smaller than the typical depletion signal $\delta n_\mu/\bar{n}_\mu \sim -0.3$ in the innermost radial bin [$0\farcm9$, $1\farcm2$]. Hence, the uncertainty in the mask correction is of the second order. Furthermore, the net effect of the mask correction depends on the difference of the $f_{\rm mask}$ values, $\Delta f_{{\rm mask},i} \approx f_{{\rm mask},i} - f_{\rm mask,back}$ and is insensitive to the particular choice of the SExtractor configuration parameters. Accordingly, the systematic uncertainty on the mask correction is negligible.

The magnification-bias profiles used in this study are presented in Figure 2 of Umetsu et al. (2014). For all clusters, the estimated values and errors for $\langle\beta\rangle_\mu$, $\bar{n}_\mu$, and $s_{\rm eff}$ are summarized in Table 4 of Umetsu et al. (2014). The observed values of $s_{\rm eff}$ range from 0.11 to 0.20, with a mean of $\langle s_{\rm eff}\rangle = 0.153$ and a typical uncertainty of 33% per cluster field. We marginalize over the calibration parameters ($\langle\beta\rangle_\mu$, $\bar{n}_\mu$, $s_{\rm eff}$) for each cluster in our joint likelihood analysis of multiple lensing probes (Section 3.6.2).

3.5. Strong Lensing

Detailed strong-lens modeling using many sets of multiple images with known redshifts allows us to determine the critical curves with great accuracy, which then provides accurate estimates of the projected mass enclosed within the critical area $A_{\rm c}$ of an effective Einstein radius $\theta_{\rm Ein} = \sqrt{A_{\rm c}/\pi}$ (Zitrin et al. 2015).[15] The enclosed projected mass profile

$$\begin{aligned} M_{\rm 2D}(<\theta) &= \Sigma_{\rm c} D_{\rm l}^2 \int_{|\boldsymbol{\theta}'|\leqslant\theta} \kappa(\boldsymbol{\theta}')\, d^2\theta' \\ &= \pi (D_{\rm l}\theta)^2 \Sigma_{{\rm c},\infty} \kappa_\infty(<\theta). \end{aligned} \tag{13}$$

at the location θ around $\theta_{\rm Ein}$ is less sensitive to modeling assumptions and approaches (see Coe et al. 2010; Oguri et al. 2012; Umetsu et al. 2012), serving as a fundamental observable quantity in the strong-lensing regime (Coe et al. 2010).

[15] For an axisymmetric lens, the average mass density within this critical area is equal to $\Sigma_{\rm c}$, thus enabling us to directly estimate the enclosed projected mass by $M_{\rm 2D}(<\theta_{\rm Ein}) = \pi (D_{\rm l}\theta_{\rm Ein})^2 \Sigma_{\rm c}$.

In this work, we use the recent *HST* results from a joint analysis of CLASH strong- and weak-lensing data presented by Zitrin et al. (2015), who have obtained detailed mass models for each cluster core using two distinct parameterizations (when applicable): One assumes light-traces-mass for both galaxies and DM, while the other adopts an analytical elliptical NFW form for the DM-halo components. Zitrin et al. (2015) performed a detailed comparison of the two models to obtain a realistic, empirical assessment of the true underlying errors, finding that the projected mass enclosed within the critical curves ($z_s = 2$) agrees typically within ∼15%. Zitrin et al. (2015) recommended replacing the statistical errors of their models with the actual (and much larger) uncertainties that account for model-dependent systematics.

We combine for each cluster the constraints on $M_{2D}(<\theta)$ from two distinct mass models (where available) of Zitrin et al. (2015). To do this, we take a conservative approach that accounts for model-dependent systematic uncertainties. First, at each projected clustercentric distance θ, we improve our estimation of $M_{2D}(<\theta)$ using the average of two different methods as $M_{2D} = (M_{Z1} + M_{Z2})/2$. Next, we combine the 1σ confidence intervals of the two models, by taking the maximum range spanned by their respective confidence limits as an overall total uncertainty, $\sigma_M = [\max(M_{Z1} + \sigma_{Z1}, M_{Z2} + \sigma_{Z2}) - \min(M_{Z1} - \sigma_{Z1}, M_{Z2} - \sigma_{Z2})]/2$. Finally, we rescale the error profile $\sigma_M(\theta)$ such that the fractional uncertainty on $M_{2D}(<\theta_{Ein})$ is 15%, as motivated by the findings of Zitrin et al. (2015). For all clusters, this has resulted in increased errors.

Now, the question is how to determine an effective sampling radius $\Delta\theta$ of projected mass constraints $M_{2D}(<\theta)$, avoiding oversampling and reducing correlations between adjacent bins. Following Coe et al. (2010), we estimate here the effective resolution $\Delta\theta$ based on the surface density of observed multiple images as $N_{im}(\Delta\theta)^2 = \pi\theta_{Ein}^2$ with N_{im} the number of multiple images. For our cluster sample, we find a median of $\overline{N}_{im} = 17$ multiple images per cluster and a median effective Einstein radius of $\overline{\theta}_{Ein} = 22\farcs3$ for a fiducial source redshift of $z_s = 2$ (Table 1), yielding $\Delta\theta \approx 10''$. This is consistent with the typical map resolutions in the strong-lensing regime adopted by the SaWLens analysis of Merten et al. (2015, see their Table 5). For the X-ray-selected subsample, we find a median value of $\overline{\theta}_{Ein} = 20\farcs1$ at $z_s = 2$. The maximum integration radius is taken to be $40''$, which is equal to approximately twice the median Einstein radius ($z_s = 2$), the region where multiple images form (see Section 3 of Zitrin et al. 2012a).

To summarize, for each cluster except RX J1532.9+3021 for which no secure identification of multiple images has been made (Zitrin et al. 2015), we obtain enclosed projected mass constraints $\{M_{2D,i}\}_{i=1}^{N_{SL}} \equiv \{M_{2D}(<\theta_i)\}_{i=1}^{N_{SL}}$ for a set of $N_{SL} = 4$ fixed integration radii $\theta_i = 10''$, $20''$, $30''$, and $40''$ from the *HST* lensing analysis of Zitrin et al. (2015). A summary of the *HST* lensing mass estimates is given in Table 1.

3.6. Cluster Mass Profile Reconstruction

3.6.1. Lensing Constraints

We consider multiple complementary lensing information available in the cluster regime, namely enclosed projected mass estimates from strong lensing, source-averaged tangential distortion and magnification bias measurements:

$$\{M_{2D,i}\}_{i=1}^{N_{SL}},\ \{\langle g_{+,i}\rangle\}_{i=1}^{N_{WL}},\ \{\langle n_{\mu,i}\rangle\}_{i=1}^{N_{WL}}. \tag{14}$$

Hence, there are a total of $N_{GL} \equiv N_{SL} + 2N_{WL}$ independent lensing constraints for each cluster.

Umetsu et al. (2014) measured the shear and magnification effects in $N_{WL} = 10$ log-spaced clustercentric radial bins over the range $[0\farcm9, 16']$ for all clusters, except $[0\farcm9, 14']$ for RX J2248.7−4431 observed with ESO/WFI (Section 3.4). We have $N_{SL} = 4$ projected mass estimates (Table 1) from the *HST* lensing analysis of Zitrin et al. (2015) for all clusters except RX J1532.9+3021 without strong-lensing constraints.

3.6.2. Joint Likelihood Function

In the Bayesian framework of Umetsu (2013, see also Umetsu et al. 2011b), the lensing signal is described by a vector $\boldsymbol{s}$ of parameters containing the binned convergence profile $\{\kappa_{\infty,i}\}_{i=1}^{N}$ with $N \equiv N_{SL} + N_{WL}$, given by N binned κ values and the average convergence enclosed by the innermost aperture radius θ_{min} for strong-lensing mass estimates, $\kappa_{\infty,min} \equiv \kappa_\infty(<\theta_{min})$,[16] so that

$$\boldsymbol{s} = \{\kappa_{\infty,\min},\ \kappa_{\infty,i}\}_{i=1}^{N} \equiv \Sigma_{c,\infty}^{-1}\boldsymbol{\Sigma} \tag{15}$$

specified by $(N + 1)$ parameters. We have $N = 14$ for all clusters except $N = N_{WL} = 10$ for RX J1532.9+3021 (Section 3.6.1). The number of degrees of freedom (dof) is $N_{GL} - (N + 1) = N_{WL} - 1 = 9$ for all clusters.

The joint likelihood function $\mathcal{L}_{GL}(\boldsymbol{s})$ for multi-probe lensing observations is given as a product of their separate likelihoods,

$$\mathcal{L}_{GL} = \mathcal{L}_{SL}\mathcal{L}_{WL} = \mathcal{L}_{SL}\mathcal{L}_g\mathcal{L}_\mu, \tag{16}$$

with $\mathcal{L}_{SL}$, $\mathcal{L}_g$, and $\mathcal{L}_\mu$ the likelihood functions for $\{M_{2D,i}\}_{i=1}^{N_{SL}}$, $\{\langle g_{+,i}\rangle\}_{i=1}^{N_{WL}}$, and $\{\langle n_{\mu,i}\rangle\}_{i=1}^{N_{WL}}$, respectively, defined as

$$\begin{aligned}
\ln\mathcal{L}_{SL} &= -\frac{1}{2}\sum_{i=1}^{N_{SL}}\frac{[M_{2D,i} - \hat{M}_{2D,i}(\boldsymbol{s})]^2}{\sigma_{M,i}^2},\\
\ln\mathcal{L}_g &= -\frac{1}{2}\sum_{i=1}^{N_{WL}}\frac{[\langle g_{+,i}\rangle - \hat{g}_{+,i}(\boldsymbol{s},\boldsymbol{c})]^2}{\sigma_{+,i}^2},\\
\ln\mathcal{L}_\mu &= -\frac{1}{2}\sum_{i=1}^{N_{WL}}\frac{[\langle n_{\mu,i}\rangle - \hat{n}_{\mu,i}(\boldsymbol{s},\boldsymbol{c})]^2}{\sigma_{\mu,i}^2},
\end{aligned} \tag{17}$$

with $(\hat{M}_{2D}, \hat{g}_+, \hat{n}_\mu)$ the theoretical predictions for the corresponding observations (Appendix A) and $\boldsymbol{c}$ the calibration nuisance parameters to marginalize over,

$$\boldsymbol{c} = \{\langle W\rangle_g, f_{W,g}, \langle W\rangle_\mu, \overline{n}_\mu, s_{eff}\}. \tag{18}$$

For each parameter of the model $\boldsymbol{s}$, we consider a flat uninformative prior with a lower bound of $\boldsymbol{s} = 0$. Additionally, we account for the calibration uncertainty in the observational parameters $\boldsymbol{c}$.

3.6.3. Estimators and Covariance Matrix

We implement our method using a Markov Chain Monte Carlo algorithm with Metropolis–Hastings sampling following the prescription outlined in Umetsu et al. (2011b). The method has been tested (Umetsu 2013) with synthetic weak-lensing catalogs from simulations of analytical NFW lenses performed using the public package GLAFIC (Oguri 2010). The results

[16] If no strong-lensing constraint is available ($N_{SL} = 0$), $\kappa_{\infty,min}$ represents the average convergence within the inner radial boundary of weak-lensing observations, $\theta_{min} = 0\farcm9$ (Umetsu et al. 2014).

suggest that, when the mass-sheet degeneracy is broken, both maximum-likelihood (ML) and marginal maximum a posteriori probability (MMAP) solutions provide reliable reconstructions with unbiased profile measurements. Hence, this method is not sensitive to the choice and form of priors. In the presence of a systematic bias in the background-density constraint ($\bar{n}_\mu$), the global ML estimator is less sensitive to systematic effects than MMAP, and provides more accurate reconstructions (Umetsu et al. 2014).

On the basis of our simulations, we thus use the global ML estimator for the determination of the mass profile. In our error analysis we take into account statistical, systematic, cosmic-noise, and intrinsic-variance contributions to the total covariance matrix $C_{ij} \equiv \mathrm{Cov}(s_i, s_j)$ for $\kappa_\infty = \Sigma/\Sigma_{\mathrm{c},\infty}$ as

$$C = C^{\mathrm{stat}} + C^{\mathrm{sys}} + C^{\mathrm{lss}} + C^{\mathrm{int}}, \tag{19}$$

where C^{stat} is the posterior covariance matrix that is derived from the data (Equations (16) and (17)) by calculating the sample covariance matrix $C_{ij}^{\mathrm{stat}} = \langle (s_i - \langle s_i \rangle)(s_j - \langle s_j \rangle) \rangle$ using MCMC-sampled posterior distributions; C^{sys} accounts for systematic errors due primarily to the mass-sheet uncertainty (Umetsu et al. 2014),

$$(C^{\mathrm{sys}})_{ij} = (\boldsymbol{s}_{\mathrm{ML}} - \boldsymbol{s}_{\mathrm{MMAP}})_i^2 \delta_{ij}, \tag{20}$$

with $\boldsymbol{s}_{\mathrm{ML}}$ and $\boldsymbol{s}_{\mathrm{MMAP}}$ the ML and MMAP solutions, respectively; C^{lss} is due to uncorrelated large-scale structure (LSS) projected along the line of sight (Hoekstra 2003; Umetsu et al. 2011a); C^{int} accounts for the intrinsic variations of the projected cluster mass profile (Gruen et al. 2015).

The cosmic-noise covariance due to projected uncorrelated LSS is given as (Umetsu et al. 2011a)

$$(C^{\mathrm{lss}})_{ij} = \int \frac{ldl}{2\pi} C_{(ij)}^{\kappa\kappa} \hat{J}_0(l\theta_i) \hat{J}_0(l\theta_j), \tag{21}$$

where $C_{(ij)}^{\kappa\kappa}$ is the weak-lensing cross power spectrum as a function of angular multipole l evaluated for a given pair of source populations in the ith and jth radial bins; $\hat{J}_0(/\theta_i)$ is the Bessel function of the first kind and order zero (J_0) averaged over the ith annulus between $\theta_{i,1}$ and $\theta_{i,2}$ ($>\theta_{i,1}$), given as (Umetsu et al. 2011a)

$$\hat{J}_0(l\theta_i) = \frac{2}{(l\theta_{i,2})^2 - (l\theta_{i,1})^2} [l\theta_{i,2} J_1(l\theta_{i,2}) - l\theta_{i,1} J_1(l\theta_{i,1})]. \tag{22}$$

We compute the elements of the C^{lss} matrix for a given pair of source populations, using the nonlinear matter power spectrum of Smith et al. (2003) for the *Wilkinson Microwave Anisotropy Probe* (*WMAP*) seven-year cosmology (Komatsu et al. 2011), and then scale to the reference far-background source plane. For the inner radial bins constrained by *HST* strong lensing, we assume a source plane at $z_{\mathrm{s}} = 2$, which is a typical redshift of strongly lensed background galaxies (Zitrin et al. 2015). For the outer weak-lensing bins, we use for each cluster the effective mean source redshift ($\bar{z}_{\mathrm{eff}}$) estimated with multi-band photometric redshifts (see Table 3 of Umetsu et al. 2014). The cross covariance terms between the strong- and weak-lensing bins are computed using the lensing window functions of the respective populations (Takada & White 2004). For a given depth of observations, the impact of cosmic noise is most important where the cluster signal itself is small (Hoekstra 2003).

The intrinsic covariance matrix C^{int} accounts for the intrinsic variations of the projected cluster density profile (i.e., cluster signal itself) due to the c–M variance, halo asphericity, and the presence of correlated halos (Gruen et al. 2015).[17] In the present work, we consider the diagonal form of the C^{int} matrix,

$$(C^{\mathrm{int}})_{ij} = \alpha_{\mathrm{int}}^2 \times (\boldsymbol{s}_{\mathrm{ML}})_i^2 \delta_{ij}, \tag{23}$$

where the coefficient $\alpha_{\mathrm{int}} \approx \sqrt{C_{ii}^{\mathrm{int}}} \big/ \kappa_{\infty,i}$ represents the fractional intrinsic scatter in κ. On the basis of semi-analytical calculations calibrated by cosmological numerical simulations (Gruen et al. 2015), we find that, for CLASH clusters with a characteristic mass of $M_{200\mathrm{c}} \approx 10^{15}\, M_\odot h^{-1}$ (Umetsu et al. 2014), the diagonal part of the C^{int} matrix can be well approximated by Equation (23) with $\alpha_{\mathrm{int}} \approx 0.2$ in the one-halo regime at $R \lesssim r_{200\mathrm{m}}$. In general, the diagonal approximation to C^{int} can lead to an underestimate of cluster parameters (see Gruen et al. 2015), where the degree of underestimation depends on the radial binning scheme for cluster lensing measurements.

We have tested the validity of this approximation in our radial binning scheme by comparing against the semi-analytical model of Gruen et al. (2015). For a cluster halo of $M_{200\mathrm{c}} = 10^{15}\, M_\odot h^{-1}$ at $z_{\mathrm{l}} = 0.35$ ($M_{200\mathrm{m}} \simeq 13 \times 10^{14}\, M_\odot h^{-1}$) matching approximately the average characteristics of the CLASH sample (Umetsu et al. 2014), we find that the total S/N estimated using the diagonal approximation with $\alpha_{\mathrm{int}} = 0.2$ is accurate to about 10% in the regime of our cluster lensing observations (S/N $\sim$ 10 per cluster), where the S/N is defined as (Umetsu & Broadhurst 2008)[18]

$$(\mathrm{S/N})^2 = \sum_{i,j} s_i C_{ij}^{-1} s_j = \boldsymbol{s}^t C^{-1} \boldsymbol{s}, \tag{24}$$

with C the total covariance matrix defined in Equation (19). In the present study, we thus adopt $\alpha_{\mathrm{int}} = 0.2$ in Equation (23) to account for the effects of the intrinsic profile variations in projection space.[19]

4. CLASH INDIVIDUAL CLUSTER ANALYSIS

In this section we carry out a comprehensive analysis of strong-lensing, weak-lensing shear and magnification data sets for all 20 CLASH clusters in our sample.

4.1. CLASH Mass Profile Reconstruction

Following the methodology outlined in Section 3, we analyze our weak- and strong-lensing data presented in Umetsu et al. (2014) and Zitrin et al. (2015) to examine the underlying radial

[17] Gruen et al. (2015) formally include the contribution from the projected uncorrelated LSS in C^{int}. In this study, we separately account for this external contribution as C^{lss}, to be consistent with the procedure in Umetsu et al. (2014).

[18] We note that this classical S/N definition beaks down in the noise-dominated regime. In our analysis, the binning scheme was chosen such that the per-pixel detection S/N is $\gtrsim$1 for each cluster (Umetsu et al. 2014), and thus the noise contribution to this estimator is negligibly small.

[19] Strictly speaking, when simultaneously determining the mass and concentration for a given individual cluster, the contribution from the intrinsic c–M variance should be excluded from C^{int}. To simplify the procedure, however, we shall fix $\alpha_{\mathrm{int}} = 0.2$ throughout this study. We note that the effect of the c–M variance becomes important only at small cluster radii, $\theta \lesssim 2'$ (Gruen et al. 2015).

mass distribution for a sample of 20 CLASH clusters (Table 1). We have derived for each cluster a mass-profile solution $\mathbf{\Sigma} \equiv \Sigma_{c,\infty}\boldsymbol{s} = \{\Sigma_{\rm min}, \Sigma_i\}_{i=1}^N$ from a joint likelihood analysis of our strong-lensing, weak-lensing shear and magnification data. We find that the minimum $\chi^2 (= -2\ln \mathcal{L}_{\rm GL})$ values for the best-fit Σ solutions range from $\chi^2 = 2.5$ (Abell 611) to 14.8 (MACS J0429.6−0253) for 9 dof (a mean reduced χ^2 of 0.95), indicating good consistency between independent observations having different systematics.

In Appendix B (Figure 11) we show the resulting mass-profile solutions, $\mathbf{\Sigma}$ (black squares), obtained for our sample along with those by Umetsu et al. (2014, blue circles) and Merten et al. (2015, red dots). Umetsu et al. (2014) derived weak-lensing-only solutions for this sample from a joint likelihood analysis of the shear and magnification measurements. When the inner strong-lensing information (Table 1) is combined with wide-field weak-lensing data, the central weak-lensing bin $\Sigma(<0.'9)$ (Section 3.6.1) is resolved into $(N_{\rm SL}+1)$ radial bins, hence improving the determination of the inner mass profile. Merten et al. (2015) performed a two-dimensional SaWLens analysis of 19 CLASH X-ray-selected clusters, by combining the CLASH *HST* data with the shear catalogs of Umetsu et al. (2014). To break the mass-sheet degeneracy, Merten et al. (2015) assumed outer boundary conditions such that the average convergence vanishes at the edge of the reconstruction. This is a reasonable approximation in wide-field weak-lensing observations entailing the full cluster field well beyond its virial radius, $r_{\rm vir}$.

We find overall good agreement between different reconstructions, except for a few systems in the overlap sample, such as MACS J1931.8−2635, RX J1347.5−1145, and MACS J0744.9+3927. For these clusters, the SaWLens reconstructions are systematically lower than those of this work and Umetsu et al. (2014) which include the weak-lensing magnification data. Here MACS J1931.8−2635 ($b = -20.^\circ09$) and MACS J0744.9+3927 ($b = +26.^\circ65$) are the two lowest Galactic latitude clusters of the overlap sample, implying higher stellar densities, correspondingly large areas masked by bright saturated stars, and hence lower number densities of background galaxies usable for weak lensing (Umetsu et al. 2014, see their Figure 2, Tables 3 and 4). In fact, MACS J1931.8−2635 has the lowest S/N of the weak-lensing observations presented in Umetsu et al. (2014, Table 5). On the other hand, RX J1347.5−1145 ($z = 0.451$) and MACS J0744.9+3927 ($z = 0.686$) represent the two highest-z clusters of the overlap sample, both of which exhibit complex mass distributions with a high degree of substructure (see Postman et al. 2012; Merten et al. 2015). For clusters at lower Galactic latitudes and higher redshifts, the color selection of background galaxies is correspondingly more difficult. Therefore, this discrepancy can be attributed in part to systematic uncertainties in the present calibration of magnification measurements for these low Galactic latitude clusters and high-redshift clusters. Weak-lensing mass reconstructions are sensitive to the treatment of boundary conditions if there are massive structures near the data boundaries. Hence, mass profile reconstructions for clusters with high degrees of substructure can be subject to a greater degree of mass-sheet degeneracy. A more quantitative comparison with the SaWLens results from Merten et al. (2015) can be found in Sections 7.3 and 7.4.

Figure 1 shows the average contributions to the total covariance matrix C (Equation (19)) for the convergence profile $\kappa(\theta)$ reconstructed from the joint likelihood analysis of strong-lensing, weak-lensing shear and magnification data. The results are obtained by averaging over 18 clusters observed with both *HST* and Subaru (i.e., all except RX J1532.9+3021 without strong-lensing constraints and RX J2248.7−4431 based on ESO/WFI data). The diagonal variance terms Var(κ), scaled to the mean depth of Subaru weak-lensing observations, are shown as a function of clustercentric radius θ. At all bins except the innermost bin, the reconstruction uncertainty is dominated by the observational statistical errors ($C^{\rm stat}$, red dashed). The relative contribution from intrinsic variance ($C^{\rm int}$, gray solid) increases toward the cluster center and becomes important at small cluster radii, $\theta \lesssim 2'$. The $C^{\rm sys}$ term (green dotted) represents the level of residual variance (Equation (20)) due primarily to the mass-sheet degeneracy. In the regime of Subaru weak-lensing ($\theta \geqslant 0.'9$), $C^{\rm sys}$ stays approximately constant at $\sim(2-4)\times10^{-4}$ with θ, corresponding to a characteristic mass-sheet uncertainty of $\sigma_\kappa \sim (1-2)\times10^{-2}$ per cluster. A noticeable increase of the cosmic-noise contribution $C^{\rm lss}$ (blue dotted–dashed) from projected uncorrelated LSS is seen at $\theta \leqslant 40''$, within which the reconstruction is dominated by *HST* strong-lensing measurements with greater depth.

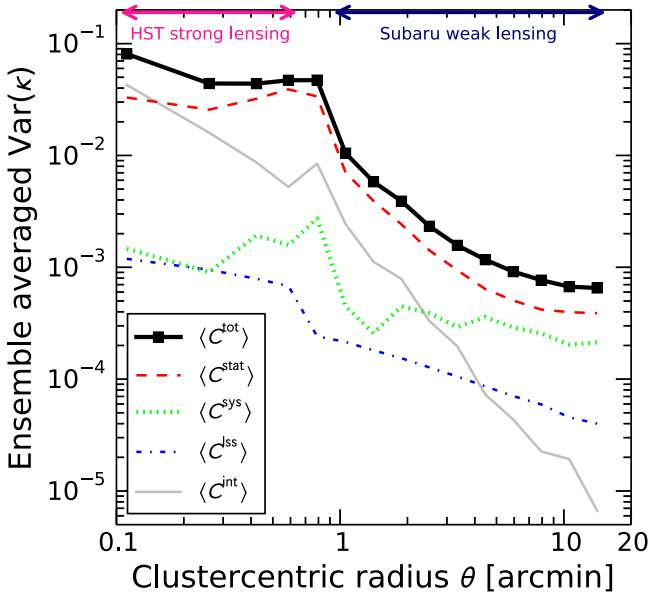

Figure 1. Contributions to the total covariance matrix $C = C^{\rm stat} + C^{\rm sys} + C^{\rm lss} + C^{\rm int}$ (black line with squares) for the binned cluster convergence profile $\kappa(\theta)$ (see Figure 11) reconstructed from a joint likelihood analysis of strong-lensing, weak-lensing shear and magnification data sets. The results are obtained by averaging over 18 clusters observed with both *HST* and Subaru (i.e., all except RX J1532.9+3021 without strong-lensing constraints and RX J2248.7−4431 based on ESO/WFI data). The diagonal variance terms Var(κ), scaled to the mean depth of Subaru weak-lensing observations, are shown as a function of clustercentric radius θ.

In Figure 2, we show the cross-correlation coefficients of the ensemble-averaged $C^{\rm stat}$ and $C^{\rm lss}$ matrices, whose diagonal elements are shown in Figure 1. We find that adjacent *HST* bins of the $\langle C^{\rm stat}\rangle$ matrix are anti-correlated at around the 40% level, where the first 4 bins in each panel of Figure 2 correspond to the *HST* data. This negative covariance arises because they are to satisfy the observed cumulative mass constraints (Equation (13)). We find small correlations of <1% between the *HST* ($10'' \leqslant \theta \leqslant 40''$) and Subaru ($0.'9 \leqslant \theta \leqslant 16'$) radial bins. For

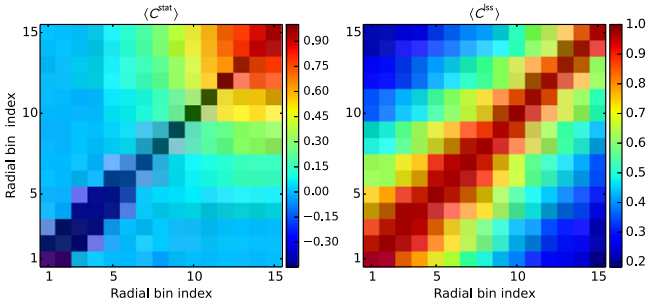

Figure 2. Cross-correlation coefficients of the ensemble-averaged $C^{\rm stat}$ (left panel) and $C^{\rm lss}$ (right panel) matrices, whose diagonal elements are shown in Figure 1.

the $\langle C^{\rm lss}\rangle$ matrix, since strongly lensed source galaxies at $z_{\rm s}\sim 2$ and weakly lensed source galaxies at $z_{\rm s}\sim 1$ behind a given cluster share the same mass overdensities at $z\lesssim 1$ where the geometrical lensing efficiency for the $z_{\rm s}\sim 2$ sources is large, there are large positive correlations at the ∼70%–20% levels between the *HST* and Subaru bins, where the degree of correlation increases with decreasing projected separation.

4.2. Weighing CLASH Clusters

Tangential shear fitting with a spherical NFW profile is a standard approach for measuring individual cluster masses from weak lensing (Umetsu et al. 2009; Okabe et al. 2010; Applegate et al. 2014). Numerical simulations suggest that these mass estimates tend to be biased low (by ∼5%–10%; see Meneghetti et al. 2010; Becker & Kravtsov 2011; Rasia et al. 2012) because local substructures that are abundant in cluster outskirts dilute the shear tangential to the cluster center. This bias can be reduced if the fitting range is restricted to within $\sim 2r_{\rm 500c}\sim r_{\rm vir}$ (Becker & Kravtsov 2011). In the CLASH survey, the availability of multi-probe, multi-scale lensing data allows us to combine weak shear lensing with magnification and/or strong-lensing constraints (Umetsu et al. 2014; Merten et al. 2015). In particular, the complementary combination of shear and magnification data enables to effectively break the mass-sheet degeneracy and reconstruct the total mass distribution Σ (Umetsu et al. 2011b).

Here we revisit the mass estimates for CLASH clusters using our improved mass profile data set (Figure 11) and taking into account the intrinsic contribution ($C^{\rm int}$) to the error covariance matrix (Section 3.6.3). We follow the Bayesian approach of Umetsu et al. (2014) to make inference on the NFW halo parameters. We employ the radial dependence of the projected NFW profiles given by Wright & Brainerd (2000), which provides a good description of the projected mass distribution in the one-halo regime, at least in an ensemble-average sense (Oguri & Hamana 2011; Umetsu et al. 2011a; Okabe et al. 2013). We restrict the fitting range to $R\leqslant 2\,{\rm Mpc}\,h^{-1}$ (Umetsu et al. 2014; Merten et al. 2015), which is close to the virial radius for most CLASH clusters. We specify the two-parameter NFW model using the halo mass $M_{\rm 200c}$ and the halo concentration $c_{\rm 200c}=r_{\rm 200c}/r_{-2}$ with r_{-2} the characteristic radius at which the logarithmic density slope is -2 (Section 5.2.1). We adopt uninformative log-uniform priors in the respective intervals $0.1\leqslant M_{\rm 200c}/(10^{15}\,M_\odot\,h^{-1})\leqslant 10$ and $0.1\leqslant c_{\rm 200c}\leqslant 10$ (Umetsu et al. 2014). We check that the mass and concentration estimates for the CLASH sample are not sensitive to the choice of the priors as found by Sereno et al. (2015b, see their Section 2.1). The χ^2 function for our observations is

$$\chi^2(\boldsymbol{p})=\sum_{i,j}[s_i-\hat{s}_i(\boldsymbol{p})]\,C_{ij}^{-1}[s_j-\hat{s}_j(\boldsymbol{p})], \tag{25}$$

where $\boldsymbol{p}=(M_{\rm 200c},\,c_{\rm 200c})$, and $\hat{s}_i(\boldsymbol{p})=\hat{\Sigma}_i(\boldsymbol{p})/\Sigma_{\rm c,\infty}$ is the predicted surface mass density averaged over the ith annulus, accounting for the effect of bin averaging (Umetsu et al. 2014).

In Table 2, we give marginalized constraints on the NFW halo parameters ($M_{\rm 200c}$, $c_{\rm 200c}$) and the characteristic radius r_{-2}. Throughout this paper, we employ the biweight estimators of Beers et al. (1990) for the central location ($C_{\rm BI}$) and scale ($S_{\rm BI}$) of the marginalized posterior distributions (Sereno & Umetsu 2011; Umetsu et al. 2014, 2015). From the posterior samples, we also derive marginalized constraints on the total enclosed mass $M_\Delta=M_{\rm 3D}(<r_\Delta)$ at several characteristic interior overdensities Δ (see Section 1). Table 3 summarizes the results of our cluster mass estimates. The median precision on our lensing mass measurements is found to be ∼28% at $\Delta_{\rm c}=200$, ∼24% at $\Delta_{\rm c}=500$, ∼23% at $\Delta_{\rm c}=1000$, and ∼24% at $\Delta_{\rm c}=2500$.

In the CLASH weak-lensing study of Umetsu et al. (2014), the $C^{\rm int}$ contribution (Equation (23)) to the total covariance matrix (Equation (19)) was not included in their individual cluster mas measurements at $\Delta_{\rm c}\leqslant 500$. Accordingly, their individual mass measurement errors were underestimated by ∼20% at $\Delta_{\rm c}=200$, on average (see also Figure 5 of Gruen

Table 2
NFW Halo Parameters for Individual CLASH Clusters

Cluster	$M_{\rm 200c}$ ($10^{14}\,M_\odot\,h_{70}^{-1}$)	$c_{\rm 200c}$	r_{-2} (Mpc h_{70}^{-1})
X-ray Selected:			
Abell 383	7.98 ± 2.66	5.9 ± 1.8	0.31 ± 0.13
Abell 209	15.40 ± 3.42	2.7 ± 0.6	0.84 ± 0.22
Abell 2261	23.10 ± 5.22	3.7 ± 0.9	0.69 ± 0.20
RX J2129.7+0005	6.14 ± 1.79	5.6 ± 1.6	0.30 ± 0.11
Abell 611	15.76 ± 4.49	3.9 ± 1.2	0.57 ± 0.21
MS2137-2353	13.56 ± 5.27	2.7 ± 1.3	0.80 ± 0.45
RX J2248.7-4431	18.78 ± 6.72	3.6 ± 1.4	0.66 ± 0.32
MACS J1115.9+0129	16.66 ± 3.85	3.0 ± 0.8	0.75 ± 0.23
MACS J1931.8-2635	15.28 ± 7.13	4.4 ± 1.9	0.51 ± 0.30
RX J1532.9+3021	5.98 ± 2.32	5.2 ± 2.8	0.29 ± 0.18
MACS J1720.3+3536	14.50 ± 4.30	4.1 ± 1.3	0.51 ± 0.20
MACS J0429.6-0253	9.76 ± 3.50	4.6 ± 1.7	0.40 ± 0.19
MACS J1206.2-0847	18.17 ± 4.23	3.7 ± 1.1	0.60 ± 0.21
MACS J0329.7-0211	8.65 ± 1.97	6.7 ± 1.6	0.26 ± 0.08
RX J1347.5-1145	34.25 ± 8.78	3.2 ± 0.9	0.85 ± 0.29
MACS J0744.9+3927	18.03 ± 4.96	3.5 ± 1.2	0.58 ± 0.23
High Magnification:			
MACS J0416.1-2403	10.74 ± 2.60	2.9 ± 0.7	0.65 ± 0.18
MACS J1149.5+2223	25.02 ± 5.53	2.1 ± 0.6	1.12 ± 0.35
MACS J0717.5+3745	26.77 ± 5.36	1.8 ± 0.4	1.31 ± 0.31
MACS J0647.7+7015	13.90 ± 4.20	4.1 ± 1.5	0.48 ± 0.21

Note. Cluster parameters derived from single spherical NFW fits to individual surface mass density profiles (Figure 11) reconstructed from combined strong-lensing, weak-lensing shear and magnification measurements. We adopt a concordance cosmology of $h=0.7$, $\Omega_{\rm m}=0.27$, and $\Omega_\Lambda=0.73$. The fitting radial range is restricted to $R\leqslant 2$ Mpc $h^{-1}\simeq 2.9$ Mpc h_{70}^{-1}.

Table 3
Mass Estimates for Individual CLASH Clusters

Cluster	M_{2500c} ($10^{14}\,M_\odot$)	M_{1000c} ($10^{14}\,M_\odot$)	M_{500c} ($10^{14}\,M_\odot$)	M_{vir}[a] ($10^{14}\,M_\odot$)	M_{100c} ($10^{14}\,M_\odot$)	M_{200m} ($10^{14}\,M_\odot$)	M (<1.5 Mpc) ($10^{14}\,M_\odot$)
X-ray Selected:							
Abell 383	2.78 ± 0.63	4.43 ± 1.16	5.88 ± 1.73	9.41 ± 3.33	9.66 ± 3.45	10.34 ± 3.78	6.95 ± 1.63
Abell 209	2.95 ± 0.68	6.18 ± 1.25	9.64 ± 1.97	19.60 ± 4.61	20.49 ± 4.88	22.36 ± 5.44	10.28 ± 1.37
Abell 2261	5.91 ± 1.03	10.85 ± 1.89	15.65 ± 3.05	28.21 ± 6.87	29.39 ± 7.26	31.41 ± 7.94	14.22 ± 1.79
RX J2129.7+0005	2.08 ± 0.44	3.35 ± 0.78	4.48 ± 1.16	7.21 ± 2.23	7.48 ± 2.34	7.87 ± 2.51	5.75 ± 1.23
Abell 611	4.13 ± 0.92	7.48 ± 1.67	10.73 ± 2.65	18.95 ± 5.77	19.99 ± 6.21	20.78 ± 6.54	11.24 ± 1.95
MS2137-2353	2.47 ± 0.72	5.21 ± 1.41	8.28 ± 2.57	16.98 ± 7.31	18.25 ± 8.12	18.91 ± 8.54	9.67 ± 2.12
RX J2248.7-4431	4.45 ± 1.05	8.42 ± 2.08	12.45 ± 3.62	22.54 ± 8.78	24.12 ± 9.68	24.53 ± 9.91	12.67 ± 2.50
MACS J1115.9+0129	3.50 ± 0.82	7.02 ± 1.43	10.67 ± 2.22	20.30 ± 4.97	21.88 ± 5.48	22.24 ± 5.60	11.55 ± 1.61
MACS J1931.8-2635	4.10 ± 1.12	7.36 ± 2.36	10.51 ± 4.05	18.02 ± 9.05	19.18 ± 9.88	19.44 ± 10.07	11.23 ± 3.07
RX J1532.9+3021	1.83 ± 1.01	3.03 ± 1.38	4.17 ± 1.71	7.04 ± 2.79	7.51 ± 3.02	7.58 ± 3.06	5.81 ± 1.63
MACS J1720.3+3536	3.92 ± 0.86	7.00 ± 1.59	9.96 ± 2.53	17.04 ± 5.39	18.29 ± 5.94	18.30 ± 5.94	11.02 ± 2.05
MACS J0429.6-0253	2.85 ± 0.70	4.92 ± 1.32	6.85 ± 2.10	11.35 ± 4.33	12.15 ± 4.76	12.13 ± 4.74	8.40 ± 2.03
MACS J1206.2-0847	4.62 ± 1.01	8.47 ± 1.63	12.24 ± 2.49	21.35 ± 5.29	23.18 ± 5.94	22.82 ± 5.81	12.98 ± 1.84
MACS J0329.7-0211	3.29 ± 0.64	5.02 ± 1.00	6.51 ± 1.37	9.72 ± 2.30	10.35 ± 2.50	10.21 ± 2.45	7.94 ± 1.36
RX J1347.5-1145	7.65 ± 1.63	14.91 ± 2.98	22.33 ± 4.89	40.66 ± 11.13	44.50 ± 12.60	43.59 ± 12.25	19.33 ± 2.61
MACS J0744.9+3927	4.32 ± 1.02	8.12 ± 1.76	11.94 ± 2.81	20.57 ± 5.98	23.21 ± 7.08	21.32 ± 6.29	13.96 ± 2.39
High Magnification:							
MACS J0416.1-2403	2.21 ± 0.53	4.48 ± 0.97	6.85 ± 1.52	12.99 ± 3.29	14.13 ± 3.66	14.12 ± 3.66	8.74 ± 1.37
MACS J1149.5+2223	3.73 ± 1.11	8.74 ± 1.98	14.57 ± 3.06	30.45 ± 7.06	34.72 ± 8.36	32.62 ± 7.71	15.31 ± 1.95
MACS J0717.5+3745	3.42 ± 0.87	8.61 ± 1.74	14.98 ± 2.85	32.97 ± 6.88	37.95 ± 8.17	35.46 ± 7.52	15.63 ± 1.75
MACS J0647.7+7015	3.72 ± 0.98	6.65 ± 1.65	9.49 ± 2.51	15.91 ± 5.07	17.59 ± 5.83	16.64 ± 5.40	11.37 ± 2.26

Notes. Cluster mass estimates $M_{3D}(<r)$ from single spherical NFW fits to individual surface mass density profiles (Figure 11). All quantities in the table are given in physical units assuming a concordance cosmology of $h = 0.7$, $\Omega_m = 0.27$, and $\Omega_\Lambda = 0.73$. See Table 2 for M_{200c}. The fitting radial range is restricted to $R \leqslant 2$ Mpc $h^{-1} \simeq 2.9$ Mpc h_{70}^{-1}.

[a] Virial overdensity Δ_{vir} based on the spherical collapse model (see Appendix A of Kitayama & Suto 1996). For our redshift range $0.187 \leqslant z \leqslant 0.686$, Δ_{vir} ranges approximately from $\simeq$110 to 140 with respect to the critical density of the universe at the cluster redshift.

et al. 2015), even though C^{int} is less important at larger cluster radii (Figure 1).

On the other hand, the stacked cluster measurements of Umetsu et al. (2014) empirically account for the cluster-to-cluster profile variations from bootstrap resampling of the cluster sample.

5. CLASH STACKED MASS PROFILE ANALYSIS

Stacking an ensemble of clusters helps average out the projection effects of halo asphericity and substructure, as well as the cosmic noise from projected uncorrelated LSS. The statistical precision can be improved by stacking a large number of clusters, allowing a tighter comparison of the averaged lensing signal with theoretical models (Okabe et al. 2010, 2013; Umetsu et al. 2011a, 2014; Miyatake et al. 2015).

Hereafter, our analysis will focus on the X-ray-selected subsample of 16 CLASH clusters, which comprises a population of high-mass X-ray regular clusters. The X-ray selection of this subsample is optimized for radial profile measurements (Postman et al. 2012). Numerical simulations suggest that the CLASH X-ray-selected subsample is prevalently composed of relaxed clusters (~70%) and largely free of orientation bias (Meneghetti et al. 2014).[20] The selection criteria based on X-ray morphology also ensure well-defined cluster centers (Section 3.1). The four high-magnification clusters are thus excluded from this part of the analysis (Sections 5 and 6).

5.1. Stacked Cluster Lensing Signal

With a given set of surface mass density profiles for individual clusters, we can stack them together to produce an ensemble-averaged radial profile. Following the prescription of Umetsu et al. (2011a), we re-evaluate the $\boldsymbol{\Sigma}$ profiles of individual clusters in physical (proper) length units, using the same radial grid for all clusters. Stacking an ensemble of clusters ($n = 1, 2, \ldots$) is expressed as (Umetsu et al. 2011a)

$$\langle\langle \boldsymbol{\Sigma} \rangle\rangle = \left(\sum_n \mathcal{W}_n \right)^{-1} \left(\sum_n \mathcal{W}_n \boldsymbol{\Sigma}_n \right), \tag{26}$$

where $\mathcal{W}_n$ is the sensitivity matrix of the nth cluster,

$$(\mathcal{W}_n)_{ij} \equiv \Sigma_{(c,\infty)n}^{-2} (C_n^{-1})_{ij}, \tag{27}$$

with $\Sigma_{(c,\infty),n}$ the far-background critical surface mass density and C_n the total covariance matrix (Equation (19)) for the nth cluster.[21] The error covariance matrix for the stacked $\langle\langle \Sigma \rangle\rangle$ profile is given by (Umetsu et al. 2011a)

$$\mathcal{C} = \left(\sum_n \mathcal{W}_n \right)^{-1}. \tag{28}$$

[20] Meneghetti et al. (2014) showed that, for this subsample, the median angle between the major axis of the halos and the X-ray-selected sight lines is ~57°, compared to ~54° expected for a distribution of random orientations.

[21] Since the covariance matrix C is defined for the far-background convergence $\kappa_{c,\infty}$, the associated critical surface mass density too is a far-background quantity, $\Sigma_{c,\infty} = \Sigma_c(z \to \infty)$.

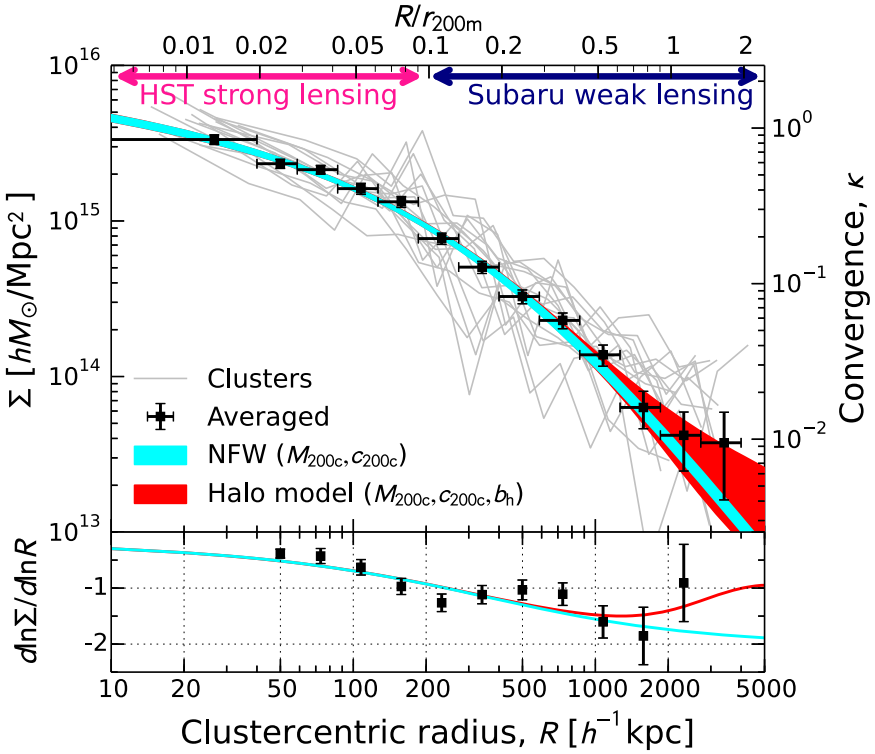

Figure 3. Upper panel: ensemble-averaged surface mass density $\langle\langle\Sigma\rangle\rangle$ (black squares) of the X-ray-selected subsample of 16 clusters, which is obtained by stacking individual Σ profiles (gray lines; Figure 11) derived from the joint analysis of *HST* and Subaru lensing data sets. The red-shaded area shows the 1σ confidence region of the three-parameter halo model fit (NFW+LSS (ii), Table 4). The projected NFW model (cyan-shaded area, 1σ) slightly underpredicts the total mass profile relative to the halo model at $R \gtrsim r_{200m}$. The scale on the right vertical axis indicates the corresponding lensing convergence scaled to the mean depth of weak-lensing observations. Lower panel: The logarithmic slope $d\ln\langle\langle\Sigma\rangle\rangle/d\ln R$ (black squares) is shown along with the two best-fit models in the upper panel.

The weight matrix $\mathcal{W}_n$ is mass-independent when stacking in physical length units (Okabe et al. 2010, 2013; Umetsu et al. 2011a, 2014), which makes the effective halo mass extracted from the averaged lensing signal a good proxy for the mean population value (see Section 5.4; Johnston et al. 2007; Okabe et al. 2013; Umetsu et al. 2014; Sereno et al. 2015c). On the other hand, stacking in length units scaled to r_Δ weights the contribution of each cluster to each radial bin in a nonlinear and model-dependent manner (Okabe et al. 2013), such that $\mathrm{tr}(\mathcal{W}) \propto r_\Delta^2 \propto M_\Delta^{2/3}$ when C is dominated by the statistical noise contribution $C^{\rm stat}$.

In Figure 3 we show the resulting $\langle\langle\boldsymbol{\Sigma}\rangle\rangle$ profile averaged in 13 radial bins. The innermost bin represents the mean density interior to $R_{\rm min} = 40\,{\rm kpc}\,h^{-1}$, which corresponds approximately to the typical resolution limit of our strong-lensing data ($\theta_{\rm min} = 10''$; Section 3.6.2 and Figure 11). Since $R_{\rm min}$ is much larger than the rms offset between the BCG and X-ray peak, $\sigma_{\rm off} \simeq 11\,{\rm kpc}\,h^{-1}$ (Section 3.1), the miscentering effects on the $\langle\langle\boldsymbol{\Sigma}\rangle\rangle$ profile are expected to be insignificant for the X-ray-selected subsample (Umetsu et al. 2014). The other bins are logarithmically spaced over the range $R = [R_{\rm min}, R_{\rm max}] = [40,4000]\,{\rm kpc}\,h^{-1}$ $(0.02 \lesssim R/r_{200m} \lesssim 2)$, spanning two decades in radius. For this sample, we find a sensitivity-weighted average redshift of $\langle\langle z_l\rangle\rangle \simeq 0.34$, in close agreement with the median redshift of $\overline{z}_l \simeq 0.35$. We detect the stacked lensing signal at a total S/N of $\simeq$33 using the total covariance matrix $\mathcal{C}$ including the statistical, systematic, projected uncorrelated LSS, and intrinsic-variance contributions (Section 3.6.3).

5.2. Modeling the Stacked Lensing Signal

We quantify and characterize the ensemble-averaged mass distribution of our X-ray-selected subsample using the $\langle\langle\Sigma\rangle\rangle$ profile (Section 5.1). To interpret the observed averaged lensing signal, we consider the line of sight projected surface mass density around the cluster center, $\Sigma(R) = \int dl\ \Delta\rho(r)$, with $\Delta\rho(r) = \rho(r) - \overline{\rho}_{\rm m}$ the mass overdensity. In the regime where $R \lesssim r_{200m}$, $\Sigma(R)$ is dominated by the cluster halo contribution $\rho_{\rm h}(r)$, so that $\Sigma(R) \simeq 2\int_0^\infty dl\ \rho_{\rm h}(r)$.

As shown in Figure 3, our weak- and strong-lensing data together cover a wide range of clustercentric distances R, extending out to $R_{\rm max} = 4000\,{\rm kpc}\,h^{-1} \approx 2r_{200m}$. In the context of the ΛCDM model, the two outermost radial bins lie in the transition between the one-halo and two-halo regimes (Cooray & Sheth 2002), $r_{200m} \lesssim R \lesssim 2R_{200m}$, where the large-scale two-halo contribution to $\Sigma(R)$ is expected to become important (Oguri & Hamana 2011; Beraldo e Silva et al. 2013; Umetsu et al. 2014).[22] In this work, we thus test models both with and without including the two-halo term.

5.2.1. Halo Density Profiles

We give here a brief description of the halo profile models that we consider. For each model $\rho_{\rm h}(r)$, the halo mass is defined using a spherical overdensity $\Delta_{\rm c} = 200$ as M_{200c}. We introduce the radius r_{-2} at which the logarithmic density slope is *isothermal*, that is, $d\ln\rho_{\rm h}(r)/d\ln r = -2$ at $r = r_{-2}$. In

[22] On the other hand, the tangential shear $\gamma_+ = \Delta\Sigma/\Sigma_{\rm c}$ is insensitive to the projected two-halo term in the transition regime (Oguri & Hamana 2011).

analogy to the NFW concentration parameter, the degree of concentration is defined by $c_{200c} = r_{200c}/r_{-2}$. We use M_{200c} and c_{200c} as fitting parameters, when possible.

1. Generalized NFW (gNFW) model (Zhao 1996):

$$\rho_h(r) = \frac{\rho_s}{(r/r_s)^{\gamma_c}(1 + r/r_s)^{3-\gamma_c}}, \quad r_{-2} = (2 - \gamma_c) r_s, \tag{29}$$

with γ_c the central slope, ρ_s and r_s the characteristic density and radius, respectively. For $\gamma_c = 1$, this reduces to the standard NFW model $\rho_{NFW}(r)$ with $r_s = r_{-2}$.

2. Einasto model (Einasto 1965):

$$\rho_h(r) = \rho_{-2} \exp\left\{-\frac{2}{\alpha_E}\left[\left(\frac{r}{r_{-2}}\right)^{\alpha_E} - 1\right]\right\}, \tag{30}$$

with α_E the shape parameter describing the degree of curvature and $\rho_{-2} = \rho_h(r_{-2})$. An Einasto profile with $\alpha_E \approx 0.18$ closely resembles the NFW profile over roughly two decades in radius (Ludlow et al. 2013).

3. DARKexp-γ model. DARKexp is a theoretically derived model for collisionless self-gravitating systems with isotropic velocity distributions (Hjorth & Williams 2010; Williams & Hjorth 2010). We use Dehnen–Tremaine γ-models (Dehnen 1993; Tremaine et al. 1994) as an analytic fitting function for the DARKexp density profile (Hjorth et al. 2015):

$$\rho_h(r) = \frac{\rho_s}{(r/r_s)^{\gamma_c}(1 + r/r_s)^{4-\gamma_c}}, \quad r_{-2} = (1 - \gamma_c/2) r_s, \quad \gamma_c \approx 3\log_{10}\phi_0 - 0.65 \quad (1.7 \leqslant \phi_0 \leqslant 6), \tag{31}$$

where ρ_s and r_s are the scale density and radius, respectively, and ϕ_0 represents the dimensionless depth of the halo potential describing the profile shape. The γ models approximate DARKexp very well over nearly four decades in radius (Hjorth et al. 2015).[23]

4. Pseudo-isothermal (PI) sphere model:

$$\rho_h(r) = \frac{\rho_c}{1 + (r/r_c)^2} \tag{32}$$

with ρ_c and r_c the core density and radius, respectively. The corresponding asymptotically flat circular velocity is $V_c = (4\pi G \rho_c r_c^2)^{1/2}$ (Shao et al. 2013).

5. Burkert model (Mori & Burkert 2000):

$$\rho_h(r) = \frac{\rho_0}{(1 + r/r_0)(1 + r^2/r_0^2)} \tag{33}$$

with ρ_0 and r_0 the core density and radius, respectively.

6. Power-law sphere model:

$$\rho_h(r) \propto r^{-\gamma_c}. \tag{34}$$

This model includes the singular isothermal sphere model with $\gamma_c = 2$.

The NFW, gNFW, and Einasto density profiles represent a family of phenomenological models for cuspy DM halos motivated by numerical simulations and observations. The DARKexp model describes the distribution of particle energies in finite, self-gravitating, collisionless, isotropic systems, providing theoretical predictions for the structure of collisionless DM halos. For radii accessible to N-body simulations, DARKexp allows for central slope values in the range $-2 \lesssim d\ln\rho_h/d\ln r \lesssim 0$. The empirical PI and Burkert models describe cored density profiles. The power-law model is often adopted as a lens model for its simplicity (e.g., Koopmans et al. 2009; Agnello et al. 2013).

[23] The DARKexp density profile is also well approximated by an Einasto profile at small halo radii (Hjorth et al. 2015).

5.2.2. Projected Halo Model

To interpret the averaged lensing signal in the context of the standard ΛCDM model, we employ as our reference model the halo model prescription of Oguri & Takada (2011). Specifically, we take into account the large-scale clustering contribution $\rho_{2h}(r)$ as

$$\Delta\rho(r) = f_t(r)\,\rho_h(r) + \rho_{2h}(r), \quad f_t(r) = \left[1 + \left(\frac{r}{r_t}\right)^2\right]^{-2}, \tag{35}$$

where $f_t(r)$ describes the steepening of the density profile around a truncation radius r_t (Baltz et al. 2009; Diemer & Kravtsov 2014). We fix the truncation parameter $\tau_{200c} \equiv r_t/r_{200c} = 3$ (Covone et al. 2014; Umetsu et al. 2014; Sereno et al. 2015c), which is a typical value for cluster-sized halos in ΛCDM cosmology (Oguri & Hamana 2011). When the two-halo term is neglected, the standard NFW halo model (Oguri & Hamana 2011) reduces to the Baltz–Marshall–Oguri (BMO) model that describes a truncated NFW profile, $f_t(r)\rho_{NFW}(r)$ (Baltz et al. 2009). For an ensemble of clusters with mass M and redshift z, the two-halo term is expressed as $\rho_{2h}(r) = \overline{\rho}_m b_h(M)\xi_m^L(r)$ with $\overline{\rho}_m$ the mean background density of the universe, $b_h(M)$ the linear halo bias, and $\xi_m^L(r)$ the linear matter correlation function, all evaluated at $z = \langle\langle z_l \rangle\rangle \simeq 0.34$ in the *WMAP* seven-year cosmology (Section 3.6.3). The two-halo term is proportional to the product $b_h\sigma_8^2$, where σ_8 is the rms amplitude of linear mass fluctuations in a sphere of comoving radius $8\,\mathrm{Mpc}\,h^{-1}$. In the adopted cosmology, $\sigma_8 = 0.81$ (Komatsu et al. 2011). We compute the total surface mass density $\Sigma(R)$ by projecting $\Delta\rho(r) = f_t\rho_{1h} + \rho_{2h}$ along the line of sight (Section 2.2 of Oguri & Hamana 2011). To evaluate the halo bias factor $b_h(M)$, we adopt the model of Tinker et al. (2010), which is well calibrated using a large set of N-body simulations. We use their fitting formula with a halo mass definition of $\Delta_c = 200$ (Umetsu et al. 2014), corresponding to $\Delta_m \simeq 420$ in our adopted cosmology.

5.3. Model Comparison with Observations

We constrain model parameters using the $\langle\langle\Sigma\rangle\rangle$ profile and its total covariance matrix $\mathcal{C}$ (Section 5.1). The χ^2 minimization is performed using the MINUIT minimization package from the CERN program libraries. The best-fit parameters are reported in Table 4, along with the reduced χ^2 and corresponding probability to exceed (PTE, hereafter) values.

We first consider halo density profile models without including the two-halo term. In this modeling approach, no truncation is applied when calculating the surface mass density

Table 4
Best-fit Models for the Stacked Mass Profile of the CLASH X-Ray-selected Subsample

Model	M_{200c} ($10^{14}\,M_\odot\,h_{70}^{-1}$)	c_{200c}	Shape/Structural Parameters	b_h	χ^2/dof	PTE[a]	Notes
NFW	$14.4^{+1.1}_{-1.0}$	$3.76^{+0.29}_{-0.27}$	$\gamma_c = 1$	⋯	11.3/11	0.419	No truncation
gNFW	$14.1^{+1.1}_{-1.1}$	$4.04^{+0.53}_{-0.52}$	$\gamma_c = 0.85^{+0.22}_{-0.31}$	⋯	10.9/10	0.366	No truncation
Einasto	$14.7^{+1.1}_{-1.1}$	$3.53^{+0.36}_{-0.39}$	$\alpha_E = 0.232^{+0.042}_{-0.038}$	⋯	11.7/10	0.306	No truncation
DARKexp-γ[b]	$14.5^{+1.2}_{-1.1}$	$3.53^{+0.42}_{-0.42}$	$\phi_0 = 3.90^{+0.41}_{-0.45}$	⋯	13.5/10	0.198	No truncation
Pseudo isothermal	⋯	⋯	$V_c = 1762^{+40}_{-39}$ km s^{-1}, $r_c = 69^{+7}_{-7}$ kpc	⋯	23.6/11	0.015	No truncation
Burkert	$11.6^{+0.8}_{-0.8}$	⋯	$r_{200c}/r_0 = 8.81^{+0.42}_{-0.41}$	⋯	29.9/11	0.002	No truncation
Power-law sphere	$12.5^{+0.8}_{-0.8}$	⋯	$\gamma_c = 1.78^{+0.02}_{-0.02}$	⋯	93.5/11	0.000	No truncation
Halo Model[c]:							
NFW+LSS (i)	$14.1^{+1.0}_{-1.0}$	$3.79^{+0.30}_{-0.28}$	$\gamma_c = 1$	9.3	10.9/11	0.450	ΛCDM $b_h(M)$ scaling
NFW+LSS (ii)	$14.4^{+1.4}_{-1.3}$	$3.74^{+0.33}_{-0.30}$	$\gamma_c = 1$	$7.4^{+4.6}_{-4.7}$	10.8/10	0.377	b_h as a free parameter
Einasto+LSS (i)	$14.3^{+1.1}_{-1.1}$	$3.69^{+0.36}_{-0.42}$	$\alpha_E = 0.248^{+0.051}_{-0.047}$	9.3	10.7/10	0.385	ΛCDM $b_h(M)$ scaling
Einasto+LSS (ii)	$14.5^{+1.9}_{-1.6}$	$3.65^{+0.47}_{-0.61}$	$\alpha_E = 0.245^{+0.061}_{-0.053}$	$8.7^{+5.3}_{-5.6}$	10.6/9	0.301	b_h as a free parameter
DARKexp+LSS (i)	$14.2^{+1.2}_{-1.1}$	$3.64^{+0.44}_{-0.46}$	$\phi_0 = 3.89^{+0.51}_{-0.54}$	9.3	11.7/10	0.308	ΛCDM $b_h(M)$ scaling
DARKexp+LSS (ii)	$14.0^{+1.8}_{-1.6}$	$3.69^{+0.53}_{-0.57}$	$\phi_0 = 3.85^{+0.57}_{-0.61}$	$10.1^{+4.9}_{-5.1}$	11.6/9	0.235	b_h as a free parameter

Notes.
[a] Probability to exceed the observed χ^2 value.
[b] We use Dehnen–Tremaine γ-models with the central cusp slope $\gamma_c = 3\log_{10}\phi_0 - 0.65$ ($1.7 \leqslant \phi_0 \leqslant 6$) as an analytic fitting function for the DARKexp density profile.
[c] For halo model predictions, we decompose the total mass overdensity $\Delta\rho(r) = \rho(r) - \overline{\rho}_m$ as $\Delta\rho = f_t\rho_h + \rho_{2h}$ where $\rho_h(r)$ is the halo density profile, $\rho_{2h}(r) = \overline{\rho}_m b_h \xi_m^L(r)$ is the two-halo term, and $f_t(r) = (1 + r^2/r_t^2)^{-2}$ describes the steepening of the density profile in the transition regime around the truncation radius r_t, which is assumed to be $r_t = 3r_{200c}$.

$\Sigma(R)$, effectively accounting for the large-scale contribution. Figure 4 shows the best-fit model profiles along with the observed $\langle\langle\Sigma\rangle\rangle$ profile. We find that two- or three-parameter cuspy models, namely, the NFW, gNFW, Einasto, and DARKexp-γ models, provide satisfactory fits (PTE > 0.05) to the data. The best-fit gNFW model has a central cusp slope of $\gamma_c = 0.85^{+0.22}_{-0.31}$, being consistent with the NFW model ($\gamma_c = 1$). The cored PI and Burkert models provide poor fits with χ^2/dof (PTE) values of 23.6/11 (1.5×10^{-2}) and 29.9/11 (1.7×10^{-3}), respectively. The power-law sphere model has a reduced χ^2 value of $\chi^2/\mathrm{dof} = 93.5/11$ and is strongly disfavored by the $\langle\langle\Sigma\rangle\rangle$ profile having a pronounced radial curvature.

Now we examine projected halo models following the prescription described in Section 5.2.2. In what follows, we will focus on our best models, specifically, the NFW, Einasto, and DARKexp-γ cuspy density profiles. We note that since the halo bias is given as a function of M_{200c}, the number of free parameters is unchanged for each case. We find these models (NFW+LSS (i), Einasto+LSS (i), and DARKexp+LSS (i) in Table 4) give statistically comparable fits. In all cases, including the two-halo term improves the fits, while keeping the best-fit parameters essentially unchanged (the difference in each parameter is much less than the 1σ uncertainty). Independent of the chosen profile, we find $b_h(M_{200c}) \sim 9.3$ ($b_h\sigma_8^2 \sim 6.1$) for our best-fit models.

On the basis of the goodness-of-fit statistic, the highest-ranked model among those considered is the NFW halo model (NFW +LSS (i); see the red curve in Figure 4) with $M_{200c} = 14.1^{+1.0}_{-1.0} \times 10^{14}\,M_\odot\,h_{70}^{-1}$ and $c_{200c} = 3.79^{+0.30}_{-0.28}$, followed by the Einasto and DARKexp halo models (Einasto+LSS (i) and DARKexp+LSS (i)). The best-fit NFW halo model yields an Einstein radius of $\theta_{Ein} = 14.0^{+3.4}_{-3.2}$ arcsec at $z_s = 2$, which is about 1.7σ lower than the median effective Einstein radius (see Section 3.5) of $\overline{\theta}_{Ein} = 20.''1$ observed for the X-ray-selected subsample (Section 3.5). The best-fit NFW parameters of our projected halo model are in good agreement with those from the stacked shear-only analysis of Umetsu et al. (2014), $M_{200c} = 13.4^{+1.0}_{-0.9} \times 10^{14}\,M_\odot\,h^{-1}$ and $c_{200c} = 4.01^{+0.35}_{-0.32}$, in

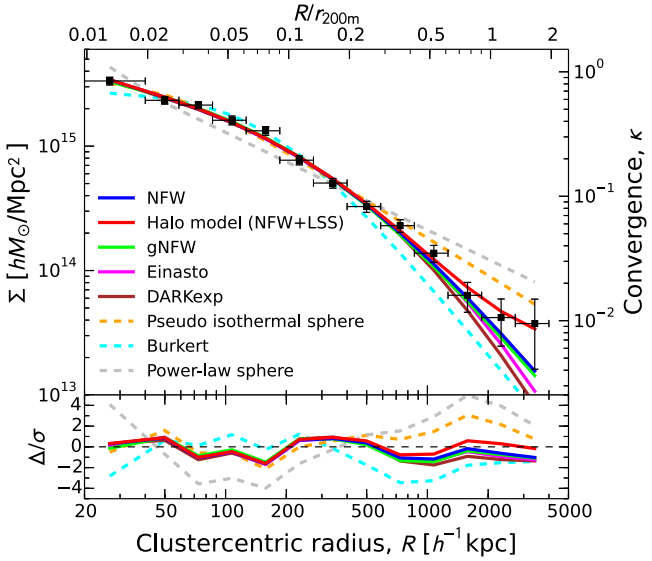

Figure 4. Upper panel: Comparison of models to the ensemble-averaged surface mass density $\langle\langle\Sigma\rangle\rangle$ (black squares) obtained for the X-ray-selected subsample of 16 clusters. Models with PTE > 0.05 are shown with solid lines, while those with PTE < 0.05 are shown with dashed lines (see Table 4). The red solid curve shows the best-fit two-parameter halo model (NFW+LSS (i), Table 4), including the effects of surrounding LSS as a two-halo term assuming the halo bias function of Tinker et al. (2010) in the *WMAP* seven-year cosmology. The lower panel shows the deviations Δ (in units of σ) of the best-fit profiles with respect to the observed $\langle\langle\Sigma\rangle\rangle$ profile.

which the two-halo term can be safely neglected as the stacked tangential-shear signal, $\langle\langle \Delta\Sigma \rangle\rangle$, is only sensitive to the intra-halo mass distribution in our radial range. The Einasto shape parameter is constrained to be $\alpha_{\rm E} = 0.248^{+0.051}_{-0.047}$ from an Einasto halo-model fit to the $\langle\langle \Sigma \rangle\rangle$ profile (Einasto+LSS (i)), in agreement with $\alpha_{\rm E} = 0.191^{+0.071}_{-0.068}$ from the stacked shear-only analysis of Umetsu et al. (2014). Our measurements agree well with predictions from ΛCDM numerical simulations, $\alpha_{\rm E}$= 0.21 ± 0.07 (Meneghetti et al. 2014, $\alpha_{\rm E} = 0.24 \pm 0.09$ when fitted to surface mass density profiles). The fitting formula given by Gao et al. (2008) yields $\alpha_{\rm E} \simeq 0.29$ for our X-ray-selected subsample. This is consistent with our results at the 1σ level.

The halo-model interpretation we have adopted is a crude approximation in the transition between the intra-halo and two-halo regimes, neglecting nonlinear effects (Baldauf et al. 2010; Diemer & Kravtsov 2014). In order to effectively account for possible modifications due to nonlinear effects, here we allow the halo bias factor $b_{\rm h}$ to be a free parameter. We find that allowing $b_{\rm h}$ to be free does not improve the fits and that the resulting best-fit parameters remain unchanged within the errors (Table 4). The *effective* halo bias $b_{\rm h}$ is detected at 1.6σ–2.0σ significance, where the exact level of significance depends on the details of the halo density profile in the transition regime. In Figure 3, we compare the resulting NFW halo model profile (NFW+LSS (ii), red shaded area) and the NFW profile (cyan-shaded area) along with the $\langle\langle \Sigma \rangle\rangle$ profile.

5.4. Interpreting the Effective Halo Mass

Interpreting the effective mass from stacked lensing requires caution when the cluster sample spans a broad range of masses and redshifts (Mandelbaum et al. 2005; Niikura et al. 2015). If there is a significant scatter in the luminosity–mass relation of halos, then the halo mass distribution of a luminosity-selected sample becomes significantly broader, with the width and asymmetry of the distribution typically increasing for higher luminosity bins. Accordingly, there is no typical mass, and in general the effective mass determination from NFW fits falls between the mean and the median masses of the halo population (Mandelbaum et al. 2005). Alternatively, if a halo sample has a broad redshift distribution, the effective lensing mass determined from stacking with redshift-dependent weights (Equation (27)) is generally different from the mean population mass (Umetsu et al. 2014).

To assess this possibility, we compare the stacked lensing results with the individual cluster masses (Tables 2 and 3). For the former, we consider our best model (NFW+LSS (i) in Table 4) for the X-ray-selected subsample, namely the NFW halo model using the $b_{\rm h}$–M relation of Tinker et al. (2010).

Following Umetsu et al. (2014), we construct a composite-halo mass profile $\langle\langle M_\Delta \rangle\rangle$ (see also Coupon et al. 2013; Ford et al. 2014) from a sensitivity-weighted average of NFW fits to individual cluster $\boldsymbol{\Sigma}$ profiles as

$$\langle\langle M_\Delta \rangle\rangle = \frac{\sum_n {\rm tr}(\mathcal{W}_n) M_{\Delta,n}}{\sum_n {\rm tr}(\mathcal{W}_n)} \tag{36}$$

using ${\rm tr}(\mathcal{W}_n) \propto \Sigma^{-2}_{({\rm c},\infty)n}$ (Equation (27)) as an effective sensitivity weight for each cluster. Hence, the weight depends on cluster redshift $z_{\rm l}$ through $\Sigma_{({\rm c},\infty)}$. The error variance for $\langle\langle M_\Delta \rangle\rangle$ is given by $\sigma^2_\Delta = \left[\sum_n {\rm tr}(\mathcal{W}_n)\right]^{-2} \sum_n \sigma^2_{\Delta,n} [{\rm tr}(\mathcal{W}_n)]^2$ with $\sigma_{\Delta,n}$ the 1σ uncertainty for $M_{\Delta,n}$. It was shown by Umetsu et al. (2014) that this composite-halo approach using the trace approximation for the sensitivity matrix can give an adequate description of the observed stacked lensing signal.

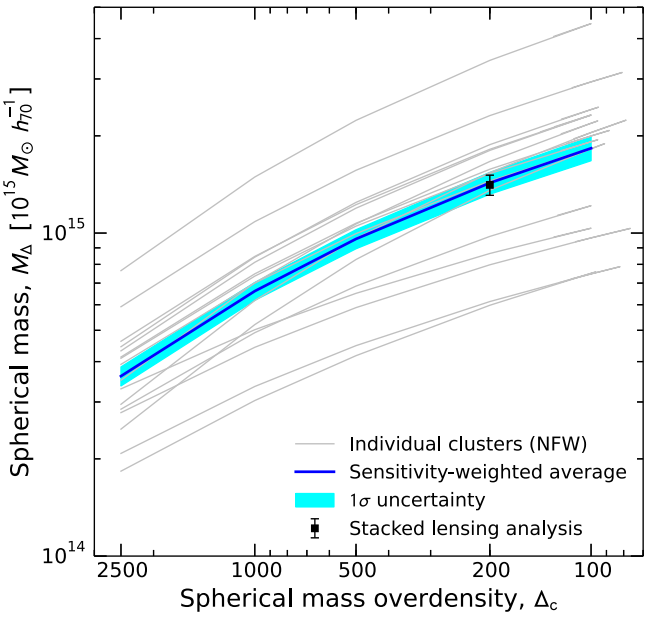

Figure 5. Cumulative mass profiles $M_\Delta = M_{\rm 3D}(<r_\Delta)$ for the X-ray-selected subsample of 16 clusters, shown at several characteristic values of the spherical mass overdensity $\Delta_{\rm c} = \rho_{\rm h}(<r)/\rho_{\rm c}$. The gray lines show the M_Δ profiles for individual clusters obtained from NFW fits to their Σ profiles (Tables 2 and 3; Figure 11). The blue line and the cyan-shaded area show the mean and its 1σ error of the composite-halo profile $\langle\langle M_\Delta \rangle\rangle$ from a sensitivity-weighted average of the individual M_Δ profiles. The filled square at $\Delta_{\rm c} = 200$ marks the best-fit halo mass $M_{200{\rm c}} = 14.1^{+1.0}_{-1.0} \times 10^{14}\, M_\odot\, h_{70}^{-1}$ obtained from a halo-model fit (NFW+LSS (i) in Table 4) to the stacked $\langle\langle \Sigma \rangle\rangle$ profile (Figure 4). This is in excellent agreement with the mean sample mass $\langle\langle M_{200{\rm c}} \rangle\rangle = (14.3 \pm 1.1) \times 10^{14}\, M_\odot\, h_{70}^{-1}$ averaged using ${\rm tr}(\mathcal{W})$ (Equation (27)) as weights.

The results of this comparison are summarized in Figure 5. At $\Delta_{\rm c} = 200$, we find a sensitivity-weighted average of $\langle\langle M_{200{\rm c}} \rangle\rangle = (14.3 \pm 1.1) \times 10^{14}\, M_\odot\, h_{70}^{-1}$ for the X-ray-selected subsample, in excellent agreement with the best-fit halo mass of $M_{200{\rm c}} = 14.1^{+1.0}_{-1.0} \times 10^{14}\, M_\odot\, h_{70}^{-1}$ extracted from a halo-model fit to the $\langle\langle \Sigma \rangle\rangle$ profile. On the other hand, the unweighted median masses of the clusters are ∼3%–8% higher than the sensitivity-weighted masses $\langle\langle M_\Delta \rangle\rangle$ at each overdensity. This difference is not due to the asymmetry of the distribution of the cluster masses because the unweighted median and mean masses agree to within ∼2% at each overdensity. Our results appear to be robust against different ensemble-averaging techniques once the effects of sensitivity weighting are consistently taken into account, supporting the findings of Umetsu et al. (2014).

6. CLASH CONCENTRATION–MASS RELATION

6.1. Bayesian Linear Regression

We examine the relationship between halo mass and concentration for our CLASH X-ray-selected subsample. Here we closely follow the Bayesian regression approach of Sereno et al. (2015b), taking into account the correlation between the errors on mass and concentration (e.g., Du & Fan 2014) and the effects of nonuniformity of the mass probability distribution (e.g., Kelly 2007; Andreon & Bergé 2012). We consider a

power-law function of the following form:

$$c_{200c} = 10^{\alpha}\left(\frac{M_{200c}}{M_{piv}}\right)^{\beta}\left(\frac{1+z}{1+z_{piv}}\right)^{\gamma}, \quad (37)$$

with M_{piv} and z_{piv} the pivot mass and redshift, respectively. We set $M_{piv} = 10^{15}\,M_{\odot}h^{-1}$ and $z_{piv} = 0.34$, approximately the effective mean values of the cluster mass and redshift, respectively (Section 5). In the present analysis, we fix $\gamma = -0.668$ (Meneghetti et al. 2014) as predicted for the CLASH X-ray-selected population (for details, see Section 6.2) because our data do not have sufficient statistics to constrain the redshift evolution of the c–M relation (Merten et al. 2015).

To perform regression analysis we define new dependent and independent variables in logarithmic form as

$$Y \equiv \log_{10}\left[\left(\frac{1+z}{1+z_{piv}}\right)^{-\gamma} c_{200c}\right],$$
$$X \equiv \log_{10}(M_{200c}/M_{piv}). \quad (38)$$

Equation (37) is then expressed by a linear relation, $Y = \alpha + \beta X$. The observed values of latent variables are denoted with lowercase letters. If the selected clusters in our sample are not uniformly distributed in logarithmic mass X, this can lead to biased estimates of regression parameters (Kelly 2007; Sereno et al. 2015b). We properly account for these effects in Bayesian regression (Kelly 2007; Sereno et al. 2015a, 2015b; Sereno & Ettori 2015a).

The clusters in our X-ray-selected subsample are selected to be X-ray hot (>5 keV) and regular in X-ray morphology (Postman et al. 2012). In general, if we select a cluster sample by imposing certain thresholds on cluster observables, then the steepening at the high end of the intrinsic mass function, combined with the selection effects, makes the resulting mass probability distribution of selected clusters approximately lognormal (Appendix A of Sereno & Ettori 2015a).

In this study, we model the intrinsic probability distribution $\mathcal{P}(X)$ of logarithmic mass X with a single Gaussian function characterized by two parameters, namely the mean μ and the dispersion τ (Kelly 2007). This approach alleviates the problem of assuming a uniform prior distribution on the independent variable X and, in general, provides a good approximation for a regular unimodal distribution (Kelly 2007; Andreon & Bergé 2012; Sereno & Ettori 2015a). A uniform prior distribution can be recovered in the limit of $\tau \to \infty$.

The conditional probability distribution $\mathcal{P}(\boldsymbol{y}|\boldsymbol{x}) = \prod_n \mathcal{P}(y_n|x_n)$ of $\boldsymbol{y} = \{y_n\}$ given $\boldsymbol{x} = \{x_n\}$ is then written as (Kelly 2007)

$$\ln \mathcal{P}(\boldsymbol{y}|\boldsymbol{x}) = -\frac{1}{2}\sum_n\left[\ln(2\pi\sigma_n^2) + \left(\frac{y_n - \langle y_n|x_n\rangle}{\sigma_n}\right)^2\right], \quad (39)$$

where $\langle y_n|x_n\rangle$ and $\sigma_n^2 \equiv \mathrm{Var}(y_n|x_n)$ are the conditional mean and variance of y_n given x_n, respectively:

$$\langle y_n|x_n\rangle = \alpha + \beta\mu + \frac{\beta\tau^2 + C_{xy,n}}{\tau^2 + C_{xx,n}}(x_n - \mu),$$
$$\sigma_n^2 = \beta^2\tau^2 + \sigma_{Y|X}^2 + C_{yy,n} - \frac{(\beta\tau^2 + C_{xy,n})^2}{\tau^2 + C_{xx,n}}, \quad (40)$$

where $\sigma_{Y|X}$ is the intrinsic scatter in the Y–X relation; $C_{xx,n}$, $C_{yy,n}$, and $C_{xy,n} = C_{yx,n}$ are the elements of the covariance matrix between the observables x_n and y_n of the nth cluster. If $\mathcal{P}(X_n)$ is assumed to be uniform, we have $\langle y_n|x_n\rangle = \alpha + \beta x_n$ and $\sigma_n^2 = \sigma_{Y|X}^2 + C_{yy,n} + \beta^2 C_{xx,n} - 2\beta C_{xy,n}$ (e.g., Kelly 2007; Okabe & Smith 2015).

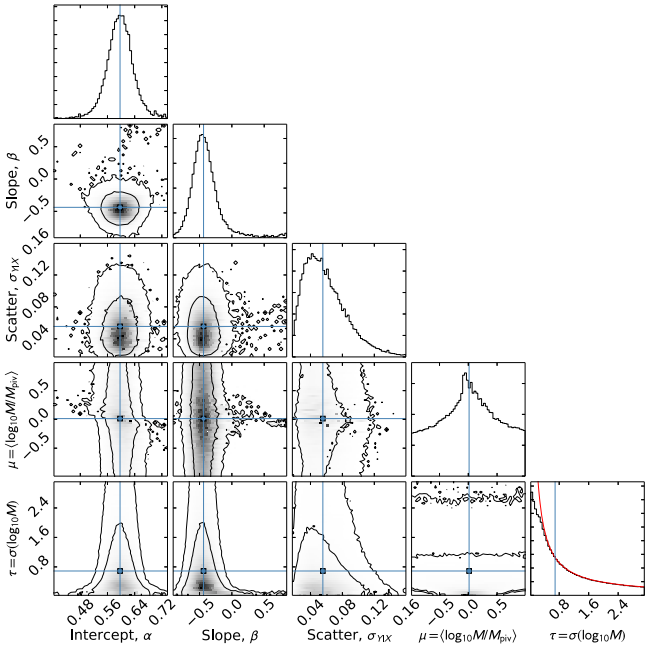

Figure 6. Constraints on the regression parameters (α, β, $\sigma_{Y|X}$, μ, τ) of the c–M relation (Section 6.1) obtained from *HST* and Subaru lensing observations of 16 CLASH X-ray-selected clusters, showing marginalized one-dimensional distributions and two-dimensional 68% and 95% limits. For each parameter, the blue solid line shows the biweight central location (C_{BI}) of the marginalized one-dimensional posterior distribution. For the τ parameter, the prior probability distribution function is shown by the red line.

We use uninformative priors for all parameters. We adopt uniform priors for the intercept α, the slope β, and the mean μ. For the variance parameters $\sigma_{Y|X}^2$ and τ^2, we use the inverse Gamma distribution, $\Pi\Gamma(\epsilon, \epsilon)$, with $\epsilon \ll 1$ a small number (Andreon & Hurn 2010; Sereno & Ettori 2015a, 2015b). In our analysis, we choose $\epsilon = 10^{-3}$ (Sereno & Ettori 2015a, 2015b).

Figure 6 shows the two-dimensional marginalized posterior distributions derived for all pairs of the regression parameters (α, β, $\sigma_{Y|X}$, μ, τ). The marginalized constraints ($C_{BI} \pm S_{BI}$; Section 4.2) on the intercept, slope, and intrinsic scatter are $\alpha = 0.60 \pm 0.04$, $\beta = -0.44 \pm 0.19$, and $\sigma_{Y|X} = 0.056 \pm 0.026$ (or, a natural logarithmic scatter of 0.13 ± 0.06). The posterior distributions show a long tail extending toward positive values of β, corresponding to shallower slopes for the c–M relation. This tail is associated with small values of the τ parameter that describes the width of the mass probability distribution $\mathcal{P}(X)$. Hence, accounting for the nonuniformity of the mass probability distribution is crucial for making inference of the underlying c–M relation for the CLASH sample. We have checked that the tail in the posterior distribution of β disappears if $\mathcal{P}(X)$ is assumed to be uniform. We see from Figure 6 that the constraint on the τ parameter is dominated by the prior especially at $\tau \gtrsim 0.5$ and that the data are not informative enough to determine the dispersion of the intrinsic mass distribution.

6.2. Comparison with Predictions for the CLASH Survey

In Figure 7, we summarize in the c–M plane our regression results obtained for our 16 CLASH X-ray-selected clusters. A

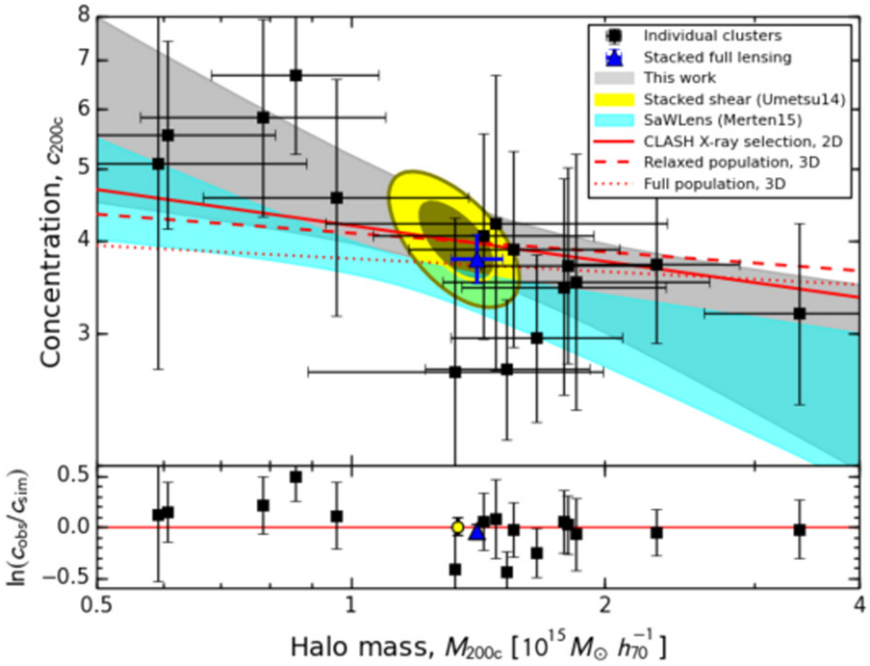

Figure 7. Upper panel: concentration–mass relation for the CLASH X-ray-selected subsample of 16 clusters derived from a joint analysis of *HST* and Subaru lensing data sets. The black squares with error bars represent the measured parameters and their 1σ uncertainties for individual clusters. The gray shaded region shows the 1σ confidence region of the CLASH c–M relation ($z = 0.34$) from our Bayesian regression. The blue triangle shows the best-fit parameters from a halo-model fit (NFW +LSS (i) in Table 4) to the ensemble-averaged surface mass density profile, $\langle\langle\boldsymbol{\Sigma}\rangle\rangle$ (Figure 4). The yellow contours represent the 1σ and 2σ confidence regions determined from the stacked shear-only analysis of the same sample (Umetsu et al. 2014). The cyan-shaded band shows the 1σ uncertainty on the CLASH c–M relation obtained by Merten et al. (2015). The red-solid line represents the theoretical expectation from numerical simulations accounting for the projection effects and the CLASH selection function based on X-ray morphology (Meneghetti et al. 2014). The red-dashed and red-dotted lines show the intrinsic three-dimensional c–M relations for the relaxed and full populations, respectively (Meneghetti et al. 2014). The lower panel shows, for each case, the ratio between the measured concentration and the predicted value using the $c(M, z)$ relation for the CLASH X-ray-selected population (red-solid line in the upper panel).

detailed comparison with the SaWLens results (Merten et al. 2015) is presented in Section 7.4.2.

Understanding the selection function and observational biases arising from projection effects is crucial when interpreting the c–M relation derived from lensing observations. For the CLASH sample, this has been addressed in detail by Meneghetti et al. (2014) using a sample of ~1400 cluster-sized halos ($0.25 \leqslant z \leqslant 0.67$) selected from the MUSIC-2 nonradiative hydrodynamical N-body simulations (Sembolini et al. 2013) in a ΛCDM universe ($h = 0.7$, $\Omega_{\rm m}$= 0.27, $\Omega_\Lambda = 1 - \Omega_{\rm m}$, $\sigma_8 = 0.82$).

Meneghetti et al. (2014) characterized a sample of halos that follows the CLASH selection function based on X-ray morphological regularity. Their results suggest that the CLASH X-ray-selected subsample is prevalently composed of relaxed clusters (~70%) and largely free of orientation bias (Section 5). Another important implication is that this subsample is expected to have a very small scatter in concentration because of the high degree of regularity in their X-ray morphology.

Meneghetti et al. (2014) find that the mean two-dimensional concentration of the CLASH X-ray-selected sample is expected to be ~11% higher than that for the full population of clusters (Meneghetti et al. 2014). According to their simulations, we expect that the NFW concentrations of this sample determined from noise-free Σ profiles are in the range $3 \lesssim c_{200c} \lesssim 6$, with a mean (median) value of 3.87 (3.76) and a standard deviation of 0.61. The distribution follows a power-law relation of the form $c \propto M^{-0.160\pm0.108} \times (1+z)^{-0.668\pm0.341}$ with a normalization of $c|_{z=0.34} = 3.96 \pm 0.14$ at $10^{15}\, M_\odot\, h^{-1}$. This model, shown as the red solid line in Figure 7, is in excellent agreement with our regression results (gray shaded area) with $c|_{z=0.34} = 3.95 \pm 0.35$ at $10^{15}\, M_\odot\, h^{-1}$, as well as with the stacked lensing measurements: $c_{200c} = 3.79^{+0.30}_{-0.28}$ (blue triangle; Section 5) from our stacked lensing analysis and $c_{200c} = 4.01^{+0.35}_{-0.32}$ (yellow contours) from the stacked shear-only analysis of Umetsu et al. (2014). The derived slope of $\beta = -0.44 \pm 0.19$ is somewhat steeper than, but consistent within errors with, the predicted values of $\beta = -0.160 \pm 0.108$ (Meneghetti et al. 2014). The intrinsic scatter, $\sigma_{Y|X} = 0.056 \pm 0.026$, is in agreement with the expected standard deviation of 0.61 around the mean 3.87 (Meneghetti et al. 2014), corresponding to $\sigma(\log_{10} c_{200c}) \sim 0.07$, or $\sigma(\ln c_{200c}) \sim 0.16$. This is significantly smaller than the typical intrinsic scatter predicted for the full (relaxed) population of halos, $\sigma(\log_{10} c_{200c}) \sim 0.14$–$0.16$ (0.1–0.12) (Neto et al. 2007; Duffy et al. 2008; Bhattacharya et al. 2013).

7. DISCUSSION

7.1. Systematic Errors

As described in Section 3, we have accounted for various sources of errors associated with our strong-lensing, weak-lensing shear and magnification measurements. All these errors are encoded in the measurement uncertainties (σ_+, σ_μ, σ_M) that enter the joint likelihood analysis (Section 3.6) and contribute to the posterior covariance matrix $\boldsymbol{C}^{\rm stat}$ of the mass profile solution $\boldsymbol{s} = \boldsymbol{\Sigma}/\Sigma_{\infty,c}$. In particular, our magnification bias analysis (Section 3.4) accounted for spurious large-scale variations of the red galaxy counts ($\sigma_\mu^{\rm sys}$), as well as the angular clustering ($\sigma_\mu^{\rm int}$) and Poisson error ($\sigma_\mu^{\rm stat}$) contributions. The fractional area $f_{\rm mask}$ lost to cluster members, foreground objects, and defects was

calculated as a function of clustercentric radius and corrected for in the source counts according to Equation (10). In our mass profile analysis, the total covariance matrix C includes additional contributions from the residual mass-sheet uncertainty $C^{\rm sys}$, the cosmic noise $C^{\rm lss}$, and the intrinsic variations $C^{\rm int}$ of the cluster signal due to the c–M variance, halo asphericity, and the presence of correlated halos (Section 3.6.3).

Additionally, we quantified potential sources of systematic errors in our weak-lensing shear+magnification measurements as follows (Section 3): (1) dilution of the weak-lensing signal by cluster members (2.4%, Section 3.2), (2) photometric-redshift bias in the mean depth estimates $\langle\beta\rangle$ (0.27%, Section 3.2), and (3) shear calibration uncertainty (5%, Section 3.3). These systematic errors scale approximately linearly with the cluster mass and add to 5.6% in quadrature. For the absolute calibration of cluster masses, one needs to take into account the systematic bias due to mass model uncertainties. Meneghetti et al. (2014) find that spherical NFW masses of cluster-sized halos estimated from their surface mass densities are biased low on average by 5% and that the bias is significantly reduced for relaxed halos (1%–2%) because they are more spherical than unrelaxed ones. According to their simulations, the degree of negative bias expected for our sample dominated by relaxed clusters is 3% (Massimo Meneghetti, private communication). Hence, the systematic uncertainty in the absolute mass calibration is estimated to be $\simeq$6%. This implies that the total uncertainty in the absolute mass calibration with the sample of 20 clusters is $\sqrt{0.28^2/20 + 0.06^2} \simeq 9\%$ at $\Delta_{\rm c} = 200$ (see Section 4.2).

7.2. Impact of Adding HST Lensing Data

A joint analysis of multi-scale, multiple lensing probes makes it possible to improve the precision of cluster mass profile reconstructions over a wide range of clustercentric radii and to self-calibrate systematics as well as observational parameters that describe the intrinsic properties of source populations (Rozo & Schmidt 2010; Umetsu 2013). When the wide-field CLASH weak-lensing data are combined with the inner *HST* lensing constraints ($N_{\rm SL} = 4$), the central weak-lensing bin $\Sigma(<0.'9)$ of Umetsu et al. (2014) is resolved into 5 radial bins of the surface mass density. We find a significant improvement of ~45% on average in terms of the total S/N (Equation (24)) from adding the *HST* lensing information to the wide-field weak-lensing data.

The improved sensitivity and resolution at 10″–40″ have also allowed us to determine the inner characteristic radius r_{-2} and the halo concentration $c_{200c} = r_{200c}/r_{-2}$ for each individual cluster (Tables 2). Umetsu et al. (2014) did not attempt to determine c_{200c} for each cluster because the weak-lensing profiles of individual clusters are highly degenerate in M_{200c} and c_{200c}, which can potentially bias the slope of the c–M relation determined from weak lensing (Hoekstra et al. 2011; Du & Fan 2014). This is particularly the case for high-z, low-mass systems, for which the characteristic profile curvature around r_{-2} is unconstrained by noisy and sparse weak-lensing data. For such clusters, the constraints on c_{200c} are essentially imposed by prior information. We note again that the $C^{\rm int}$ contribution to the total covariance matrix C was not included in the individual cluster mass measurements of Umetsu et al. (2014, Table 6), so that their mass measurement errors were underestimated (Section 4.2) with respect to this work.

A multi-probe approach combining complementary probes of cluster lensing allows us to test the consistency and robustness of cluster mass measurements (Umetsu 2013). Now we compare our weak+strong lensing mass estimates derived for our full sample of 20 CLASH clusters with the weak-lensing masses of Umetsu et al. (2014) to assess the level of systematic uncertainties in the ensemble mass calibration.

In Figure 8, we show for each cluster the weak+strong to weak lensing mass ratio, $M_{\rm 3D}^{\rm WL+SL}/M_{\rm 3D}^{\rm WL}$, as a function of spherical radius r. The results are shown in the range $r = [200, 2000]\,{\rm kpc}\,h^{-1}$ ($0.1 \lesssim r/r_{\rm 200m} \lesssim 1$) where the weak-lensing mass measurements were obtained by Umetsu et al. (2014, see their Figure 4). At each cluster radius, we compute the unweighted average of the mass ratios for our sample using geometric averaging (Donahue et al. 2014; Umetsu et al. 2014).[24] Figure 8 shows that the ensemble-averaged mass ratio $\langle M_{\rm 3D}^{\rm WL+SL}/M_{\rm 3D}^{\rm WL}\rangle$ is consistent with unity within the errors at all cluster radii. In particular, the mass offset is within 2% at $r \gtrsim 600\,{\rm kpc}\,h^{-1} \sim 1.5 r_{\rm 2500c}$. We see a trend for the average ratio to decrease toward the center, reaching 0.95 ± 0.06 at $r = 200\,{\rm kpc}\,h^{-1}$. This indicates that the *HST* analysis (Zitrin et al. 2015) favors relatively low central masses and hence low halo concentrations although the difference is not significant, $|\langle M_{\rm 3D}^{\rm WL+SL}/M_{\rm 3D}^{\rm WL}\rangle - 1| \leqslant 5\% \pm 6\%$, compared to the sensitivity limit with 20 clusters. This level of mass offset is smaller than, but consistent with, the value $8\% \pm 9\%$ based on the shear–magnification consistency test of Umetsu et al. (2014).

On the basis of these consistency checks, the residual systematic uncertainty in the ensemble mass calibration is estimated to be of the order ~5%–8% in the one-halo regime, $r = [200, 2000]\,{\rm kpc}\,h^{-1}$. This however implies that, on an individual cluster basis, there is a large scatter of ~20%–40% between different reconstruction methods that use different combinations of data. The level of uncertainty in the ensemble mass calibration (5%–8%) empirically estimated using different combinations of lensing probes is in agreement with the systematic uncertainty in the absolute mass calibration (6%) assessed in Section 7.1.

7.3. Ensemble Calibration of Cluster Masses

CLASH provides a sizable sample (20 clusters at $0.19 < z < 0.69$, $\bar{z} = 0.377$) for the calibration of the high end of the cluster mass function. In principle, weak lensing can yield unbiased mass estimates (assuming sphericity) for a sample of clusters that is largely free of orientation bias (Meneghetti et al. 2014). In practice, however, lensing mass measurements can be subject to various (known and unknown) systematic effects, as discussed in Section 7.1. In our early work (e.g., Broadhurst et al. 2005; Umetsu & Broadhurst 2008), we established that the dominant source of systematic effects in cluster weak lensing is the contamination of background galaxy samples by cluster members, which can lead to a substantial underestimation of the true lensing signal. This point has been supported by recent observations (Okabe et al. 2013; Applegate et al. 2014; Hoekstra et al. 2015) through systematic mass comparisons between different surveys that use different approaches to measuring weak lensing.

Here we compare our cluster mass estimates (Tables 2 and 3) with those obtained from other cluster lensing surveys that

[24] The geometric mean $\langle X\rangle$ is defined as $\langle X\rangle = (\prod_{n=1}^{N} X_n)^{1/N} = \exp\left(\frac{1}{N}\sum_{n=1}^{N}\ln X_n\right)$, so that $\langle Y/X\rangle = 1/\langle X/Y\rangle$ for the ratios of samples X and Y.

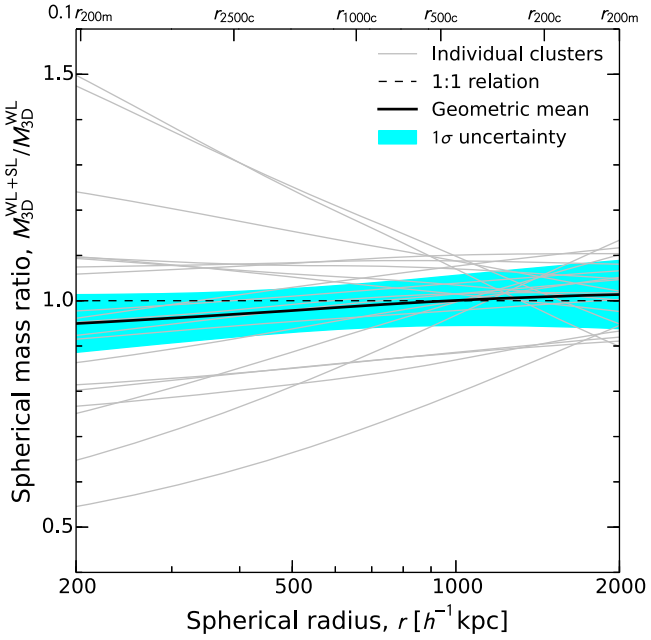

Figure 8. Ratio of cluster masses $M_{3D}(<r)$ from NFW fits to the Σ profile obtained in our weak+strong lensing analysis (Figure 11) and to that from the weak-lensing analysis by Umetsu et al. (2014). The results are shown for our full sample of 20 clusters (gray lines). The black line and the cyan-shaded area show the geometric-mean mass ratio and its 1σ uncertainty, respectively. The dashed horizontal line marks the 1:1 relation. This comparison shows that, adding the inner strong-lensing information to the weak-lensing constraints has a substantial impact on the individual cluster mass determinations at $r \lesssim r_{2500c}$. When averaged over the 20 clusters, our ensemble analysis shows no significant evidence for a systematic bias between weak-lensing-only and weak +strong-lensing measurements.

overlap with our sample, namely the *Weighing the Giants* program (WtG; Applegate et al. 2014), the Canadian Cluster Cosmology Project (CCCP; Hoekstra et al. 2015), and the LoCuSS (Okabe & Smith 2015, LoCuSS),[25] as well as with those from the SaWLens analysis of Merten et al. (2015). The WtG sample is a representative X-ray luminous subset of the *ROSAT* All-sky Survey (RASS) clusters at $0.15 < z < 0.7$, with a median redshift of $\bar{z} = 0.387$. The WtG clusters span a wide range of dynamical states, as well as of redshifts (von der Linden et al. 2014a). The CCCP sample is a mixture of X-ray luminous clusters for which archival *B*- and *R*-band observations made with the CFH12k camera on the 3.6 m Canada–France–Hawaii Telescope (CFHT) were available (Hoekstra 2007) and a temperature-selected subset of clusters drawn from the *ASCA* survey ($k_B T_X > 5$ keV, Hoekstra et al. 2012), spanning the range $0.15 < z < 0.55$ ($\bar{z} = 0.233$). The LoCuSS sample is drawn from the RASS catalogs at $0.15 < z < 0.3$ ($\bar{z} = 0.229$) and is approximately X-ray luminosity limited (Okabe & Smith 2015). The observed X-ray temperatures of the LoCuSS clusters are $k_B T_X \gtrsim 5$ keV (Martino et al. 2014, see their Figure 5). The LoCuSS sample is selected purely on the X-ray luminosity, ignoring other physical parameters and relaxation properties (Smith et al. 2015).

In all cases, the cluster masses are measured assuming a spherical NFW halo (Section 4.2). The WtG and LoCuSS mass measurements are based on weak-lensing observations with Subaru/Suprime-Cam, while the CCCP survey uses weak-lensing data taken with CFHT. The CCCP and LoCuSS surveys used the BCG as the cluster center as done in our work (Section 3.1), whereas the WtG survey adopted the X-ray centroid as the cluster center (von der Linden et al. 2014a). We note that, for all clusters in our sample, the mass measurements presented in Tables 2 and 3 are insensitive to the choice of the cluster center as discussed in Section 3.1. Another key difference is that the LoCuSS and CLASH surveys controlled contamination of their background galaxy samples at the $\lesssim$2% level by imposing stringent color cuts (Section 3.2), albeit with increased shot noise, whereas the WtG and CCCP surveys boosted the diluted shear signal to correct statistically for contamination, by assuming that the observed number density profile of a pure background galaxy sample is flat. This correction, referred to as a boost factor, is not valid in general as it ignores the depletion or enhancement of the number density of background galaxies due to magnification bias (Umetsu et al. 2014; Chiu et al. 2015; Okabe & Smith 2015; Ziparo et al. 2015).

In the following, we compare cluster masses between two studies by using the same aperture radii to avoid aperture mismatch problems. These comparisons are limited to those overdensity radii (r_Δ) where the fitting ranges typically overlap. The results of the comparisons are shown in Figure 9. For each case, we calculate the mass ratios for the overlap sample using the unweighted geometric mean (Section 7.2), unless otherwise noted.

7.3.1. CLASH: Merten et al. (2015)

There are 16 clusters in common with the CLASH SaWLens analysis of Merten et al. (2015). These are all CLASH X-ray-selected clusters. Merten et al. (2015) measure masses by reconstructing two-dimensional convergence maps of individual clusters, binning the maps into Σ profiles, and fitting these profiles with an NFW model within 2 Mpc h^{-1} ($R \lesssim r_{\rm vir}$), closely following the procedure suggested by Meneghetti et al. (2014). An important difference between the data used by Merten et al. (2015) and the data used here is the availability of azimuthally integrated magnification constraints (Umetsu et al. 2014).[26]

This comparison shows that, on average, the SaWLens masses are 7% ± 6% lower than our masses at $\Delta_c = \Delta_{\rm vir}$, 200, and 500; their masses are 9% ± 11% lower than our masses at $\Delta_c = 2500$. This difference is smaller than the systematic mass offset of ∼10% ± 5% at $r = 0.5$ Mpc, 1 Mpc, and r_{500c} found between the CLASH weak-lensing (Umetsu et al. 2014) and SaWLens (Merten et al. 2015) mass profiles (see Donahue et al. 2014, Table 6). Hence, combining the central *HST*-lensing and outer weak-lensing data has reduced the discrepancy with respect to the SaWLens results. We find that this remaining discrepancy can be attributed to the three outliers discussed in Section 4.1, which correspond to clusters at the lowest Galactic latitudes of the overlap sample (MACS J1931.82635, MACS J0744.9+3927) and those at the highest redshifts (RX J1347.51145, MACS J0744.9+3927) which exhibit complex mass distributions with a high degree of substructure (Postman et al. 2012; Merten et al. 2015). When excluding the three outliers, we find that the SaWLens mass estimates ($M_{\rm SaWLens}$) are statistically in excellent agreement with our results ($M_{\rm CLASH}$) at all overdensities:

[25] http://www.sr.bham.ac.uk/locuss

[26] Merten et al. (2015) and Zitrin et al. (2015) use identical sets of *HST* lensing constraints (i.e., *HST* shear catalogs plus locations and redshifts of multiple images) as input for respective mass reconstructions. Merten et al. (2015) simultaneously combine the *HST* lensing constraints and ground-based shear catalogs of Umetsu et al. (2014). In this work, lensing constraints are combined a posteriori in the form of radial profiles according to the procedure described in Section 3.6.

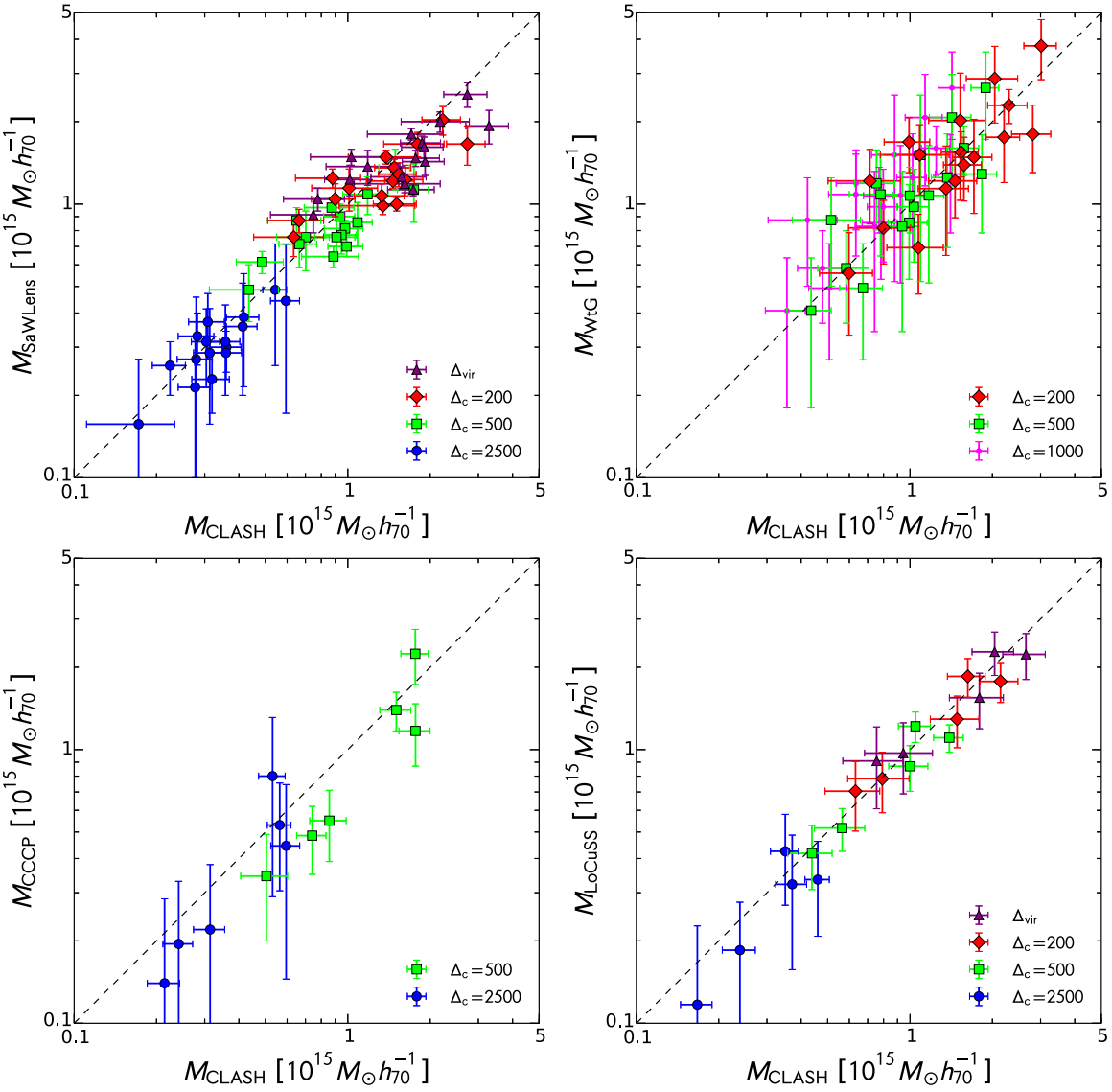

Figure 9. Comparison of our weak+strong lensing mass measurements ($M_{\rm CLASH}$) of 20 clusters to results from Merten et al. (2015, SaWLens), Applegate et al. (2014, WtG), Hoekstra et al. (2015, CCCP), and Okabe & Smith (2015, LoCuSS). For each comparison, we measure the mass of clusters within characteristic overdensity radii r_Δ of the respective work assuming the spherical NFW density profile (Section 7.3). The dashed line shows the one-to-one relation.

$\langle M_{\rm SaWLens}/M_{\rm CLASH}\rangle = 1.01 \pm 0.07$, 1.00 ± 0.07, 0.99 ± 0.07, and 0.95 ± 0.12 at $\Delta_{\rm c} = \Delta_{\rm vir}$, 200, 500, and 2500, respectively. We note that this agreement is achieved in spite of using substantially different reconstruction methods even though the data used are largely common to the two analyses.

7.3.2. The WtG Project

The WtG collaboration conducted weak-lensing shear mass measurements for 51 X-ray-selected luminous clusters at $0.15 \lesssim z \lesssim 0.7$ ($\bar{z} = 0.387$) using deep multi-color Subaru/Suprime-Cam and CFHT/MegaPrime optical imaging (Applegate et al. 2014; von der Linden et al. 2014a). Their cluster sample includes the majority of the CLASH clusters. There are 17 clusters in common between the two studies, both of which use Subaru data. The overlap sample includes 14 CLASH X-ray-selected clusters and 3 high-magnification clusters. Applegate et al. (2014) derived cluster masses from NFW fits to reduced tangential shear profiles over the radial range 0.75–3 Mpc h_{70}^{-1} ($R \gtrsim 0.8 r_{1000c}$) assuming a fixed concentration parameter of $c_{200c} = 4$ for all clusters. In contrast, we have measured masses from NFW fits to surface mass density profiles within $R \leqslant 2$ Mpc $h^{-1} \simeq 2.9$ Mpc h_{70}^{-1}, allowing both M_{200c} and c_{200c} as free parameters (see Section 4.2). This fitting procedure is the same as that adopted by Umetsu et al. (2014) and Merten et al. (2015).

In the upper-right panel of Figure 9 we compare shear-only masses ($M_{\rm WtG}$) of Applegate et al. (2014) and our full-lensing masses ($M_{\rm CLASH}$), obtaining good agreement. We find that the WtG masses are $3\% \pm 9\%$, $7\% \pm 12\%$, and $7\% \pm 12\%$ higher than our masses at $\Delta_{\rm c} = 200$, 500, and 1000, respectively. We see a trend of increasing mass offset with increasing overdensity (or, decreasing overdensity radius r_Δ). However, the offsets are well within the 1σ errors and not statistically significant.

7.3.3. The CCCP

The CCCP conducted weak-shear lensing mass measurements for a sample of 52 clusters at $0.15 < z < 0.55$ ($\bar{z} = 0.233$) on

the basis of CFHT observations. We have 6 clusters in common with the CCCP project, including 5 CLASH X-ray-selected clusters (Abell 383, Abell 209, Abell 2261, Abell 611, RX J1347.5−1145) and one high-magnification cluster (MACS J0717.5+3745). Hoekstra et al. (2015) measure NFW masses from CFHT reduced tangential shear measurements within 0.5–2 Mpc h_{70}^{-1} ($r_{2500c} \lesssim R \lesssim 1.5r_{500c}$), assuming the c–M relation of Dutton & Macciò (2014; see Section 7.4.1).

We find that this mass comparison is somewhat sensitive to weighting schemes because of the large observational uncertainties in the CFHT-based CCCP masses (with a typical uncertainty of ∼34%) and of the small number of clusters. Taking the error-weighted geometric mean (down-weighting clusters with noisy mass measurements), we find that the CCCP masses are on average 16% ± 10% and 9% ± 24% lower than our masses at $\Delta_c = 500$ and 2500, respectively. With limited statistics, we do not find statistically significant differences between the CCCP and our masses. We note that Hoekstra et al. (2015) obtained an excellent agreement between the Subaru weak-lensing masses of Umetsu et al. (2014) and their masses measured from the Subaru imaging data processed by the CLASH collaboration.[27] Hoekstra et al. (2015) found that the Subaru-based CCCP masses are on average only ∼2.4% lower than the CLASH weak-lensing masses of Umetsu et al. (2014). Since our mass calibration is highly consistent with that of Umetsu et al. (2014; Section 7.2), a similar improvement is expected when the Subaru-based CCCP masses are compared to our weak+strong lensing masses.

7.3.4. The LoCuSS

The LoCuSS has carried out a systematic weak-shear lensing analysis of a sample of 50 X-ray luminous clusters at $0.15 < z < 0.3$ ($\bar{z} = 0.229$) based on deep two-band imaging with Subaru/Suprime-Cam (Okabe & Smith 2015). There are 5 clusters in common between the LoCuSS and our samples (Abell 383, Abell 209, Abell 2261, RX J2129.7+0005, Abell 611). Both studies use Subaru weak-shear lensing data. To reduce biases due to noisy inner profiles, Okabe & Smith (2015) optimize the binning scheme (i.e., the fitting range and the number of bins) for each individual cluster. They perform NFW fits to a suite of reduced tangential shear profiles that span inner radii in the range 50–300 kpc h^{-1}, outer radii in the range 2000–3000 kpc h^{-}, and number of bins in the range 4–8. The NFW concentration parameter is treated as a free parameter in their fits.

For this comparison, we obtain excellent agreement between the LoCuSS masses ($M_{\rm LoCuSS}$) and our masses, even on an individual cluster basis (see the lower-right panel of Figure 9). Accordingly, the comparison results are insensitive to the choice of weighting schemes. The LoCuSS masses are on average 0% ± 15%, 2% ± 13%, 7% ± 10%, and 16% ± 22% lower than our masses at $\Delta_c = \Delta_{\rm vir}$, 200, 500, and 2500, respectively. A better agreement is seen for lower overdensities where the constraints are dominated by the Subaru weak-lensing measurements. A possible explanation for this excellent agreement is the fact that both surveys controlled contamination of the background samples at the $\lesssim$2% level without employing a boost factor (Section 7.3) and both used independent but very similar shape measurement algorithms. In particular, Okabe & Smith (2015) adopted a shear calibration procedure that is nearly identical to the one developed by Umetsu et al. (2010) and adopted by Umetsu et al. (2014; see Section 3.3). Okabe & Smith (2015) obtained a shear calibration bias of $m \sim -3\%$, which is close to the value derived by Umetsu et al. (2010, $m \sim -5\%$). We note that adding the inner strong-lensing information (Zitrin et al. 2015) to the weak-lensing constraints (Umetsu et al. 2014) has resulted in, on average, a decrease of the mass estimates, especially at $r \lesssim 1.5r_{2500c}$ (see Figure 8; Section 7.2).

7.4. Cluster c–M Relation

7.4.1. Comparison with ΛCDM Predictions from the Literature

We compare our individual cluster mass and concentration measurements (Table 2; Figure 7) with predictions from numerical simulations in the literature. To statistically quantify the level of agreement with a given predicted c–M relation, we use frequentist measures of goodness of fit. Specifically, for a given fixed $c(M, z)$ function, we evaluate the χ^2 goodness of fit to the null hypothesis that the sample data are derived from the model population. The χ^2 statistic is then defined as

$$\chi^2 = \sum_n \left[\frac{\log_{10} c_n - \log_{10} c(M_n, z_n)}{\sigma_n} \right]^2, \tag{41}$$

where σ_n is the total statistical uncertainty of the nth cluster,

$$\sigma_n^2 = \sigma_{\rm int,0}^2 + C_{yy,n} + \beta_0^2 C_{xx,n} - 2\beta_0 C_{xy,n} \tag{42}$$

with β_0 the mass slope of the intrinsic c–M relation under consideration and $\sigma_{\rm int,\,0}$ the intrinsic scatter in $\log_{10} c_{200c}$ at fixed mass and redshift. For all models, we fix $\sigma_{\rm int,0} = \sigma_{Y|X} \simeq 0.057$ according to our regression results (Section 6.1) and assume that the effective number of parameters for the null model is three (i.e., the intercept, mass slope, and redshift evolution).

Table 5 lists for each model the values of χ^2 and PTE, along with the weighted geometric average[28] and the standard deviation of observed-to-predicted concentration ratios $c^{\rm (obs)}/c^{\rm (pred)}$. The theoretical predictions from Meneghetti et al. (2014) are based on nonradiative simulations of DM and baryons, and those from the others are based on DM-only simulations. In all cases, halo masses and concentrations are defined using the overdensity $\Delta_c = 200$ and measured assuming the spherical NFW profile, either in projection (2D) or in three-dimensions (3D). For peak-height-based $c(\nu)$ relations (Prada et al. 2012; Diemer & Kravtsov 2015), we assume the *WMAP* seven-year cosmology of Komatsu et al. (2011) to calculate the relationship between peak height and halo mass at each redshift.[29]

We first consider models for the full population of halos based on the three-dimensional characterization of the halo density profile. We find that recent c–M relations from Bhattacharya et al. (2013), Dutton & Macciò (2014), Meneghetti et al. (2014), and Diemer & Kravtsov (2015) are in satisfactory agreement with the data. The Meneghetti et al. (2014) model (PTE = 0.675), which is calibrated for a cosmology with a relatively high normalization ($h = 0.7$, $\Omega_{\rm m} = 0.27$, $\sigma_8 = 0.82$; Section 6.2), yields the highest goodness of fit among those considered here, followed by the Dutton & Macciò (2014) model (PTE = 0.659) calibrated for the

[27] https://archive.stsci.edu/prepds/clash/

[28] Specifically, the weighted geometric average $\langle Y/X \rangle$ is defined as $\langle Y/X \rangle = \exp\left\{ \left[\sum_n u_n \ln(Y_n/X_n)\right] \left(\sum_n u_n\right)^{-1} \right\}$ with u_n the inverse variance weight for the nth cluster, $u_n^{-1} = \sigma_{X,n}^2/X_n^2 + \sigma_{Y,n}^2/Y_n^2$.

[29] We find that the average mass of the CLASH X-ray-selected subsample corresponds to a halo peak height of $\nu \simeq 3.8$ in the adopted cosmology.

Table 5
Comparison of Measured and Predicted Concentrations for the CLASH X-Ray-selected Subsample

Author	Sample	3D/2D	Function[a]	$c^{(\mathrm{obs})}/c^{(\mathrm{pred})}$ Average[c]	σ[d]	χ^2	PTE[b]
Theory:							
Duffy et al. (2008)	full	3D	c–M	1.331 ± 0.108	0.334	22.6	0.046
Duffy et al. (2008)	relaxed	3D	c–M	1.165 ± 0.094	0.290	13.6	0.399
Prada et al. (2012)	full	3D	c–ν	0.733 ± 0.065	0.244	24.6	0.026
Bhattacharya et al. (2013)	full	3D	c–ν	1.169 ± 0.095	0.292	14.1	0.369
Bhattacharya et al. (2013)	relaxed	3D	c–ν	1.131 ± 0.092	0.277	12.4	0.494
Dutton & Macciò (2014)	full	3D	c–M	1.061 ± 0.086	0.262	10.4	0.659
Meneghetti et al. (2014)	full	3D	c–M	1.061 ± 0.089	0.279	10.2	0.675
Meneghetti et al. (2014)	relaxed	3D	c–M	0.990 ± 0.083	0.249	9.2	0.760
Diemer & Kravtsov (2015)	full (median)	3D	c–ν	1.021 ± 0.083	0.330	14.4	0.349
Diemer & Kravtsov (2015)	full (mean)	3D	c–ν	1.060 ± 0.086	0.326	13.8	0.391
Meneghetti et al. (2014)	full	2D	c–M	1.087 ± 0.092	0.336	13.5	0.413
Meneghetti et al. (2014)	relaxed	2D	c–M	1.040 ± 0.086	0.283	10.8	0.628
Meneghetti et al. (2014)	CLASH	2D	c–M	0.988 ± 0.078	0.227	9.6	0.730
Observations:							
Merten et al. (2015)	CLASH	2D	c–M	1.133 ± 0.087	0.209	9.2	0.754

Notes.
[a] c–M: power-law $c(M, z)$ relation; c–ν: halo concentration given as a function of peak height $\nu(M, z)$.
[b] Probability to exceed the measured χ^2 value assuming the standard χ^2 probability distribution function.
[c] Weighted geometric average of observed-to-predicted concentration ratios.
[d] Standard deviation of the distribution of observed-to-predicted concentration ratios.

Planck cosmology ($h = 0.671, \Omega_{\mathrm{m}} = 0.3175, \sigma_8 = 0.8344$). Our measurements are $33\% \pm 11\%$ higher than the predictions of Duffy et al. (2008) based on the *WMAP* five-year cosmology ($h = 0.742$, $\Omega_{\mathrm{m}} = 0.258$, $\sigma_8 = 0.796$). This is in line with the findings of Dutton & Macciò (2014), who showed that the c–M relation in the *WMAP* five-year cosmology has a 20% lower normalization at $z = 0$ than in the *Planck* cosmology. On the other hand, the observed concentrations are $27\% \pm 7\%$ lower than the predictions of Prada et al. (2012). Their model exhibits a flattening and upturn of the c–M relation in the high ν regime, so that their concentrations derived for cluster halos are substantially higher than those of others. We refer the reader to Meneghetti & Rasia (2013) and Diemer & Kravtsov (2015) for detailed discussions on the possible origin of this discrepancy.

Next, we consider models derived for relaxed populations of cluster halos (Duffy et al. 2008; Bhattacharya et al. 2013; Meneghetti et al. 2014). Numerical simulations suggest that relaxed subsamples have concentrations that are on average ~10% higher than for the full samples. In all cases, we find improved agreement with the data compared to the full-sample comparison (Table 5). This is consistent with the expectation that the CLASH X-ray-selected subsample is largely composed of relaxed clusters (Section 6.2). For the Meneghetti et al. (2014) model, the agreement is particularly excellent, with a PTE of 0.760.

Finally, we examine the two-dimensional c–M relations of Meneghetti et al. (2014) obtained from fitting Σ profiles of simulated halos (Section 6.2).[30] As summarized in Table 5, we find a better agreement with the model that explicitly takes into account the CLASH selection function based on X-ray morphology (PTE = 0.730).

In summary, we find that, overall, cluster c–M relations that are calibrated for recent cosmologies yield good agreement with the observations (Bhattacharya et al. 2013; Dutton & Macciò 2014; Meneghetti et al. 2014; Diemer & Kravtsov 2015). An improved agreement is achieved when selection effects are taken into account in the models (Duffy et al. 2008; Bhattacharya et al. 2013; Meneghetti et al. 2014), matching the characteristics of the CLASH clusters in terms of the overall degree of relaxation and X-ray morphological regularity.

7.4.2. Comparison with the SaWLens Results

The observational c–M relation of Merten et al. (2015) is derived from their SaWLens analysis of a sample of 19 CLASH X-ray-selected clusters (Section 4.1; Figure 11). Their sample includes all 16 clusters in our X-ray-selected subsample. Their NFW concentrations scale with halo mass and redshift as $c \propto M^{-0.32\pm0.18}$ and $c \propto (1+z)^{0.14\pm0.52}$ with a normalization of $c|_{z=0.37} = 3.66 \pm 0.16$ at $M_{200\mathrm{c}} = 8 \times 10^{14}\, M_\odot\, h^{-1}$. Their slope is in good agreement with our results, while their normalization is somewhat lower than our measurement (Sections 6.1 and 6.2). The best-fit c–M relation of Merten et al. (2015) is compared with our regression results in Figure 7. We see that the confidence regions overlap well at the 1σ level. The Merten et al. (2015) relation is also in agreement with the stacked lensing results of Umetsu et al. (2014) and those of this work. As discussed by Merten et al. (2015), their normalization is slightly lower than that of the Meneghetti et al. (2014) relation predicted for the CLASH-like X-ray-selected halos and in better agreement with that of the full-sample relation (including both relaxed and unrelaxed halos).

A quantitative comparison of the Merten et al. (2015) c–M relation with our individual cluster measurements is summarized in Table 5. The observed-to-predicted concentration ratio has a small scatter of 0.209 around the mean value of 1.133 ± 0.087 and shows an excellent goodness of fit, with PTE = 0.754. A direct comparison for the 16 clusters in common shows that our NFW concentrations (Table 2) are $9.7\% \pm 10.3\%$ higher than those obtained by Merten et al. (2015). We emphasize here that

[30] We refer to Meneghetti et al. (2014) and Giocoli et al. (2012) for general discussions on the effects of projection bias in measuring the c–M relation from lensing.

this agreement comes in spite of using substantially different reconstruction methods even though the data and sample used are largely common to the two studies. A multi-probe approach for cluster lensing is one of the great advantages of the CLASH survey, providing consistency checks between different lensing methods and different data sets (Coe et al. 2012; Umetsu et al. 2012, 2014; Medezinski et al. 2013).

7.4.3. Revisiting the Overconcentration Problem

In contrast to the CLASH X-ray-selected subsample, clusters selected to have large Einstein radii ($\theta_{\rm Ein}$) represent a highly biased population with their major axis preferentially aligned with the line of sight. A population of such *superlenses* might also be biased toward halos with intrinsically higher concentrations (Hennawi et al. 2007). In the context of ΛCDM, the projected mass distributions of superlens clusters have ∼40%–60% higher concentrations than typical clusters with similar masses and redshifts (Oguri & Blandford 2009).

Prior to the CLASH survey, Umetsu et al. (2011a, hereafter U11) performed a strong-lensing, weak-lensing shear and magnification analysis of four strong-lensing-selected clusters of similar masses (A1689, A1703, A370, and Cl0024+17) at $\langle\langle z_{\rm l}\rangle\rangle \simeq 0.32$ using high-quality *HST* and Subaru observations. These clusters display prominent strong-lensing features, characterized by $\theta_{\rm Ein} \gtrsim 30''$ ($z_{\rm s} = 2$). U11 show that the stacked $\langle\langle\Sigma\rangle\rangle$ profile of the four clusters is well described by a single NFW profile in the one-halo regime, with an effective concentration of $c_{\rm vir} = 7.68^{+0.42}_{-0.40}$ ($c_{\rm 200c} \simeq 6.29$) at $M_{\rm vir} = 22.0^{+1.6}_{-1.4} \times 10^{14}\, M_\odot\, h_{70}^{-1}$ ($M_{\rm 200c} \simeq 19.4 \times 10^{14}\, M_\odot h_{70}^{-1}$), corresponding to an Einstein radius of $\theta_{\rm Ein} \simeq 36''$ ($z_{\rm s} = 2$). Semianalytical simulations of ΛCDM incorporating idealized triaxial halos yield a ∼40%–60% bias correction for a strong-lensing cluster population (Oguri & Blandford 2009). After applying a 50% superlens correction, U11 found a discrepancy of $\sim 2\sigma$ with respect to the Duffy et al. (2008) *c*–*M* relation based on the *WMAP* five-year cosmology. U11 conclude that there is no significant tension between the concentrations of their clusters and those of CDM halos if large lensing biases are coupled to a sizable intrinsic scatter in the *c*–*M* relation.

Figure 10 compares in the *c*–*M* plane the stacked full-lensing constraints for our CLASH X-ray-selected subsample (blue contours; NFW+LSS (i) in Table 4) and those for the strong-lensing-selected sample of U11 (gray contours). In the figure we overplot theoretical *c*–*M* relations of Duffy et al. (2008), Bhattacharya et al. (2013), Dutton & Macciò (2014), Meneghetti et al. (2014), and Diemer & Kravtsov (2015, their mean relation; see Table 5), all evaluated for the full population of halos at the mean redshift $\langle\langle z_{\rm l}\rangle\rangle \simeq 0.32$ of the U11 sample. Figure 10 demonstrates that *c*–*M* relations that are calibrated for more recent cosmologies and simulations provide better agreement with our CLASH measurements (see Section 7.4.1).

To account for the superlens bias in the U11 sample, we plot each of the *c*–*M* models with a maximal 60% correction (Oguri & Blandford 2009). We find that, once the effects of selection and orientation bias are taken into account, the full-lensing results of U11 come into line with the models of Dutton & Macciò (2014), Meneghetti et al. (2014), and Diemer & Kravtsov (2015), the three most recent *c*–*M* models studied in this work. Hence, the discrepancy found by U11 can be fully reconciled by the higher normalization of the *c*–*M* relation as favored by recent *WMAP* and *Planck* cosmologies.

8. SUMMARY AND CONCLUSIONS

We have presented a comprehensive analysis of strong-lensing, weak-lensing shear and magnification data for a sample of 16 X-ray-selected and 4 high-magnification-selected galaxy clusters at $0.19 \lesssim z \lesssim 0.69$ (Table 1) targeted in the CLASH survey (Postman et al. 2012). Our analysis combines constraints from 16-band *HST* observations (Zitrin et al. 2015) and wide-field multi-color imaging (Umetsu et al. 2014) taken primarily with Subaru/Suprime-Cam, spanning a wide range of cluster radii, $\theta = 10''$–$16'$. We have carefully taken into account several major sources of uncertainties in our error analysis (Section 3).

We have reconstructed surface mass density profiles $\boldsymbol{\Sigma}$ of all clusters from a joint analysis of strong-lensing, weak-lensing shear and magnification constraints (Section 4; Figure 11), providing a unique cluster mass profile data set. We find a significant improvement of ∼45% on average in terms of the total S/N of the cluster mass profile measurement from adding the central *HST* lensing constraints ($10''$–$40''$) to the wide-field weak-lensing data ($0.'9$–$16'$).

With the improved sensitivity and resolution at $10''$–$40''$, we have measured masses and concentrations from these mass profiles for individual clusters assuming a spherical NFW halo (Tables 2 and 3). The median precision on individual cluster mass measurements is found to be ∼28%, 24%, 23%, and 24% at $\Delta_{\rm c} = 200$, 500, 1000, and 2500, respectively. We assessed the internal consistency of cluster mass measurements across the multiple probes of cluster lensing effects (Section 7.2). We find internal consistency of the ensemble mass calibration to be $\leqslant 5\% \pm 6\%$ in the one-halo regime, $r = 200$–$2000\,{\rm kpc}\,h^{-1}$ ($0.01 \lesssim r/r_{\rm 200m} \lesssim 1$; Figure 8), by comparison with the CLASH weak-lensing-only measurements of Umetsu et al. (2014). This level of uncertainty in the ensemble mass calibration, empirically estimated using different combinations of lensing probes, is in agreement with the systematic uncertainty in the absolute mass calibration of ≃6% assessed in Section 7.1. This implies that the total uncertainty in the absolute mass calibration with the sample of 20 clusters is $\sqrt{0.28^2/20 + 0.06^2} \simeq 9\%$ at $\Delta_{\rm c} = 200$ (Section 4.2).

The CLASH X-ray-selected sample was selected to have a high degree of regularity in their X-ray morphology (Postman et al. 2012). Numerical simulations suggest that this sample is prevalently composed of relaxed clusters (∼70%) and largely free of orientation bias (Meneghetti et al. 2014). An important effect of the CLASH selection function is to significantly reduce the scatter in concentration because of their X-ray regularity (Section 6.2). For a lensing-unbiased subsample of 16 CLASH X-ray-selected clusters, we have examined the mean *c*–*M* relation and its intrinsic scatter using Bayesian regression methods (Section 6; Figures 6 and 7). Our analysis takes into account the correlation between the errors on mass and concentration and the effects of nonuniformity of the intrinsic mass probability distribution. Our model yields a mean concentration of $c|_{z=0.34} = 3.95 \pm 0.35$ at $M_{\rm 200c} = 10^{15}\, M_\odot\, h^{-1} \simeq 14 \times 10^{14}\, M_\odot\, h_{70}^{-1}$ and an intrinsic scatter of $\sigma(\log_{10} c_{\rm 200c}) = 0.056 \pm 0.026$, or $\sigma(\ln c_{\rm 200c}) = 0.13 \pm 0.06$. The normalization, slope, and scatter of the observed *c*–*M* relation are all consistent with ΛCDM predictions (Meneghetti et al. 2014) when the projection effects and the CLASH selection function based on X-ray morphological regularity are taken into account. Our regression results are in agreement with the SaWLens analysis of Merten et al. (2015) and the stacked shear-only analysis of Umetsu et al. (2014). This multi-probe

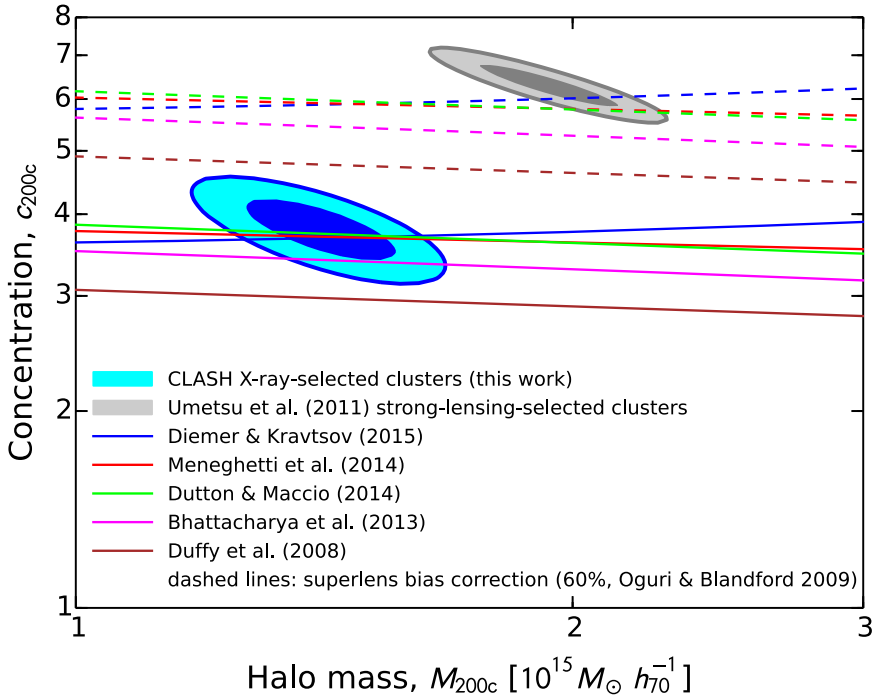

Figure 10. Joint constraints on the mass and concentration parameters (M_{200c}, c_{200c}) for our CLASH X-ray-selected subsample ($\langle\langle z_l\rangle\rangle \simeq 0.34$; blue contours) and the strong-lensing-selected sample of Umetsu et al. (2011a; $\langle\langle z_l\rangle\rangle \simeq 0.32$; gray contours) derived from the respective lensing analyses of *HST*+Subaru observations. For each case, the contours show the 68.3% and 95.4% confidence levels ($\Delta\chi^2 = 2.3$ and 6.17). The results are compared to theoretical c–M relations (solid lines) from numerical simulations of ΛCDM cosmologies (Duffy et al. 2008; Bhattacharya et al. 2013; Dutton & Macciò, 2014; Meneghetti et al. 2014; Diemer & Kravtsov 2015), all evaluated at $z \simeq 0.32$ for the full population of halos. The dashed lines show 60% superlens corrections to the solid lines, accounting for the effects of selection and orientation bias expected for a strong-lensing cluster population (60%; Oguri & Blandford 2009). Once the effects of superlens bias are taken into account, the stacked-lensing constraints on the Umetsu et al. (2011a) sample come into line with the models of Dutton & Macciò (2014), Meneghetti et al. (2014), and Diemer & Kravtsov (2015), the three most recent c–M models studied in this work.

approach for cluster lensing is one of the key advantages of the CLASH survey, providing consistency checks between different lensing methods and different data sets.

We have derived an ensemble-averaged surface mass density profile $\langle\langle\boldsymbol{\Sigma}\rangle\rangle$ at an average redshift of $\langle\langle z_l\rangle\rangle \simeq 0.34$ for the X-ray-selected subsample of 16 clusters by stacking their individual $\boldsymbol{\Sigma}$ profiles (Section 5; Figure 3). The stacked lensing signal is detected at 33σ significance over the entire radial range, $R \leqslant 4000\,\mathrm{kpc}\,h^{-1}$, accounting for the effects of intrinsic profile variations and uncorrelated LSS along the line of sight (Figure 1).

Our CLASH lensing determination of the cluster mass distribution provides a firm basis for a detailed comparison with theoretical models. We show that the $\langle\langle\boldsymbol{\Sigma}\rangle\rangle$ profile is well described by a family of density profiles predicted for DM-dominated halos in gravitational equilibrium (Table 4; Figure 4), namely, the NFW, Einasto, and DARKexp models. Of these, the first two are phenomenological models and the last is a theoretically derived model (Hjorth & Williams 2010; Williams & Hjorth 2010). The single power-law, cored isothermal and Burkert density profiles are disfavored by the observed mass profile having a pronounced radial curvature.

We find that cuspy halo models that include the large-scale two-halo contribution using the b_h–M relation of Tinker et al. (2010) provide improved agreement with the data. Independent of the chosen halo density profile, we find $b_h(M_{200c}) \sim 9.3$ ($b_h\sigma_8^2 \sim 6.1$). For the NFW halo model (NFW+LSS (i)), we measure a mean concentration of $c_{200c} = 3.79^{+0.30}_{-0.28}$ at $M_{200c} = 14.1^{+1.0}_{-1.0} \times 10^{14}\,M_\odot\,h_{70}^{-1}$, demonstrating consistency between complementary analysis methods (Figure 7). This model yields an Einstein radius of $\theta_{\rm Ein} = 14.0^{+3.4}_{-3.2}$ arcsec at $z_s = 2$, which agrees within 2σ with the observed median Einstein radius of $\overline{\theta}_{\rm Ein} = 20.''1$ ($z_s = 2$) for this subsample (Section 3.5). The Einasto shape parameter is constrained to be $\alpha_E = 0.248^{+0.051}_{-0.047}$ ($1/\alpha_E = 4.03^{+0.93}_{-0.69}$), which is in good agreement with predictions from ΛCDM numerical simulations (Gao et al. 2008; Meneghetti et al. 2014).

A systematic comparison between different cluster lensing surveys that use different approaches to measuring the masses of clusters allows us to identify (known and unknown) systematic effects. In the last few years, a substantial effort has been devoted to establishing an accurate mass calibration from cluster lensing (von der Linden et al. 2014b; Hoekstra et al. 2015; Israel et al. 2015), in light of the apparent tension in cosmological constraints from *Planck* primary CMB data and SZE cluster counts (Planck Collaboration et al. 2014, 2015). We compared our CLASH lensing masses (Tables 2 and 3) with weak-lensing masses from other surveys (WtG, CCCP, LoCuSS). Our mass measurements are in excellent agreement within 1σ with the WtG (Applegate et al. 2014) and LoCuSS (Okabe & Smith 2015) surveys, with which we have 17 and 5 clusters in common, respectively. At higher mass overdensities $\Delta_c \gtrsim 500$ where weak-lensing measurements are subject to various systematics, the agreement appears to be less impressive (Sections 7.3.2 and 7.3.4). We find that our measurements are on average 16% and 9% higher than the CCCP measurements at $\Delta_c = 500$ and 2500, respectively. With limited statistics, however, we do not find statistically significant differences between the CCCP and CLASH results.

Our mass measurements are found to be ∼7%–9% higher than the CLASH SaWLens results of Merten et al. (2015), with

which we have 16 clusters in common. This difference is smaller than the systematic mass offset of ∼10% ± 5% found between the CLASH weak-lensing (Umetsu et al. 2014) and SaWLens (Merten et al. 2015) mass profiles. Hence, combining the central *HST*-lensing and outer weak-lensing data has reduced the discrepancy with respect to the SaWLens results. We find that this remaining discrepancy can be attributed to three outliers (Section 4.1), which correspond to clusters at the lowest Galactic latitudes ($b < 30°$) of the overlap sample and those at the highest redshifts ($z \gtrsim 0.45$) which exhibit complex mass distributions with a high degree of substructure (Postman et al. 2012; Merten et al. 2015). Since the data used are largely common to the two analyses except for the inclusion of weak-lensing magnification data in this work, this discrepancy likely arises from systematics in the present calibration of magnification measurements for these low Galactic latitude clusters and high-redshift clusters. Weak lensing reconstructions are sensitive to the treatment of boundary conditions if there are massive structures near the data boundaries. Hence, mass profile reconstructions for clusters with high degrees of substructure can be subject to a greater degree of mass-sheet degeneracy. Excluding the three outliers brings the two results into agreement within 1% at $\Delta_c = \Delta_{vir}$, 200, and 500 and within 5% at $\Delta_c = 2500$.

In the CLASH survey (Postman et al. 2012), we have demonstrated the power of multi-probe, multi-scale data sets available from a space telescope cluster survey (Merten et al. 2015; Zitrin et al. 2015) combined with X-ray (Donahue et al. 2014), SZE (Sayers et al. 2013; Czakon et al. 2015), and wide-field imaging plus spectroscopic (Rosati et al. 2014; Umetsu et al. 2014) follow-up observations. Extending this type of cluster survey to a large sky area, as planned for the WFIRST and Euclid missions, will be a significant step forward in obtaining a comprehensive picture of the evolution of clusters over cosmic time and across populations, as well as in understanding the evolutionary and tidal effects of surrounding LSS on the mass distribution of the central cluster.

We thank the anonymous referees for their careful reading of the manuscript and useful suggestions. This work was made possible by the availability of high-quality lensing data produced by the CLASH team. We express our gratitude to all members of the CLASH team who enabled us to carry out the work. We thank all authors of Umetsu et al. (2014) and Zitrin et al. (2015) for their valuable contributions to the lensing analyses used here. We thank John Moustakas for his assistance in the early stages of this work. We thank Massimo Meneghetti and Elinor Medezinski for providing useful information and suggestions. We acknowledge very fruitful discussions with Mauro Sereno, Nobuhiro Okabe, Bau-Ching Hsieh, Benedikt Diemer, Nicole Czakon, Tom Broadhurst, Masahiro Takada, Jens Hjorth, Liliya L.R. Williams, and Graham Smith. This work is partially supported by the Ministry of Science and Technology of Taiwan under the grants MOST 103-2112-M-001-030-MY3 and MOST 103-2112-M-001-003-MY3. AZ acknowledges support by NASA through Hubble Fellowship Grant HST-HF2-51334.001-A awarded by STScI. JM is supported by the People Programme (Marie Curie Actions) of the European Union's Seventh Framework Programme (FP7/2007-2013) under REA grant agreement number 627288. DG was supported by SFB-Transregio 33 "The Dark universe" by the Deutsche Forschungsgemeinschaft (DFG), the DFG cluster of excellence "Origin and Structure of the Universe," and NASA through the Einstein Fellowship Program, grant PF5-160138.

APPENDIX A
DISCRETIZED EXPRESSIONS FOR CLUSTER LENSING PROFILES

First, we derive a discrete expression for the mean interior convergence $\kappa_\infty(<\theta)$ as a function of clustercentric radius θ using the azimuthally averaged convergence $\kappa_\infty(\theta)$. For a given set of $(N+1)$ concentric radii θ_i defining N radial bands in the range $\theta_{\rm min} \equiv \theta_1 \leqslant \theta \leqslant \theta_{N+1} \equiv \theta_{\rm max}$, a discretized estimator for $\kappa_\infty(<\theta)$ can be written as

$$\kappa_\infty(<\theta_i) = \left(\frac{\theta_{\rm min}}{\theta_i}\right)^2 \kappa_\infty(<\theta_{\rm min}) + \frac{2}{\theta_i^2}\sum_{j=1}^{i-1} \Delta \ln\theta_j\, \bar{\theta}_j^2\, \kappa_\infty(\bar{\theta}_j), \tag{43}$$

with $\Delta \ln\theta_i \equiv (\theta_{i+1} - \theta_i)/\bar{\theta}_i$ and $\bar{\theta}_i$ the area-weighted center of the ith bin defined by $[\theta_i, \theta_{i+1}]$. In the continuous limit,

$$\bar{\theta}_i = 2\int_{\theta_i}^{\theta_{i+1}} d\theta' \theta'^2 / (\theta_{i+1}^2 - \theta_i^2) = \frac{2}{3}\frac{\theta_{i+1}^3 - \theta_i^3}{\theta_{i+1}^2 - \theta_i^2}.$$

Next, we derive discretized expressions for the tangential reduced shear $g_+(\theta)$ and the inverse magnification $\mu^{-1}(\theta)$ in terms of the binned convergence $\kappa_\infty(\bar{\theta}_i)$, using the following relations:

$$g_+(\bar{\theta}_i) = \frac{\langle W\rangle_g\,[\kappa_\infty(<\bar{\theta}_i) - \kappa_\infty(\bar{\theta}_i)]}{1 - f_{W,g}\,\langle W\rangle_g\,\kappa_\infty(\bar{\theta}_i)}, \tag{44}$$

$$\mu^{-1}(\bar{\theta}_i) = [1 - \langle W\rangle_\mu\,\kappa_\infty(\bar{\theta}_i)]^2 - \langle W\rangle_\mu^2\,[\kappa_\infty(<\bar{\theta}_i) - \kappa_\infty(\bar{\theta}_i)]^2, \tag{45}$$

where both depend on the mean convergence interior to $\bar{\theta}_i$, $\kappa_\infty(<\bar{\theta}_i)$. By assuming a constant density in each radial band, we find the following expression for $\kappa_\infty(<\bar{\theta}_i)$:

$$\kappa_\infty(<\bar{\theta}_i) = \frac{1}{2}[(\theta_i/\bar{\theta}_i)^2\kappa_\infty(<\theta_i) + (\theta_{i+1}/\bar{\theta}_i)^2\kappa_\infty(<\theta_{i+1})], \tag{46}$$

where $\kappa_\infty(<\theta_i)$ and $\kappa_\infty(<\theta_{i+1})$ can be computed using Equation (43).

Accordingly, all relevant cluster lensing observables can be uniquely specified by the binned convergence profile $\{\kappa_{\infty,{\rm min}}, \kappa_{\infty,i}\}_{i=1}^N$ with $\kappa_{\infty,{\rm min}} \equiv \kappa_\infty(<\theta_{\rm min})$ and $\kappa_{\infty,i} \equiv \kappa_\infty(\bar{\theta}_i)$.

APPENDIX B
COMPARISON OF SURFACE MASS DENSITY PROFILES

Appendix B includes the surface mass density profiles for our cluster sample obtained in this study, along with those of Umetsu et al. (2014) and Merten et al. (2015).

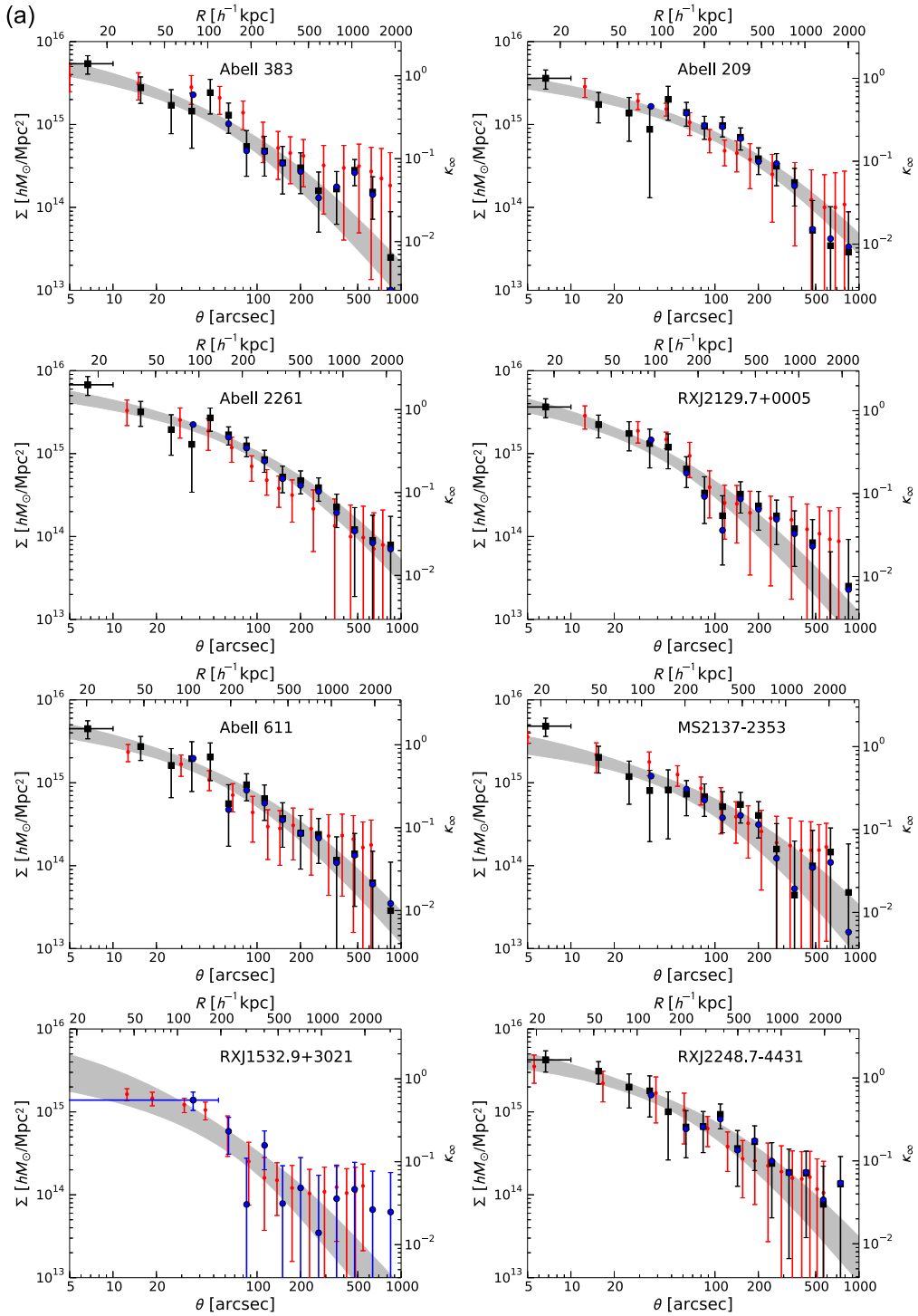

Figure 11. Surface mass density profiles derived from a joint analysis of *HST* strong/weak-shear lensing and ground-based weak shear/magnification lensing data (black squares) we have obtained for a sample of (a), (b) 16 X-ray-regular and (c) 4 high-magnification clusters selected from the CLASH survey. For each cluster, the central bin $\Sigma(<\theta_{\rm min})$ is marked with a horizontal bar. The location of each binned Σ point represents the area-weighted center of the radial band (Appendix A). The error bars represent the 1σ uncertainty from the diagonal part of the total covariance matrix including statistical, systematic, projected uncorrelated LSS, and intrinsic-variance contributions, $C = C^{\rm stat} + C^{\rm sys} + C^{\rm lss} + C^{\rm int}$ (Section 3.6.3). The gray area in each plot shows the best-fit NFW profile (68% CL) for the observed Σ profile. The results are compared to the shear+magnification results (blue circles) of Umetsu et al. (2014) and those from a SaWLens (red dots) analysis of Merten et al. (2015). The scale on the right vertical axis shows the corresponding lensing convergence κ_∞ scaled to the reference far-background source plane.

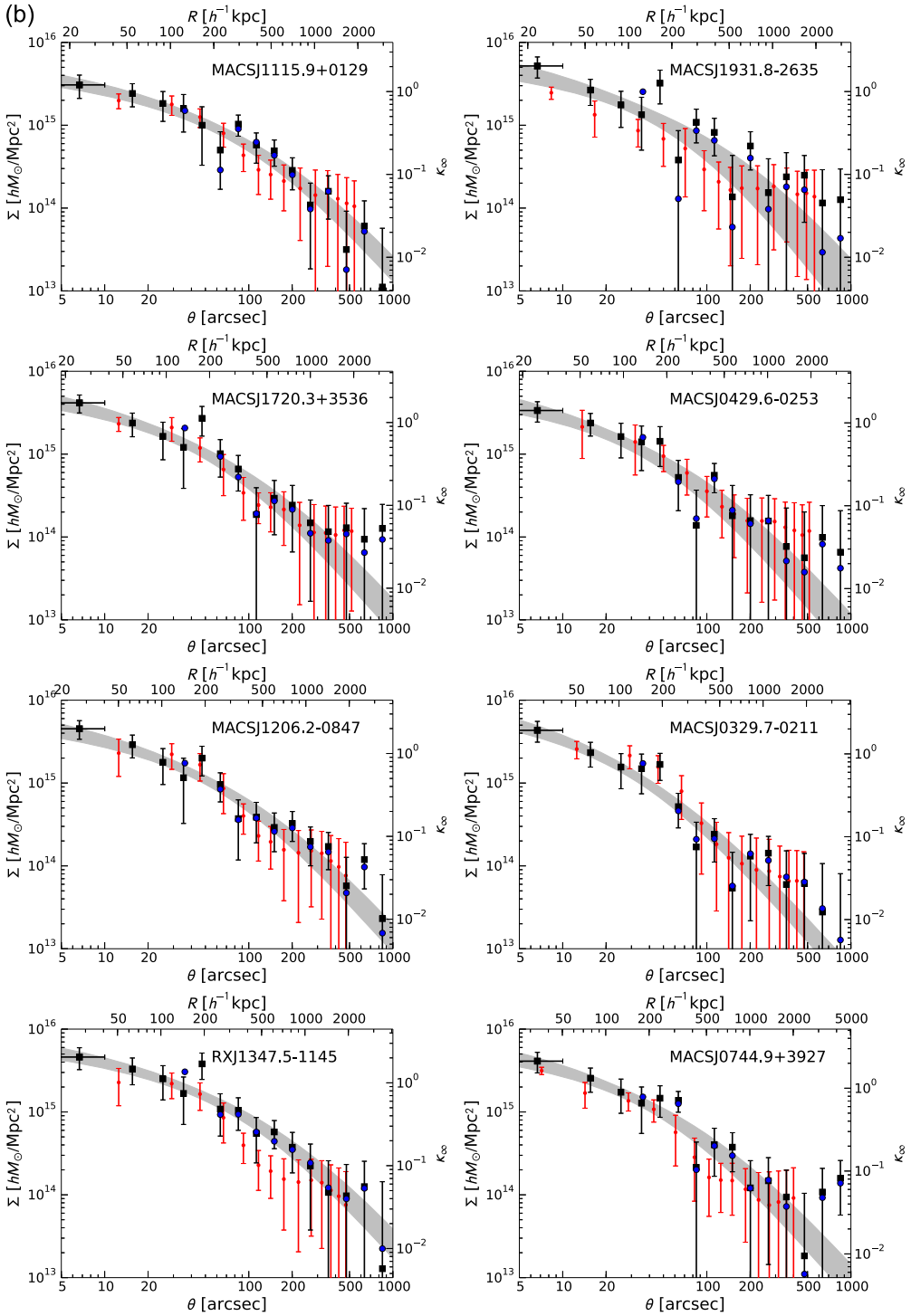

Figure 11. (Continued.)

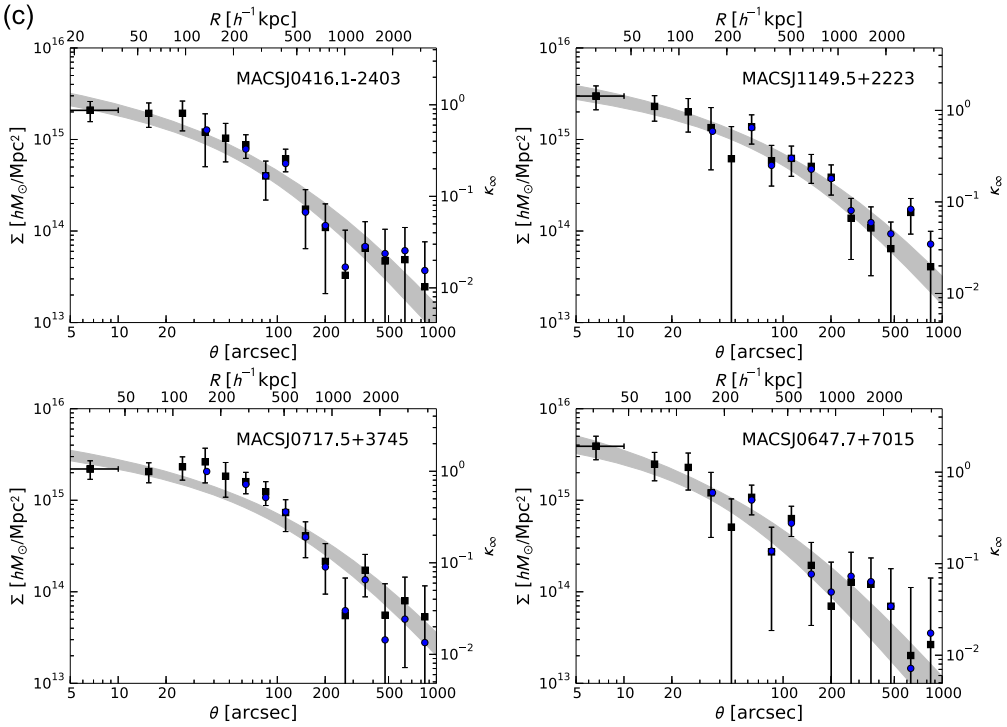

Figure 11. (Continued.)

REFERENCES

Adhikari, S., Dalal, N., & Chamberlain, R. T. 2014, JCAP, 11, 19
Agnello, A., Auger, M. W., & Evans, N. W. 2013, MNRAS, 429, L35
Andreon, S., & Bergé, J. 2012, A&A, 547, A117
Andreon, S., & Hurn, M. A. 2010, MNRAS, 404, 1922
Applegate, D. E., von der Linden, A., Kelly, P. L., et al. 2014, MNRAS, 439, 48
Baldauf, T., Smith, R. E., Seljak, U., & Mandelbaum, R. 2010, PhRvD, 81, 063531
Balestra, I., Vanzella, E., Rosati, P., et al. 2013, A&A, 559, L9
Baltz, E. A., Marshall, P., & Oguri, M. 2009, JCAP, 1, 15
Bartelmann, M., & Schneider, P. 2001, PhR, 340, 291
Becker, M. R., & Kravtsov, A. V. 2011, ApJ, 740, 25
Beers, T. C., Flynn, K., & Gebhardt, K. 1990, AJ, 100, 32
Benítez, N. 2000, ApJ, 536, 571
Benitez, N., Dupke, R., Moles, M., et al. 2014, arXiv:1403.5237
Benítez, N., Ford, H., Bouwens, R., et al. 2004, ApJS, 150, 1
Beraldo e Silva, L. J., Lima, M., & Sodré, L. 2013, MNRAS, 436, 2616
Bertin, E., & Arnouts, S. 1996, A&AS, 117, 393
Bhattacharya, S., Habib, S., Heitmann, K., & Vikhlinin, A. 2013, ApJ, 766, 32
Biviano, A., Rosati, P., Balestra, I., et al. 2013, A&A, 558, A1
Bradač, M., Clowe, D., Gonzalez, A. H., et al. 2006, ApJ, 652, 937
Broadhurst, T. 1995, arXiv:astro-ph/9511150
Broadhurst, T., Takada, M., Umetsu, K., et al. 2005, ApJL, 619, L143
Broadhurst, T. J., Taylor, A. N., & Peacock, J. A. 1995, ApJ, 438, 49
Chiu, I., Dietrich, J. P., Mohr, J., et al. 2016, MNRAS, 457, 3050
Clowe, D., Luppino, G. A., Kaiser, N., & Gioia, I. M. 2000, ApJ, 539, 540
Coe, D., Benítez, N., Broadhurst, T., & Moustakas, L. A. 2010, ApJ, 723, 1678
Coe, D., Umetsu, K., Zitrin, A., et al. 2012, ApJ, 757, 22
Coe, D., Zitrin, A., Carrasco, M., et al. 2013, ApJ, 762, 32
Connolly, A. J., Szalay, A. S., & Brunner, R. J. 1998, ApJL, 499, L125
Cooray, A., & Sheth, R. 2002, PhR, 372, 1
Coupon, J., Broadhurst, T., & Umetsu, K. 2013, ApJ, 772, 65
Covone, G., Sereno, M., Kilbinger, M., & Cardone, V. F. 2014, ApJL, 784, L25
Czakon, N. G., Sayers, J., Mantz, A., et al. 2015, ApJ, 806, 18
Dehnen, W. 1993, MNRAS, 265, 250
Diego, J. M., Broadhurst, T., Benitez, N., et al. 2015, MNRAS, 446, 683
Diemer, B., & Kravtsov, A. V. 2014, ApJ, 789, 1
Diemer, B., & Kravtsov, A. V. 2015, ApJ, 799, 108
Donahue, M., Voit, G. M., Mahdavi, A., et al. 2014, ApJ, 794, 136
Du, W., & Fan, Z. 2014, ApJ, 785, 57
Duffy, A. R., Schaye, J., Kay, S. T., & Dalla Vecchia, C. 2008, MNRAS, 390, L64
Dutton, A. A., & Macciò, A. V. 2014, MNRAS, 441, 3359
Einasto, J. 1965, TrAlm, 5, 87
Fahlman, G., Kaiser, N., Squires, G., & Woods, D. 1994, ApJ, 437, 56
Falco, E. E., Gorenstein, M. V., & Shapiro, I. I. 1985, ApJL, 289, L1
Ford, J., Hildebrandt, H., Van Waerbeke, L., et al. 2012, ApJ, 754, 143
Ford, J., Hildebrandt, H., Van Waerbeke, L., et al. 2014, MNRAS, 439, 3755
Gao, L., Navarro, J. F., Cole, S., et al. 2008, MNRAS, 387, 536
Giocoli, C., Meneghetti, M., Ettori, S., & Moscardini, L. 2012, MNRAS, 426, 1558
Girardi, M., Mercurio, A., Balestra, I., et al. 2015, A&A, 579, A4
Gorenstein, M. V., Shapiro, I. I., & Falco, E. E. 1988, ApJ, 327, 693
Graham, A. W., Merritt, D., Moore, B., Diemand, J., & Terzić, B. 2006, AJ, 132, 2701
Gruen, D., Seitz, S., Becker, M. R., Friedrich, O., & Mana, A. 2015, MNRAS, 449, 4264
Gruen, D., Seitz, S., Brimioulle, F., et al. 2014, MNRAS, 442, 1507
Haiman, Z., Mohr, J. J., & Holder, G. P. 2001, ApJ, 553, 545
Hennawi, J. F., Dalal, N., Bode, P., & Ostriker, J. P. 2007, ApJ, 654, 714
Heymans, C., Van Waerbeke, L., Bacon, D., et al. 2006, MNRAS, 368, 1323
Hildebrandt, H. 2016, MNRAS, 455, 3943
Hjorth, J., & Williams, L. L. R. 2010, ApJ, 722, 851
Hjorth, J., Williams, L. L. R., Wojtak, R., & McLaughlin, M. 2015, ApJ, 811, 2
Hoekstra, H. 2003, MNRAS, 339, 1155
Hoekstra, H. 2007, MNRAS, 379, 317
Hoekstra, H., Hartlap, J., Hilbert, S., & van Uitert, E. 2011, MNRAS, 412, 2095
Hoekstra, H., Herbonnet, R., Muzzin, A., et al. 2015, MNRAS, 449, 685
Hoekstra, H., Mahdavi, A., Babul, A., & Bildfell, C. 2012, MNRAS, 427, 1298
Hu, W., & Kravtsov, A. V. 2003, ApJ, 584, 702
Ilbert, O., Capak, P., Salvato, M., et al. 2009, ApJ, 690, 1236
Ilbert, O., Salvato, M., Le Floc'h, E., et al. 2010, ApJ, 709, 644
Israel, H., Schellenberger, G., Nevalainen, J., Massey, R., & Reiprich, T. H. 2015, MNRAS, 448, 814
Jauzac, M., Clément, B., Limousin, M., et al. 2014, MNRAS, 443, 1549
Jimeno, P., Broadhurst, T., Coupon, J., Umetsu, K., & Lazkoz, R. 2015, MNRAS, 448, 1999
Jing, Y. P., & Suto, Y. 2000, ApJL, 529, L69
Johnston, D. E., Sheldon, E. S., Wechsler, R. H., et al. 2007, arXiv:0709.1159
Kaiser, N. 1995, ApJL, 439, L1
Kaiser, N., & Squires, G. 1993, ApJ, 404, 441
Kelly, B. C. 2007, ApJ, 665, 1489

Kitayama, T., & Suto, Y. 1996, ApJ, 469, 480
Kneib, J.-P., & Natarajan, P. 2011, A&ARv, 19, 47
Komatsu, E., Smith, K. M., Dunkley, J., et al. 2011, ApJS, 192, 18
Koopmans, L. V. E., Bolton, A., Treu, T., et al. 2009, ApJL, 703, L51
Limousin, M., Richard, J., Jullo, E., et al. 2007, ApJ, 668, 643
Ludlow, A. D., Navarro, J. F., Boylan-Kolchin, M., et al. 2013, MNRAS, 432, 1103
Mandelbaum, R., Tasitsiomi, A., Seljak, U., Kravtsov, A. V., & Wechsler, R. H. 2005, MNRAS, 362, 1451
Martino, R., Mazzotta, P., Bourdin, H., et al. 2014, MNRAS, 443, 2342
Massey, R., Heymans, C., Bergé, J., et al. 2007, MNRAS, 376, 13
Medezinski, E., Broadhurst, T., Umetsu, K., et al. 2010, MNRAS, 405, 257
Medezinski, E., Broadhurst, T., Umetsu, K., Benítez, N., & Taylor, A. 2011, MNRAS, 414, 1840
Medezinski, E., Umetsu, K., Nonino, M., et al. 2013, ApJ, 777, 43
Melchior, P., Suchyta, E., Huff, E., et al. 2015, MNRAS, 449, 2219
Meneghetti, M., & Rasia, E. 2013, arXiv:1303.6158
Meneghetti, M., Rasia, E., Merten, J., et al. 2010, A&A, 514, A93
Meneghetti, M., Rasia, E., Vega, J., et al. 2014, ApJ, 797, 34
Merten, J., Cacciato, M., Meneghetti, M., Mignone, C., & Bartelmann, M. 2009, A&A, 500, 681
Merten, J., Meneghetti, M., Postman, M., et al. 2015, ApJ, 806, 4
Miyatake, H., More, S., Mandelbaum, R., et al. 2015, ApJ, 806, 1
Miyazaki, S., Oguri, M., Hamana, T., et al. 2015, ApJ, 807, 22
Monna, A., Seitz, S., Greisel, N., et al. 2014, MNRAS, 438, 1417
Mori, M., & Burkert, A. 2000, ApJ, 538, 559
Navarro, J. F., Frenk, C. S., & White, S. D. M. 1997, ApJ, 490, 493
Navarro, J. F., Ludlow, A., Springel, V., et al. 2010, MNRAS, 402, 21
Neto, A. F., Gao, L., Bett, P., et al. 2007, MNRAS, 381, 1450
Niikura, H., Takada, M., Okabe, N., Martino, R., & Takahashi, R. 2015, PASJ, 67, 103
Oguri, M. 2010, PASJ, 62, 1017
Oguri, M., Bayliss, M. B., Dahle, H., et al. 2012, MNRAS, 420, 3213
Oguri, M., & Blandford, R. D. 2009, MNRAS, 392, 930
Oguri, M., & Hamana, T. 2011, MNRAS, 414, 1851
Oguri, M., Hennawi, J. F., Gladders, M. D., et al. 2009, ApJ, 699, 1038
Oguri, M., & Takada, M. 2011, PhRvD, 83, 023008
Okabe, N., & Smith, G. P. 2015, arXiv:1507.04493
Okabe, N., Smith, G. P., Umetsu, K., Takada, M., & Futamase, T. 2013, ApJL, 769, L35
Okabe, N., Takada, M., Umetsu, K., Futamase, T., & Smith, G. P. 2010, PASJ, 62, 811
Planck Collaboration Ade, P. A. R., Aghanim, N., et al. 2014, A&A, 571, A20
Planck Collaboration Ade, P. A. R., Aghanim, N., et al. 2015, arXiv:1502.01597
Postman, M., Coe, D., Benítez, N., et al. 2012, ApJS, 199, 25
Prada, F., Klypin, A. A., Cuesta, A. J., Betancort-Rijo, J. E., & Primack, J. 2012, MNRAS, 423, 3018
Radovich, M., Formicola, I., Meneghetti, M., et al. 2015, A&A, 579, A7
Rasia, E., Meneghetti, M., Martino, R., et al. 2012, NJPh, 14, 055018
Rosati, P., Balestra, I., Grillo, C., et al. 2014, Msngr, 158, 48
Rozo, E., & Schmidt, F. 2010, arXiv:1009.5735
Sayers, J., Czakon, N. G., Mantz, A., et al. 2013, ApJ, 768, 177
Schneider, P., King, L., & Erben, T. 2000, A&A, 353, 41
Schneider, P., & Seitz, C. 1995, A&A, 294, 411
Seitz, C., & Schneider, P. 1997, A&A, 318, 687
Sembolini, F., Yepes, G., De Petris, M., et al. 2013, MNRAS, 429, 323
Sereno, M., & Ettori, S. 2015a, MNRAS, 450, 3675
Sereno, M., & Ettori, S. 2015b, MNRAS, 450, 3633
Sereno, M., Ettori, S., & Moscardini, L. 2015a, MNRAS, 450, 3649
Sereno, M., Giocoli, C., Ettori, S., & Moscardini, L. 2015b, MNRAS, 449, 2024
Sereno, M., & Umetsu, K. 2011, MNRAS, 416, 3187
Sereno, M., Veropalumbo, A., Marulli, F., et al. 2015c, MNRAS, 449, 4147
Shao, S., Gao, L., Theuns, T., & Frenk, C. S. 2013, MNRAS, 430, 2346
Smith, G. P., Mazzotta, P., Okabe, N., et al. 2016, MNRAS, 456, L74
Smith, R. E., Peacock, J. A., Jenkins, A., et al. 2003, MNRAS, 341, 1311
Takada, M., & White, M. 2004, ApJL, 601, L1
Tasitsiomi, A., Kravtsov, A. V., Gottlöber, S., & Klypin, A. A. 2004, ApJ, 607, 125
Taylor, A. N., Dye, S., Broadhurst, T. J., Benitez, N., & van Kampen, E. 1998, ApJ, 501, 539
Tinker, J. L., Robertson, B. E., Kravtsov, A. V., et al. 2010, ApJ, 724, 878
Tremaine, S., Richstone, D. O., Byun, Y.-I., et al. 1994, AJ, 107, 634
Umetsu, K. 2010, arXiv:1002.3952
Umetsu, K. 2013, ApJ, 769, 13
Umetsu, K., Birkinshaw, M., Liu, G.-C., et al. 2009, ApJ, 694, 1643
Umetsu, K., & Broadhurst, T. 2008, ApJ, 684, 177
Umetsu, K., Broadhurst, T., Zitrin, A., et al. 2011a, ApJ, 738, 41
Umetsu, K., Broadhurst, T., Zitrin, A., Medezinski, E., & Hsu, L. 2011b, ApJ, 729, 127
Umetsu, K., & Futamase, T. 2000, ApJL, 539, L5
Umetsu, K., Medezinski, E., Broadhurst, T., et al. 2010, ApJ, 714, 1470
Umetsu, K., Medezinski, E., Nonino, M., et al. 2012, ApJ, 755, 56
Umetsu, K., Medezinski, E., Nonino, M., et al. 2014, ApJ, 795, 163
Umetsu, K., Sereno, M., Medezinski, E., et al. 2015, ApJ, 806, 207
Umetsu, K., Tada, M., & Futamase, T. 1999, PThPS, 133, 53
van Waerbeke, L. 2000, MNRAS, 313, 524
Vikhlinin, A., Kravtsov, A. V., Burenin, R. A., et al. 2009, ApJ, 692, 1060
von der Linden, A., Allen, M. T., Applegate, D. E., et al. 2014a, MNRAS, 439, 2
von der Linden, A., Mantz, A., Allen, S. W., et al. 2014b, MNRAS, 443, 1973
Williams, L. L. R., & Hjorth, J. 2010, ApJ, 722, 856
Wright, C. O., & Brainerd, T. G. 2000, ApJ, 534, 34
Xu, B., Postman, M., Meneghetti, M., et al. 2016, ApJ, 817, 85
Zhao, H. 1996, MNRAS, 278, 488
Zheng, W., Postman, M., Zitrin, A., et al. 2012, Natur, 489, 406
Ziparo, F., Smith, G. P., Okabe, N., et al. 2015, arXiv:1507.04376
Zitrin, A., Fabris, A., Merten, J., et al. 2015, ApJ, 801, 44
Zitrin, A., Rephaeli, Y., Sadeh, S., et al. 2012a, MNRAS, 420, 1621
Zitrin, A., Rosati, P., Nonino, M., et al. 2012b, ApJ, 749, 97